

UILU-ENG 91-3601

Report No. 155

**FATIGUE OF ALUMINA
AT ROOM AND HIGH TEMPERATURES**

by

Chih-Kuang Jack Lin
Department of Mechanical and Industrial Engineering

A Report of the
MATERIALS ENGINEERING—MECHANICAL BEHAVIOR
College of Engineering, University of Illinois at Urbana-Champaign
October 1991

FATIGUE OF ALUMINA AT ROOM AND HIGH TEMPERATURES

Chih-Kuang Jack Lin, Ph.D.
Department of Mechanical and Industrial Engineering
University of Illinois at Urbana-Champaign, 1991

ABSTRACT

Fatigue behavior of a polycrystalline alumina at room temperature and 1200°C was investigated. Uniaxial tensile tests were conducted in both static and cyclic loading to produce stress-life curves. Cyclic loading at room temperature was found to be a deleterious effect on lifetime, as compared to static loading with a similar maximum stress. Cyclic lifetime was also found to be cycle dependent at room temperature.

A variety of loading wave forms were applied during the cyclic tests at 1200°C. High temperature results indicated that cyclic loading would not cause more detrimental effects on failure time in comparison to static loading. Cyclic lifetime at 1200°C was found to be cycle shape dependent. Specimens cyclically loaded with a short duration of maximum stress in the loading cycle took a much longer time to fail than did the static loading specimens under the same maximum applied loads. Failure time for cyclic loading with a longer hold time at maximum stress was comparable to the static loading results.

Failure analysis results suggest that the activities behind the crack tip may be the primary sources of the cyclic fatigue effects at both room and high temperatures. Detrimental cyclic effect at room temperature was likely related to the interlocking grains, frictional interlocking of asperities, and trapped grains behind the crack tip. High temperature beneficial cyclic effect (compared to static loading) might be attributed to the rate-sensitivity of the deformation of the viscous glassy phase bridging the crack surfaces behind the crack tip. A simplified model of crack bridging by the viscous glassy phase was applied to calculate the effective stress intensity factor at the crack tip under various loading conditions. Trends of the calculated results are consistent with the lifetime data obtained at high temperatures.

ACKNOWLEDGEMENTS

This research was supported by the U.S. Department of Energy under Contracts No. DE-AC02-76ER-01198 and DE-FG02-91ER-45439, and was conducted in the Materials Engineering Research Laboratory and the Materials Research Laboratory at the University of Illinois at Urbana-Champaign.

Professor Darrell F. Socie, thesis advisor, is gratefully acknowledged for his initial idea to this investigation, as well as the freedom and trust he has given me to pursue independent initiatives for my research. He is also thanked for his friendship, encouragement, and advice throughout my graduate career. Dr. Peter Kurath, and my fellow graduate students, Tom Mayer and Aslak Siljander are thanked for their friendship and assistance in the lab. Special thanks go to Tom Mayer for his invaluable help and contributions to the experimental set-up of this work.

Dr. Youren Xu and Professor Avigdor Zangvil are thanked for their assistance on TEM analysis and helpful discussions related to this work. Mr. Darrell Miller, of machine shop in Materials Research Laboratory, is especially acknowledged for his friendship and excellent work in performing the fabrication of the specimens.

I would like to express my deep gratitude to my parents and family for their continuous encouragement and support throughout my personal and professional development. Finally and most importantly, my wife, Tsui-Rong (Ellen), is sincerely thanked for her patience, understanding, and unselfish support in taking care of our baby daughter, Kathy, while this work was being completed.

TABLE OF CONTENTS

	Page
LIST OF TABLES	viii
LIST OF FIGURES	ix
 1. INTRODUCTION.....	 1
1.1 Review of Previous Work on Ceramic Fatigue	2
1.2 Purpose and Scope	7
 2. MATERIAL TESTING.....	 9
2.1 Material and Specimen Fabrication	9
2.2 Test Facility.....	10
2.3 Test Procedure and Loading Paths.....	12
 3. EXPERIMENTAL RESULTS.....	 13
3.1 Room Temperature Results.....	13
3.2 High Temperature Results	14
 4. LIFETIME ANALYSIS	 17
4.1 Model for Prediction of Cyclic Lifetime.....	17
4.2 Comparison of Measured and Predicted Cyclic Lifetime.....	20
 5. DISCUSSION	 23
5.1 Cyclic Effects at Room Temperature	23
5.2 Cyclic Effects at High Temperatures	24
5.3 Comparison of Cyclic Effects at Room and High Temperatures.....	29
 6. FAILURE ANALYSIS	 31
6.1 Scanning Electron Microscopy Observations.....	31
6.1.1 Room Temperature Fracture Patterns.....	32
6.1.2 High Temperature Fracture Patterns.....	34
6.2 Transmission Electron Microscopy Observations.....	38
6.2.1 Room Temperature Phenomena.....	38
6.2.2 High Temperature Phenomena	39

6.3	Failure Mechanisms	40
6.3.1	Fatigue Mechanisms at Room Temperature.....	42
6.3.2	Fatigue Mechanisms at High Temperatures.....	46
6.3.2.1	Slow Crack Growth vs. Creep Rupture	46
6.3.2.2	Comparison with Other Studies.....	48
6.3.2.3	Bridging Effect of the Viscous Glassy Phases.....	52
7.	CONCLUSIONS.....	58
	TABLES.....	60
	FIGURES.....	69
	REFERENCES.....	127
	APPENDIX.....	135

LIST OF TABLES

	Page
Table 1 Results of cyclic fatigue at room temperature under triangular loading wave form with $R = 0.075$	60
Table 2 Results of static fatigue at room temperature under constant loading	61
Table 3 Results of cyclic fatigue at 1200°C under sine wave form with $R = 0.1$ and $f = 2$ Hz	62
Table 4 Results of cyclic fatigue at 1200°C under square wave form with $R = 0.1$ and $f = 2$ Hz	63
Table 5 Results of cyclic fatigue at 1200°C under trapezoid I wave form with $R = 0.1$, $t_h = 0.25$ s, and $t_u = 0.02$ s	64
Table 6 Results of cyclic fatigue at 1200°C under trapezoid II wave form with $R = 0.1$, $t_h = 2.5$ s, and $t_u = 0.02$ s	65
Table 7 Results of cyclic fatigue at 1200°C under square wave form with $R = 0.5$ and $f = 2$ Hz	66
Table 8 Results of static fatigue at 1200°C under constant loading	67
Table 9 Calculated r factors for various kinds of loading wave forms	68

LIST OF FIGURES

	Page
Figure 1 Geometry of tested specimens. (All dimensions in millimeters).....	69
Figure 2 Complete view of test system.	70
Figure 3 Schematic drawing of loading paths for fatigue tests at room temperature. (A) static loading, (B) triangular wave form (0.1 to 5 Hz, $R = 0.075$).	71
Figure 4 Schematic drawing of loading paths for fatigue tests at 1200°C. (A) static loading, (B) sine wave form (2 Hz, $R = 0.1$), (C) square wave form (2 Hz, $R = 0.1$ and 0.5), and (D) trapezoid wave form (trapezoid I: $t_h = 0.25$ s, trapezoid II: $t_h = 2.50$ s, $t_u = 0.02$ s and $R = 0.1$ for both cases).	72
Figure 5 Cyclic fatigue lifetime under different cycle frequencies at room temperature. (Some of the data points of 0.5 and 2 Hz are from Refs. 38 and 59; see Table 1 for details.)	73
Figure 6 Comparison of static and cyclic fatigue lifetime at room temperature. (Arrow indicates that failure of specimen did not occur when the test was terminated.) (Some of the data points of 0.5 and 2 Hz are from Refs. 38 and 59; see Table 1 for details.)	74
Figure 7 Comparison of cyclic fatigue lifetime at 1200°C under various kinds of loading wave forms with $R = 0.1$	75
Figure 8 Comparison of cyclic fatigue lifetime at 1200°C under square wave form with $R = 0.1$ and 0.5.	76
Figure 9 Comparison of static and all cyclic fatigue lifetime with $R = 0.1$ at 1200°C. (The dashed lines are the upper and lower bound of static fatigue data.)	77
Figure 10 Comparison of static and cyclic fatigue lifetime under square wave form with $R = 0.1$ and 0.5 at 1200°C. (The dashed lines are the upper and lower bound of static fatigue data.)	78
Figure 11 Comparison of measured cyclic lifetime at room temperature with predicted value from static fatigue data. (Some of the data points of 0.5 and 2 Hz are from Refs. 38 and 59; see Table 1 for details.)	79
Figure 12 Comparison of measured cyclic lifetime for sine wave form at 1200°C with predicted value from static fatigue data.	80
Figure 13 Comparison of measured cyclic lifetime for square wave form ($R = 0.1$) at 1200°C with predicted value from static fatigue data.	81

Figure 14	Comparison of measured cyclic lifetime for trapezoid I wave form at 1200°C with predicted value from static fatigue data.....	82
Figure 15	Comparison of measured cyclic lifetime for trapezoid II wave form at 1200°C with predicted value from static fatigue data.....	83
Figure 16	Comparison of measured cyclic lifetime for square wave form ($R = 0.5$) at 1200°C with predicted value from static fatigue data.	84
Figure 17	SEM micrographs of the as-received microstructure for the AD-998 alumina showing the residual porosity. (A) low magnification view and (B) high magnification view.....	85
Figure 18	Diffuse dark-field TEM micrographs of the as-received alumina illustrating the isolated zones of glassy phase (A) at triple-point junctions, (B) at a two-grain "channel", and (C) along a two-grain interface and connected triple-point junctions. The glassy phase appears bright in the diffuse dark-field image.....	86
Figure 19	SEM micrographs demonstrating the typical fracture surface in cyclic fatigue specimens failed at room temperature. (A) macroscopic view, (B) high magnification view in the slow crack growth region, (C) high magnification view in the fast fracture zone. ($\sigma_{\max} = 220.6$ MPa, 2 Hz).....	88
Figure 20	SEM micrographs of some typical features of transgranular failure mode observed in the fracture surface of room temperature specimens. (A) general view, (B and C) higher magnification view of the cleavage facets associated with the grain-boundary pores or within-grain pores, and (D) a transverse crack through the grain facet.	90
Figure 21	SEM micrographs demonstrating the typical fracture surface in static fatigue specimens failed at room temperature. (A) macroscopic view, (B) high magnification view in the slow crack growth region, and (C) high magnification view in the fast fracture zone. ($\sigma_{\max} = 234.4$ MPa)....	92
Figure 22	Debris formation observed around the macrocrack branching areas on the fracture surface in both (A) static fatigue and (B) cyclic fatigue specimens failed at room temperature.	94
Figure 23	SEM micrographs of the axially sectioned view in fractured specimens under different loading conditions at room temperature. (A) static loading ($\sigma_{\max} = 234.4$ MPa) and (B) cyclic loading ($\sigma_{\max} = 220.6$ MPa, 2 Hz). (Arrows indicate the loading direction.).....	95
Figure 24	Some typical features observed along the crack paths in room temperature cyclic fatigue specimens. (A) crack deflection, (B) interlocking grains, (C) contact of fracture surface asperities, (D) an unbroken ligament, and (E) trapped grains within the closed crack.	96

Figure 25	SEM micrographs demonstrating the typical fracture surface in sine wave form specimens failed at 1200°C. (A) macroscopic view, (B) high magnification view in the slow crack growth region, and (C) high magnification view in the fast fracture zone. ($\sigma_{\max} = 86.2$ MPa).....	99
Figure 26	Macroscopic SEM view of the typical fracture surface in square wave form specimens ($R = 0.1$) failed at 1200°C. ($\sigma_{\max} = 86.2$ MPa)	101
Figure 27	Macroscopic SEM view of the typical fracture surface in square wave form specimens ($R = 0.5$) failed at 1200°C. ($\sigma_{\max} = 48.3$ MPa)	102
Figure 28	Macroscopic SEM view of the typical fracture surface in trapezoid I wave form specimens failed at 1200°C. ($\sigma_{\max} = 86.2$ MPa)	103
Figure 29	Macroscopic SEM view of the typical fracture surface in trapezoid II wave form specimens failed at 1200°C. ($\sigma_{\max} = 34.5$ MPa)	104
Figure 30	SEM micrographs demonstrating the typical fracture surface in static loading specimens failed at 1200°C. (A) macroscopic view, (B) high magnification view in the slow crack growth region, and (C) high magnification view in the fast fracture zone. ($\sigma_{\max} = 34.5$ MPa).....	105
Figure 31	Typical failure origins at all applied loading conditions at 1200°C. (A) a large void near the edge of the fracture surface (square, $R = 0.1$, $\sigma_{\max} = 58.6$ MPa), (B) a large surface flaw (sine, $\sigma_{\max} = 86.2$ MPa), and (C) a large-grained agglomerate (static loading, $\sigma_{\max} = 34.5$ MPa).....	107
Figure 32	Typical profiles of the glassy phase on fracture surface in different loading conditions at 1200°C. (A) sine wave form ($\sigma_{\max} = 86.2$ MPa), (B) trapezoid II wave form ($\sigma_{\max} = 34.5$ MPa), and (C) static loading, ($\sigma_{\max} = 34.5$ MPa).....	109
Figure 33	Comparison of the SEM micrographs of the grain facets in the areas without glassy phase on the fracture surface in the (A) room and (B) high temperature specimens.	111
Figure 34	Evidence of grain-boundary sliding from the SEM micrograph of a trapezoid II wave form specimen failed with $\sigma_{\max} = 34.5$ MPa at 1200°C.....	112

Figure 35	SEM micrographs of the axially sectioned view in fractured specimens under different loading conditions at 1200°C. (A) sine wave form ($\sigma_{\max} = 62$ MPa), (B) static loading ($\sigma_{\max} = 34.5$ MPa), (C) high magnification view of the non-failure-induced macrocracks in (B), and (D) the area around the crack tip of a non-failure-induced macrocrack in (C). (Arrows indicate the loading direction.)	113
Figure 36	High magnification SEM view of the crack profile in an axially-cut section of a static loading specimen ($\sigma_{\max} = 34.5$ MPa) failed at 1200°C. (A) typical crack path, (B and C) enlarged views showing the viscous glassy phases bridging the crack surfaces at marked segments, G1 and G2, respectively, in (A).	115
Figure 37	TEM micrographs of the general structure after failure in room temperature (A) static and (B) cyclic fatigue specimens.....	117
Figure 38	TEM micrographs demonstrating (A) growth and linkage of pores in a static loading specimen ($\sigma_{\max} = 34.5$ MPa) and (B) isolated pores (no linkage of pores was observed) in a sine wave form specimen ($\sigma_{\max} = 62$ MPa).	118
Figure 39	Evidence of grain-boundary sliding in the TEM micrograph of a static loading specimen failed with $\sigma_{\max} = 34.5$ MPa at 1200°C.....	119
Figure 40	TEM micrograph showing a side view of the finger-like meniscus of the viscous glassy phase between two alumina grains.....	120
Figure 41	A damage zone of distributed microcracking ahead of a long fatigue crack in an Al_2O_3 -33 vol.% SiC whisker composite subjected to cyclic tensile loads (in four-point flexure) in 1500°C air environment. (From Ref. 62)..	121
Figure 42	Microcrack coalescence through shear band formation on the tensile surface of a bend bar of AVCO alumina deformed at 100 MPa and 1150°C. Bars = 0.1 mm. (From Ref. 82).....	122
Figure 43	Extensive microcracking is visible on the side of a tensile specimen of ARCO alumina deformed at 100 MPa and 1250°C. Bar = 1 mm. (From Ref. 82).....	123
Figure 44	Microcracking and crack-tip blunting on an internal section of a tensile specimen of ARCO alumina deformed at 55 MPa and 1250°C. Bars = 10 μm . (From Ref. 82).....	124
Figure 45	Comparison of the calculated effective stress intensity factors at the crack tip in static loading and various cyclic loading wave forms at 1200°C under the same maximum applied stress intensity factor, K_{\max}	125

Figure 46	Comparison of the calculated effective stress intensity factors at the crack tip in static loading and square loading wave forms ($R = 0.1$ and 0.5) at 1200°C under the same maximum applied stress intensity factor, K_{max}	126
Figure A1	Geometry of the crack and ligament assumed for the bridging-zone model. (From Ref. 103).....	139

1. INTRODUCTION

The use of ceramic materials for structural engineering applications is increasingly being developed, e.g. in advanced heat engines. They offer higher specific strength, specific stiffness, hardness, temperature resistance, wear resistance, and corrosion resistance. The combination of these desirable properties make ceramic materials significant potential for use in the more efficient engines requiring higher operating temperatures. Many of the engineering ceramic components are subjected to cyclic loading at elevated temperatures for prolonged periods, yet very few researchers have investigated fatigue behavior of ceramics at high temperatures. In ceramic literature static fatigue has been used to describe the phenomenon of delayed fracture of a ceramic member under a sustained constant load. If the delayed fracture occurs under cyclic loading, it is termed cyclic fatigue.

Most effort to date has been directed towards increasing the room temperature fracture toughness of ceramics. To be commercially viable, these materials must also have adequate reliability and long term strength durability under sustained thermal and mechanical loading. The long term behavior of ceramic materials strengthened by various toughening mechanisms has not been well quantified and is not quite understood. Cyclic fatigue, in particular at high temperatures, would be the most challenging field regarding the long term performance of engineering ceramic materials. Although the physical and mechanical properties of ceramic materials have been studied extensively, it is not until recently that cyclic fatigue has received more attention in ceramics. The reason is that ceramics seem to be generally perceived as unsusceptible to significant degradation under cyclic loading due to their low ductility and lack of crack-tip plasticity.

1.1 Review of Previous Work on Ceramic Fatigue

Although the studies of fatigue in ceramics have begun since about 1956,[1-3] they are still inadequate and inconclusive. The limited prior work on the fatigue properties of ceramics has shown conflicting conclusions regarding the causes of the observed damage. Some of the previous studies on alumina,[4-8] silicon nitride,[9-11] zirconia,[12] and silicon carbide[8,10,13] demonstrated no definitive evidence of true cyclic fatigue. The observed phenomenon of cyclic fatigue was essentially a cyclic manifestation of static fatigue. In contrast, much of the prior work has concluded that the evidence of cyclic fatigue effect indeed exists in ceramics such as alumina,[1,8,14-22] silicon nitride,[8,23-26] zirconia,[8,27-31] and others.[8,32] In addition to the studies cited above, still other research on fatigue properties of ceramics has observed cyclic effects only under certain conditions.[4,6,33-36] Although some other cyclic fatigue data have been published in the form of stress-life curves or crack growth rate for ceramics including alumina,[3,37-42] silicon nitride,[41-50] zirconia,[51,52] and others,[53-57] no attempts were made in these studies to determine whether ceramics undergo any true cyclic fatigue.

Some early work done by Evans et al.[5,9] was focused on the crack propagation under cyclic loading in silicon nitride, porcelain, and glass. Double torsion specimens were used to observe the crack growth rate under static and cyclic loading, respectively. They found that the measured cyclic crack growth rates could be rationalized on the crack growth data under static loading and the time variation of load during cycling; i.e., the cyclic fatigue was essentially the integrated effects of static fatigue. It was therefore concluded that these ceramics did not exhibit true cyclic fatigue damage. Similar conclusions were also drawn on alumina from the studies of Lathabai et al.[7] and Kawakubo et al.[8] that no significant reduced lifetime under cyclic, as opposed to static, loading was observed and cyclic lifetime was predictable from the measured static lifetime by establishing the traditional S-N curves. In addition, Horibe and Sumita[13] used pre-

indented specimens to study the fatigue crack propagation behavior of SiC under static and cyclic loading. No crack extension was observed in the same specimen when the loading mode was shifted to cyclic loading with the maximum stress equal to the stress level of static loading. It was therefore suggested that cyclic fatigue might not exist in this silicon carbide.

However, much more investigation points out ceramics do undergo cyclic fatigue at room temperature. For instance, results obtained by Guiraud[17] on polycrystalline alumina under uniaxial static and cyclic tension-compression loading showed that cyclic lifetime was much shorter than static lifetime under the same maximum stress. Moreover, Ewart and Suresh[18,19] indicated that the application of cyclic compressive loads to edge-notched specimens of alumina could lead to stable cyclic fatigue crack growth due to the local residual tensile stresses around the notch. However, the limited crack growth arrests after a finite extension of the crack. Direct evidence of cyclic fatigue crack growth in silicon nitride under tension-tension cyclic loading was reported by Grathwohl[23] and Horibe[24] using pre-indented bending specimens. They claimed that no crack extension was observed under static loading, while cyclic loading enhanced crack propagation in those silicon nitride ceramics.

More evidence of cyclic fatigue crack propagation at room temperature has been unequivocally demonstrated in transformation-toughened magnesia-partially stabilized zirconia (Mg-PSZ) by Dauskardt et al.[29,30] using compact tension specimens containing long cracks (millimeter scale). Several aspects of their observations were directed towards the conclusion that a true cyclic fatigue effect does exist in Mg-PSZ. It was shown that cyclic loading led to notable crack growth at stress intensity factors significantly below those required to produce crack growth in sustained constant loading. The crack growth rates under tension-tension cyclic loading were found to be several orders of magnitude larger than the crack growth rates at peak sustained loading. More importantly, variable-amplitude cyclic loading also demonstrated transient crack-growth acceleration following

low-high block overloads, transient crack-growth retardation following high-low block overloads, and delayed retardation following single tensile overloads in Mg-PSZ. These results suggest that Mg-PSZ exhibits a cyclic fatigue crack growth behavior analogous to the common fatigue phenomenon of metals.

Some studies have observed that ceramic materials suffer cyclic fatigue damage only under certain circumstances. Cyclic fatigue effects have been detected in an alumina only at high frequency by Krohn and Hasselman.[4] Their results were examined by Evans[6] and found to be no apparent cyclic fatigue effects within the scatter of the data except at the highest frequency (40 Hz). The results obtained by Chen and Knapp[33] on another alumina indicated that cyclic fatigue effects did exist at room temperature but disappeared at temperatures above 216°C. In a study on silicon nitride, Kawakubo and Komeya[34] reported that cyclic loading, as compared to peak sustained loading, significantly reduced lifetime only at low applied load regions. Similar observation was also obtained by Ueno et al.[35] in another silicon nitride, where fatigue crack propagated cycle-dependently in the range of $K_{I_{max}} < K_{ISCC}$ and time-dependently in the range of $K_{I_{max}} > K_{ISCC}$. Moreover, Ohya et al.[36] have recently shown that a yttria-partially stabilized zirconia (Y-PSZ) exhibited true cyclic fatigue only at low stress ratio $R=0.05$ as compared to $R=0.3$ to 1.

In addition to the work cited above, there are still more studies of cyclic fatigue in ceramics without critical examination of the existence of true cyclic effect. For example, Ko[39-41] obtained the traditional stress-life (S-N) curves for alumina and silicon nitride using rotary bending tests. The fatigue lifetime in both materials increased with the decrease in applied stress level. Similar observations in other silicon nitrides were obtained by Kossowsky,[43] Liu and Brinkman[45,46] at high temperatures. Moreover, results of direct measurement of the crack growth under cyclic loading have been expressed as crack velocity-stress intensity (V-K) curves for silicon nitride,[42] and ceramic composite.[57]

Hoshide et al.[42] and Luh et al.[57] showed that, at room temperature, the cyclic crack propagation in ceramics could be defined by the form of Paris power law, $da/dN = C\Delta K^m$.

Some previous fatigue tests in ceramics were focused on the empirical understanding of the effects of various factors on the S-N or V-K curves. The variables examined include grain size,[17,40] frequency,[25,29,35,36,47,49,58] stress ratio,[25,29,35,36,47,48,58] loading mode,[47,50] surface finish,[51] volume,[58] and stress concentration.[59]

In the studies of polycrystalline alumina, Guio[17] and Ko[40] both demonstrated the decreases in resistance to cyclic fatigue as the average grain size increased. The effects of frequency on cyclic fatigue behavior of silicon nitride at room temperature were investigated by Masuda et al.[47,49,58] using cantilever beam specimens. Their results showed cyclic fatigue lifetime was cycle dependent and frequency independent at room temperature. Similar observations were also obtained in other silicon nitride by Kishimoto et al.[25,35] and Mg-PSZ by Dauskardt et al.[29] measuring the room temperature crack propagation rates. It was found in those studies[25,35,29] that crack growth rate per cycle, da/dN , was frequency independent and almost constant under the same ΔK or K_{max} ; i.e. the crack velocity with respect to time, da/dt , increased linearly with frequency.

Additionally, Kishimoto et al.[25,35] and Dauskardt et al.[29] also reported that the crack growth rates increased with the decreases in stress ratio under the same maximum stress intensity factor in their chosen ceramic materials. Soma et al.,[47] Nikkila and Mantyla[50] examined the effects of loading mode on the cyclic fatigue behavior of silicon nitride at room temperature, and found that tension-compression loading produced more damage than tension-tension loading with the same peak stress. This suggests that crack propagation can also occur in ceramics under compressive stresses in smooth specimens.

The unusual results obtained by Zelizko and Swain[51] indicated that no significant differences in the S-N curves of Mg-PSZ with three different surface finishes including axially ground, radially ground and polished. However, for most ceramics, the strength of

polished specimen is higher than that of as-machined material, and the specimens ground parallel to stress direction are stronger than the perpendicular-ground specimens. The volume effect on the cyclic fatigue properties of silicon nitride has been studied by Masuda et al.[58] using cantilever beam and uniaxial tensile specimens under alternative loading. With the same stress amplitude, the cantilever beam specimen with small effective volume took a much longer time to fail as compared to the uniaxial tensile specimen having a large volume experiencing the maximum stress.

The effect of stress concentration on the fatigue strength in ceramics has recently been examined by Mayer[59] using double-notch specimens of alumina. The smooth specimens last longer than the notched specimens under the same nominal stresses. However, the notched specimens became increasingly less sensitive to the stress concentration factor, K_t , as the applied stress level decreased. This implied the existence of a fatigue notch factor, K_f . The value of K_f was found to be 1.2 which is significantly less than the K_t value of 2.13.

Most of the above studies involving cyclic or static loading were conducted at room temperature. Only a limited number of researchers have studied cyclic fatigue behavior in ceramics at high temperatures. Those ceramic materials investigated at high temperatures under cyclic loading include alumina,[33,37,59-61,63] silicon nitride,[9-11,43-47,58,64-66] silicon carbide,[10,13,63] and ceramic composites.[54,60-62] Only a few of these recent work at high temperatures has critically compared the lifetime or crack growth rate under cyclic loading to the corresponding lifetime or crack growth rate under static loading. Among those comparisons,[9,10,13,60-62,64-66] two distinct observations were obtained: (1) cyclic loads at high temperatures were found to extend the lifetime or decelerate crack propagation compared to static loads with a maximum stress or stress intensity factor equal to the maximum cyclic stress or stress intensity factor;[60-62,64-66] (2) no true cyclic effects on the failure time or crack growth rate at high temperatures were detected.[9,10,13] These high temperature results are contrary to the room temperature

results in which the cyclic effects, where they exist, would degrade more strength than static loading. More discussion on those studies of high temperature fatigue in ceramics will be given in a later chapter.

1.2 Purpose and Scope

In the previous studies on high temperature fatigue of ceramics, a sinusoidal or triangular wave form was exclusively used as the cyclic loading pattern. In high temperature metal fatigue, fatigue failure can occur by fatigue and/or interactions between creep and fatigue depending on the loading wave form. However, there is still lack of understanding of the fatigue behavior of ceramic materials in the creep regime under cyclic loading with hold time introduced at peak stress in each cycle. It is an important consideration in design and operation of structural ceramic components to determine whether the high temperature cyclic fatigue of ceramics is controlled by the number of load cycles or by any time dependent process.

Polycrystalline alumina is considered a typical representative of modern structural ceramics. These ceramics are developed and designed to serve as structural components subjected to high thermal and high mechanical loading conditions. Thus, study of high temperature failure mechanisms and lifetime prediction in ceramics is of considerable practical interest and need. In the past several years, studies on high temperature failure mechanisms of ceramics have focussed mainly on creep damage under constant loading (e.g. Refs. 67-82). More information is necessary to understand the cyclic fatigue behavior of alumina at elevated temperatures where most structural ceramic components will be used in service. The main goal of this study is to characterize cyclic fatigue behavior of ceramics, in particular at high temperatures, by systematic experiments on a polycrystalline alumina. Tests are conducted in both static and cyclic tension loading at both room and elevated temperatures. One of the major concerns in this investigation is

whether alumina undergoes any true cyclic fatigue at both room and high temperatures. A direct comparison of static and cyclic fatigue results will provide some insight into the failure mechanisms in ceramics at both room and elevated temperatures. A variety of loading wave forms are applied for cyclic loading at 1200°C. Effects of cycle shape, maximum stress, and duration of maximum stress on the lifetime of alumina at high temperatures are examined. Failure analysis is conducted with electron microscopes to examine the fatigue mechanisms at both room and high temperatures. The results of this study will lead to a better understanding of the fatigue behavior in ceramics on both the macroscopic and microscopic scale.

2. MATERIAL TESTING

In this study a 99.8%-pure polycrystalline alumina ceramic* was investigated. Although few data have been published for this material in the form of stress-life curve only under cyclic loading at room temperature,[38,59] no attempts were made to examine the existence of any true cyclic fatigue effect in this alumina. Therefore, both static and cyclic fatigue tests were conducted in this program at room temperature and 1200°C to characterize the fatigue behavior of this alumina ceramic at room and high temperatures.

2.1 Material and Specimen Fabrication

The specimens tested in this investigation were made from commercial polycrystalline alumina rods.* The average grain size of this material is about 6 μm and some grains are as large as 25 μm . Energy dispersive X-ray spectrometer (EDS) analysis indicated that Si (and presumably oxygen) is the primary element of the grain-boundary phase in this nominally 99.8%-pure alumina, with trace amounts of Mg, Ca, Na, and Fe. The residual porosity of this ceramic material is about 1.5%. The manufacturer provides the room temperature properties of this materials as follows: specific gravity = 3.90, elastic modulus = 345 GPa, flexural strength = 331 MPa, and compressive strength = 2071 MPa. The fracture toughness of this alumina at room temperature was found to be 3.35 $\text{MPa}\cdot\text{m}^{1/2}$ by Tschegg and Suresh[83] using circumferentially notched cylindrical rods quasi-statically fractured after being precracked in uniaxial cyclic compression.

Uniaxial tensile specimens with uniform gage section were used in both static and cyclic fatigue tests. The geometry of the testing specimens is shown in Figure 1. Specimens were circumferentially ground to the final dimensions from the supplied rods

* Grade AD-998, Coors Ceramics Co., Golden, CO.

using an 150-grit diamond grinding wheel. The surface finish of the specimens was quantitatively determined by measuring the surface roughness using surface profilometer and was found to be $R_q = 1\sim2\ \mu\text{m}$ (root mean square average roughness).

2.2 Test Facility

Most of the mechanical behavior studies of ceramics have been conducted using bending test because of its simplicity and relatively inexpensive nature, where only a small portion of the small rectangular specimen is subjected to the maximum stress. There is small possibility to encounter a critical flaw in this highly stressed region. Ceramics are very sensitive to surface or volume flaws implanted during processing and machining. Thus, this type of test may be suitable for screening work but is not applicable to extrapolate its results to the aspects for design of structural ceramic components. Uniaxial tensile testing was utilized in this study. Advantages for uniaxial tensile testing of ceramics include: (1) there is smaller scatter of test results due to a larger volume of material subjected to the maximum stress in an uniaxial tensile test specimen compared with small bending test specimens, and a higher probability of flaws existing in this larger volume; (2) uniaxial homogeneous stress distribution is necessary for fatigue tests at high temperatures to avoid the stress redistribution effects.

A new system for testing brittle materials under cyclic tensile loading at elevated temperatures was developed and set up jointly by the author and Mayer. Details of the experimental set-up are given in a previous study by Mayer.[59] A brief description of this high temperature testing system is given in the following paragraphs.

A self-aligning grip system designed for uniaxial tensile testing was used to accomplish proper alignment and reduce bending strains. The grip system was originally designed at Oak Ridge National Laboratory (ORNL)[84] and using a buttonhead specimen. However, some of the specimens[38,59] have been found to fail around the shoulder of the

buttonhead instead of the gage section. The grip-head was then replaced by a hydraulic collet gripping head which can hold smooth-shank specimens (see Figure 1) to eliminate the buttonhead and the associated failures outside of the gage section of the specimen. This new grip-head also includes a water-cooling jacket for high temperature tests. The mechanical self-aligning mechanism design by ORNL is still utilized by the new modified grip system. This modified grip system was then attached to a closed-loop servo-hydraulic test machine for both static and cyclic loading tests. Excellent alignment of the load train has been verified through several bending strain tests with a maximum bending strain equal to 0.46% of the applied axial strain.

Induction heating was used to achieve the high testing temperatures. The advantage of using induction heating is that heat can be focused onto the gage section of the uniaxial tensile specimen so that the specimen's ends are heated only through conduction. Thus, the pull rod extension, used in other high temperature testing systems, is not necessary as the ends of the specimen are at sufficiently low temperature to allow using the water-cooled hydraulic collet gripping head due to the low thermal conductivity of alumina. A pair of silicon carbide susceptors are directly heated with induction power as alumina is an electrical and magnetic insulator. The alumina specimen can then be easily heated to 1200°C through radiation from the red hot silicon carbide susceptors.

Figure 2 shows the complete view of the entire test system as it looks during a test. The self-aligning grip-heads are located outside of the small induction furnace and the two heat shields in the test frame. The induction power generator connected with the induction coils surrounding the small furnace just stands next to the test frame. The 20-kip load cell is controlled by an MTS Model 442 Controller and an MTS Model 436 Control Unit, both of which reside in the rack beside the other side of test frame. The temperature controller and two digital temperature readouts are also contained in the rack and connected to three type-R thermocouple probes, which are inserted through the small furnace for temperature measurement.

2.3 Test Procedure and Loading Paths

Static fatigue and cyclic fatigue tests were carried out at both room temperature and 1200°C in air. For high temperature tests, all specimens were preheated to 1200°C with a heating rate of 12°C/min to avoid thermal shock and remained at 1200°C for 30 minutes to reach thermal equilibrium before the start of each test. The specimens for static fatigue test at room temperature and 1200°C were tested to failure under constant tensile loads.

The room temperature cyclic fatigue tests were conducted at a stress ratio $R = 0.075$ ($R = \sigma_{\min}/\sigma_{\max}$) with a triangular loading wave form. The value of the testing frequency for room temperature cyclic loading tests is at a range of 0.1 to 5 Hz. The loading path for the static and cyclic fatigue test at room temperature is schematically shown in Figure 3.

Cyclic fatigue tests at 1200°C were mainly performed with a stress ratio $R = 0.1$ under different cyclic loading wave forms as shown in Figure 4. The testing frequency for cyclic loading with a sine or square wave form was 2 Hz. Two types of trapezoid wave forms were applied. The hold time at maximum load for the first one, trapezoid I, is $t_h = 0.25$ s which is equal to the duration of maximum load in the square wave form. The hold time of the second trapezoid wave form, trapezoid II, is increased 10 times to 2.5 s. The unloading time, t_u , in both trapezoid wave forms is 0.02 s. Another set of specimens were conducted with a square wave form at a frequency of 2 Hz and $R = 0.5$ to examine the stress ratio effects on the cyclic fatigue behavior of alumina at elevated temperatures.

Post-failure microstructural analysis is performed with both scanning electron microscopy (SEM) and transmission electron microscopy (TEM) to study the failure mechanisms at both room and high temperatures.

3. EXPERIMENTAL RESULTS

In this chapter an overview of the mechanical testing results will be given. These data will be provided in the form of tables and stress-life curves for each loading path applied in this study. Detailed analysis and discussion of these results are left to later chapters.

3.1 Room Temperature Results

The results of cyclic fatigue tests under triangular loading wave form with $R = 0.075$ and a frequency range of 0.1 to 5 Hz at room temperature are given in Table 1 and graphically shown in Figure 5. Each point represents a single specimen tested to failure. Tensile strength was plotted as a single cycle to failure. The data produced in two previous studies[38,59] using a similar material and test system is also given in Table 1 and Figure 5. The current results agree very well with the data reported by the developer of the ORNL self-aligning grip system[38] as shown in Figure 5. Thus, the new modified hydraulic grip-heads worked well with the test frame and produced valid data. Cyclic fatigue behavior of this alumina at room temperature appears to depend principally on the number of cycles rather than on time as the cyclic fatigue strength at various frequencies does not show any discontinuities against the number of cycles. The solid line is the best-fit curve obtained by linear regression analysis using a simple power law, and indicates the cyclic fatigue limit at 10^6 cycles is about 2/3 of the tensile strength at room temperature.

Static fatigue tests at room temperature were conducted in the same test frame under constant loading and generated the data given in Table 2. These static fatigue results are graphically compared to the cyclic fatigue data in Figure 6 as maximum applied stress is plotted against time to failure. The time to failure for the cyclic cases is made up of both loading and unloading portions. The arrow in the figure indicates that failure of specimen

did not occur when the test was terminated. Linear regression analysis of the log-log plot of static fatigue data, excluding the two runout points, determines that static fatigue failure can be satisfactorily described by a simple power law as $t_{sf} = 2.80 \times 10^{205} \sigma_m^{-85.87}$ (in hour and MPa), where t_{sf} is the failure time under a constant tensile stress, σ_m . The solid line is the best-fit curve for the static fatigue data and shows that the static fatigue limit is about 3/4 of the tensile strength. No scatter band could be defined for static fatigue data as only a limited number of data points were applied in the curve fitting. Figure 6 also indicates that specimens subjected to cyclic loading took a shorter time to failure than statically loaded specimens at the same maximum applied stresses.

3.2 High Temperature Results

Results of cyclic fatigue tests with $R = 0.1$ and different loading wave forms at 1200°C are given in Tables 3-6 and graphically shown in Figure 7 as a plot of maximum applied stress against number of cycles to failure. Fatigue lifetime was observed to increase with the decrease in applied stress for each cyclic wave form. No significant difference in cycle lifetime between sine and square wave forms under the same maximum applied loads was observed. In trapezoid I loading, the number of cycles to failure was slightly lower (by a factor of 2) than either sine or square wave loading. It is not considered a significant difference in fatigue testing. However, trapezoid II loading substantially reduced the number of cycles to failure by more than an order of magnitude compared to the previous three loading wave forms under a similar maximum stress. This comparison suggests that cyclic fatigue lifetime is cycle shape or time dependent at high temperatures.

Cyclic fatigue tests at 1200°C with a higher stress ratio, $R = 0.5$, were performed with a square wave form at 2 Hz to examine the effect of stress ratio on the cyclic fatigue properties of ceramics at high temperatures. These results are reported in Table 7 and

graphically compared to the results of square wave form with $R = 0.1$ in Figure 8. The S-N curves show that cyclically loaded specimens with a higher stress ratio took a smaller number of cycles to failure than those with a lower stress ratio.

Static fatigue tests at 1200°C were also performed in the same test machine under constant loads and produced the data given in Table 8. This data is graphically compared to the results of cyclic loading with $R = 0.1$ in Figure 9 where maximum applied stress is plotted versus lifetime on time base. Linear regression analysis of the log-log plot of static fatigue data, excluding the runout point, determines that static fatigue failure can be satisfactorily described by a simple power law as $t_{sf} = 5.72 \times 10^{14} \sigma_m^{-8.32}$ (in hour and MPa), where t_{sf} is the failure time under a constant tensile stress, σ_m . The correlation coefficient of the linear regression analysis is relatively high with a value of $R^2 = 0.941$. The slope of this best-fitting curve is then used to draw the upper and lower limit of static fatigue life which are shown as dashed lines in Figure 9. The horizontal width of this scatter band bounded by the two dashed lines is about a factor of 6. A similar approach (not shown in Figure 7) is also used for the cyclic fatigue data and indicates that the scatter range is about a factor of 6, 8, 6, and 10, respectively, for sine, square, trapezoid I, and trapezoid II loading wave forms with $R = 0.1$. The scatter of static and cyclic fatigue data in this study is apparently smaller than those using other testing methods (e.g. Refs. 4,7,8,39,40) and is attributed to the use of uniaxial tensile specimens with a larger portion of material under maximum stress.

The results of cyclic fatigue under square loading at stress ratios $R = 0.1$ and 0.5 are also compared to the static fatigue results as shown in Figure 10. Though the failure time was lower for cyclic loading with $R = 0.5$ than with $R = 0.1$ at low stress levels, it was still much longer than the lifetime under static loading at the same maximum stress. The scatter in the data of square loading wave form with $R = 0.5$ is approximately a factor of 8.

In the following chapter a linear elastic crack growth model is applied to examine whether cyclic fatigue failure can be attributed to the accumulation of static fatigue failure or if there exist some other cyclic effects on failure time.

4. LIFETIME ANALYSIS

Most of the mechanical failure of ceramic materials occurs from preexistent flaws. These preexistent flaws are introduced into the material during either processing or machining. Thus, the lifetime of many mechanically loaded ceramic structural components is restrained by subcritical crack growth of the preexistent flaws. Preexistent flaws may grow under constant or varying loading to critical sizes for spontaneous propagation and lead to failure of ceramic components during operation. This time-delayed failure within the planned operation time could be prevented by the lifetime prediction based on the preexistent flaw size distribution and the measurement of crack growth parameters.

4.1 Model for Prediction of Cyclic Lifetime

Subcritical crack growth in ceramics is usually described by the following power law[85]:

$$V = da/dt = AK_I^n = A(Y\sigma\sqrt{a})^n \quad (1)$$

where V is the crack velocity during crack propagation, a is the crack size, t is time, A and n are material constants which are functions of temperature and environments, K_I is the stress intensity factor, Y is a geometric factor, and σ is the applied stress. Assuming the failure mechanisms of static and cyclic fatigue are identical and fully time dependent; then the lifetime for cyclic loading can be predicted from the measured static fatigue data.

The applied stress, σ , which is a function of time, can be generally expressed as:

$$\sigma = \sigma_m f(t) \quad (2)$$

where σ_m is the maximum applied stress and $0 \leq f(t) \leq 1$ for tensile loading. The failure time, t_f , can be obtained from the integration of Eq. (1) as follows:

$$a_f^{(2-n)/2} - a_i^{(2-n)/2} = [(2-n)/2]AY^n\sigma_m^n \int_0^{t_f} [f(t)]^n dt \quad (3)$$

where a_i and a_f are the initial and final crack sizes. In most cases, $a_i^{(2-n)/2} \gg a_f^{(2-n)/2}$ due to $n \gg 1$; thus, the first term in the left hand side of Eq. (3) can be reasonably neglected compared to the second term. For static fatigue test with $f(t) = 1$, the static lifetime, t_{sf} , is given by the following approximation from Eq. (3):

$$t_{sf} \cong [2/(n-2)]A^{-1}Y^{-n}a_i^{(2-n)/2}\sigma_m^{-n} \quad (4)$$

For a fatigue test performed under a cyclic loading wave form with a period τ , the cyclic lifetime, t_{cf} , can also be obtained by simplifying Eq. (3) as follows:

$$t_{cf} \cong [2/(n-2)]A^{-1}Y^{-n}a_i^{(2-n)/2}\sigma_m^{-n}\tau \left\{ \int_0^\tau [f(t)]^n dt \right\}^{-1} \quad (5)$$

In Eq. (5), $t_{cf} = N_f\tau$ is used to get the approximation for $N_f \gg 1$, where N_f is the number of cycles to failure.

The ratio of cyclic fatigue to static fatigue lifetime under the same maximum applied stress, σ_m , is then given as:

$$r = t_{cf}/t_{sf} = \tau \left\{ \int_0^\tau [f(t)]^n dt \right\}^{-1} \quad (6)$$

The periodic function, $f(t)$, in each cycle for the cyclic loading wave forms used in this study can be expressed as follows:

(A) sine wave form:

$$f(t) = \frac{(1+R)}{2} + \frac{(1-R)}{2} \cdot \sin \omega t \quad (7)$$

where R is the stress ratio and $\omega = 2\pi/\tau$.

(B) square wave form:

$$f(t) = \begin{cases} 1 & \text{for } 0 \leq t \leq \frac{\tau}{2} \\ R & \text{for } \frac{\tau}{2} \leq t \leq \tau \end{cases} \quad (8)$$

(C) triangular wave form:

$$f(t) = \begin{cases} R + (1-R) \cdot \frac{2t}{\tau} & \text{for } 0 \leq t \leq \frac{\tau}{2} \\ 1 - (1-R) \cdot \frac{2(t - \frac{\tau}{2})}{\tau} & \text{for } \frac{\tau}{2} \leq t \leq \tau \end{cases} \quad (9)$$

(D) trapezoid wave form:

$$f(t) = \begin{cases} R + (1-R) \cdot \frac{2t}{t_u} & \text{for } 0 \leq t \leq \frac{t_u}{2} \\ 1 & \text{for } \frac{t_u}{2} \leq t \leq t_h + \frac{t_u}{2} \\ 1 - (1-R) \cdot \frac{2(t - t_h - \frac{t_u}{2})}{t_u} & \text{for } t_h + \frac{t_u}{2} \leq t \leq \tau \end{cases} \quad (10)$$

where $\tau = t_h + t_u$.

In the previous chapter, linear regression analysis of the room and high temperature static fatigue data has determined the crack growth exponent, n , a value of 85.87 at room temperature and 8.32 at 1200°C. Since n is not an integer in this case, an analytical solution can not be obtained for a sinusoidal wave form from Eqs. (6) and (7). Numerical analysis was used to calculate the integration in Eq. (6) using Eq. (7) for $f(t)$. However, for square, triangular, and trapezoidal wave forms, the analytical solution of r can be directly obtained from Eq. (6) substituting Eqs.(8), (9), and (10) into the integral, respectively. The calculated values of r are given in Table 9. As the experimental scatter of fatigue data in static and cyclic loading has been an important factor in the confusion of possible "true" cyclic fatigue of ceramics in some of the literature, the scatter in the static fatigue data at 1200°C is also taken into account on the prediction of high temperature cyclic fatigue lifetime.

4.2 Comparison of Measured and Predicted Cyclic Lifetime

The predicted cyclic fatigue lifetime is then plotted in Figure 11 for room temperature tests and in Figures 12-16 for tests at 1200°C. The predicted upper and lower bound of cyclic fatigue lifetime at 1200°C is based on the upper and lower bound of static fatigue data at 1200°C. If there is no apparent cyclic effect on the crack growth rate, the measured cyclic lifetime should be comparable with the predicted value from static fatigue data.

Figure 11 shows that cyclic fatigue lifetime at room temperature is much shorter than the predicted lifetime. This result is expected, as the measured cyclic fatigue lifetime falls below the measured static fatigue lifetime at the same maximum tensile stress and only a very small portion of the cyclic triangular loading is at the maximum load. Thus, the measured cyclic lifetime would be definitely much less than the predicted value based on

the static fatigue data. It is clear from this comparison that cyclic loading can accelerate the fatigue crack growth in this alumina at room temperature.

For high temperature tests with sine, square, and trapezoid I loading wave forms at $R = 0.1$ (Figures 12-14), the measured cyclic fatigue lifetime is beyond the upper limit of the predicted cyclic lifetime and the deviations increase with the decrease in applied stress level. The observed cyclic fatigue lifetime is about an order of magnitude larger than the predicted upper limit value at lower stresses for the sine and square loading tests. However, the data for trapezoid II loading wave form lie within the range of predicted cyclic lifetime from the static loading data as shown in Figure 15. It is obvious that cyclic lifetime under sine, square, or trapezoid I loading wave form is underestimated from the static fatigue data associated with the consideration of the scatter in the data. Failure mechanisms of cyclic loading with trapezoid II wave form might be similar to those of static loading as the cyclic lifetime is predictable from the static fatigue results.

The cyclic fatigue lifetime under square loading with $R = 0.5$ at 1200°C is also compared to the predicted lifetime as shown in Figure 16. The measured cyclic lifetime is still larger than the value of the predicted upper bound although the stress ratio is increased from 0.1 to 0.5.

The above comparisons of test results at 1200°C indicate that there is a beneficial cyclic effect at high temperature on failure time from repeated loading with a short duration of maximum stress (e. g. sine, square, and trapezoid I wave forms in this study) compared to static loading. The worst cyclic loading case with respect to failure time is a long hold time at maximum stress (e. g. trapezoid II in this work), but the lifetime is at least comparable to the static lifetime under the same maximum stress. The comparisons of results under square loading wave form at $R = 0.1$ and 0.5 show that the cyclic lifetime decreased with the increase of stress ratio, yet the effect of stress ratio on the failure time is apparently much less important than the effect of the hold time at maximum tensile stress.

The overall comparisons imply that cyclic loading is not more detrimental than static loading in the alumina under the high temperature testing conditions in this investigation.

5. DISCUSSION

The existence of any true cyclic fatigue effect at room and high temperatures in the selected alumina has been examined in the previous chapter. More detailed discussion of the cyclic effects at room and elevated temperatures will be given in this chapter.

5.1 Cyclic Effects at Room Temperature

The above results and lifetime analysis demonstrate the evidence of true cyclic fatigue in this alumina at room temperature. There was more strength degradation in cyclic loading than in static loading as the cyclically loaded specimens took a much shorter time to fracture than those under sustained constant loads at the same maximum stresses. The threshold stress level for cyclic fatigue ($2/3$ of tensile strength) was also lower than that for static fatigue ($3/4$ of tensile strength). Cyclic fatigue behavior of this alumina was mainly dependent on the number of cycles rather than on time, as the number of cycles to failure at a similar maximum stress was comparable in the tests of various frequencies (0.1 to 5 Hz). This deleterious cycle-dependent fatigue behavior at room temperature is similar to that of metal fatigue. It is therefore inappropriate to attribute the current results of cyclic fatigue exclusively to the failure mechanism (such as environmental stress corrosion) that controls static fatigue behavior, as the tests for cyclic and static fatigue were conducted in the similar lab conditions in a random order.

Direct measurements of fatigue crack growth rates in a 99.5%-pure polycrystalline alumina at room temperature using tapered double cantilever beam (TDCB) specimens have been recently reported by Reece et al.[22] The crack velocities under cyclic loading in that alumina could be expressed by a power law, $da/dN=A(K_{max})^m$. The cyclic crack growth was found to be substantially faster than the static fatigue crack growth for the same K_{max} , and to occur at the K_{max} values lower than the threshold K_{max} for static fatigue. The crack

extension per cycle (da/dN) determined at 5 and 10 Hz was also found to be comparable and independent of frequency. Those observations by Reece et al.[22] show similar trends in room temperature fatigue behavior of alumina as observed in the present study. It is obvious that, at room temperature, there indeed exists in some ceramics a genuine cyclic fatigue effect which is cycle dependent rather than time dependent.

5.2 Cyclic Effects at High Temperatures

The literature survey shows a limited number of studies that directly compared static and cyclic fatigue data at elevated temperatures for alumina,[60,61] silicon nitride,[9,10,64-66] silicon carbide,[10,13] and alumina-matrix ceramic composite.[60-62] In those studies only a sinusoidal or triangular wave form was used as the cyclic loading pattern. In this section the current observations will be compared with other researchers' investigation on the influence of cyclic loading on the fatigue behavior of ceramics at elevated temperatures.

It is noted that the lifetime prediction method discussed in the previous chapter is based on the assumption that both cyclic and static fatigue failure mechanisms are identical and dominated by subcritical crack growth and the stress intensity factor, K_{Ic} , is the only dependent variable in describing the crack velocity during slow crack propagation. The literature is conflicting regarding this assumption.

For example, Evans et al.[9] subjected a silicon nitride to static loading and cyclic loading with frequency < 5 Hz at 1400°C , and found that there was no enhanced cyclic effect on the slow crack growth rate as the measured cyclic crack velocity was predictable from the static velocity data. That observation provides a verification for the assumption that cyclic crack growth is essentially due to the static crack growth mechanism. Similar observations were also reported by Kawai et al.[10] on a silicon carbide and a silicon nitride. S-N curves were established for silicon nitride up to 1200°C and for silicon

carbide up to 1400°C with the application of uniaxial tensile tests in both static and cyclic loading. The cyclic loading tests were conducted at $R = 0.5$ and under a triangular wave form with the period of a loading cycle ranging from 1 to 7 mins as the stressing rate was kept constant at a value of 0.6 MPa/s. Within the scatter of the data, no true cyclic fatigue effects could be discerned either for silicon nitride at 1000°C, 1100°C, and 1200°C or for silicon carbide at 1400°C as the predicted cyclic lifetime agreed very well with the measured data. It was therefore concluded that delayed fracture in both static and cyclic fatigue for those two ceramic materials at high temperatures were essentially caused by slow crack growth with no interactions of any cyclic effects.[10]

In contrast, this assumption becomes invalid for another silicon nitride under bending tests at 1200°C in a study reported by Fett et al.,[64] where the prediction based on static loading data substantially underestimated the measured cyclic lifetime under a sinusoidal loading wave form with a frequency of 30 Hz. The observations of Fett et al.[64] imply that cyclic fatigue mechanism is not entirely similar to the static fatigue mechanism in that particular silicon nitride at high temperatures.

The current test results demonstrate both phenomena regarding the assumption that cyclic fatigue is primarily attributed to static crack growth mechanism. For the alumina under the test ranges in this study, failure time for the trapezoid II loading wave form (with a longer hold time at maximum stress) can be predicted from the measured static lifetime. This is similar to the observations of Evans et al.[9] and Kawai et al.[10] On the other hand, measured cyclic lifetime in sine, square, and trapezoid I loading wave forms (with a short duration of maximum stress and higher loading rate) is much larger than the predicted value from static loading data. This phenomenon has a strong resemblance to the results of Fett et al.[64]

Some recent results obtained by Masuda et al.[65,66] on silicon nitride showed similar trends in the cyclic lifetime at high temperatures to those observed in the current study. In their investigation, the measured cyclic lifetime was obtained from the uniaxial

tension-compression test ($R = -1$) under a sinusoidal wave form with a frequency of 20 or 0.01 Hz at 1000°C. Their results demonstrated the dependence of cyclic lifetime on frequency at high temperatures. At 20 Hz, the measured cyclic lifetime was much larger than the predicted value based on the static fatigue data and slow crack growth model. However, the cyclic lifetime with a frequency of 0.01 Hz was within the range of the predicted lifetime from the experimental data under static loading.[65,66]

The above comparison indicates that in addition to slow crack growth, other high temperature mechanisms such as creep, microstructural instabilities, and/or a mechanical cycle effect need to be considered in lifetime prediction for ceramics at elevated temperatures. Even though Fett et al.[64] considered the effect of stress redistribution due to creep in bending tests, the measured cyclic lifetime is still much larger than the modified prediction. A further consideration of the adhesive effects of the viscous grain-boundary phase on the crack surfaces was proposed to explain the deviations between predictions and measurements.[64] The effect of the viscous boundary phase may also be applied to explain the observations in this study. Detailed evidences of the viscous glassy phase for the alumina selected in this study will be given in next chapter.

For the cyclic cases with high stressing rate or a short duration of maximum stress, such as the sine, square, and trapezoid I wave forms in this study, the viscous glassy phases would carry a part of the applied load by bridging the crack surfaces. These adhesive forces from glassy phases would reduce the effective stress intensity factor in calculating the crack propagation velocity given in Eq. (1) and retard the crack growth. In the case of static loading or cyclic loading with lower frequency or a longer hold time at maximum stress, such as the trapezoid II loading wave form in this study, these effects on the crack opening behavior may disappear after the initial loading in each cycle due to the relaxation characteristics of the viscous glassy phases. The definitions of low or high frequency and short or long hold time at maximum stress for cyclic loading are dependent on material, temperature, and environments. For instance, 2 Hz might be a high frequency

value for the alumina tested in this study, while it may be classified as low frequency for the silicon nitride investigated in the study of Evans et al.[9] A simplified model in calculating the effective stress intensity factor at the crack tip with the consideration of the bridging effect by the viscous glassy phase behind the crack tip will be addressed in details in a later chapter.

Recently, Suresh and co-workers measured the static and cyclic (sine wave form) crack growth rates for an alumina (0.13 and 2 Hz at 1050°C)[60,61] and a silicon carbide reinforced alumina matrix composite (0.1 and 2 Hz at 1400°C).[60-62] Cyclic loading was found to give rise to a lower crack growth rate compared to static loading under the same maximum stress intensity factor for both ceramics in their studies. They also observed that higher cyclic frequency (2 Hz) caused more crack growth retardation than lower cyclic frequency (0.13 or 0.10 Hz) in both materials. One of the contributions to the improved cyclic fatigue resistance is due to the bridging of crack surfaces by the inherent boundary glassy phases in monolithic alumina[60,61] or the in situ formation amorphous glassy phases arising from the oxidation of SiC whisker in the composite ceramics.[60-62] Again, those observations[60-62] imply that adhesive effects from glassy phases would diminish with a decrease in cyclic frequency. Han and Suresh[62] also suggested that another reason for improved cyclic fatigue was the cyclic loading specimen had a smaller portion of time at the maximum tensile stress than did the static loading specimen. This is not the case in the present work, as the total lifetime at maximum stress for the cyclic specimens under square or trapezoid I loading wave form is still much longer than the failure time of static specimens under a similar maximum stress.

It is obvious from the current observations that the duration of maximum tensile stress in a cycle is a critical parameter in determining the cyclic lifetime. Once this hold time at maximum tensile stress exceeds a particular value, the cyclic loading no longer has a beneficial effect on lifetime compared to static loading. Additionally, the retardation of crack growth for cyclic loading with a short duration of maximum stress is more

pronounced when the thickness of the boundary phase becomes comparable with the crack tip opening displacement. This could explain the larger deviations in measured lifetime between static loading and cyclic loading with a short duration of maximum stress at lower applied stress levels where the crack tip opening displacement is smaller and closer to the size of glassy phase thickness.

Creep mechanisms are another contributor to the failure of ceramics at elevated temperatures. In a recent study by Page and Lankford,[63] the creep behavior of a silicon carbide with a glassy phase and an alumina without glassy phase under cyclic compressive loading was investigated. The compressive creep testing was conducted at 1600°C under a symmetrical trapezoid loading wave form (the hold times at maximum and minimum stresses were identical as were the loading and unloading rates) with a frequency of 0.33 Hz. The cavitation rate and the minimum creep rate in the silicon carbide was found to be controlled by the total amount of time at maximum compressive stress and unaltered by the cyclic loading. The formation of creep cavitation for ceramics with glassy phases is through the viscous pore growth; hence 0.33 Hz is probably too slow to generate any cyclic effect on cavitation in this silicon carbide.[63] However, larger cavity size, higher cavity volume fraction and a slightly lower cavity density were found in alumina, yet no cyclic effect on the minimum creep rate was observed. For the alumina without glassy phase, creep cavitation occurs by means of grain-boundary diffusion; thus 0.33 Hz is fast enough to keep the transient stress concentration due to grain-boundary sliding in each cycle to accelerate the growth of cavitation.[63] Page and Lankford[63] also claimed that, in ceramics with glassy phases, cavitation might increase with the increasing cyclic frequency due to the transient stresses. In the present study, failure time is found to increase with the increasing cyclic frequency or shorter hold time at maximum stress in contrast to the expected increasing cavitation. This comparison suggests that most of the failure time of the alumina under the testing conditions in this investigation was consumed by slow crack growth rather than by the nucleation and growth of cavities. This would

also support the earlier postulation that glassy phases would generate different influences on the crack opening behaviors in static loading and cyclic loading with different cycle shapes or frequencies.

5.3 Comparison of Cyclic Effects at Room and High Temperatures

As noted above, the observed cyclic fatigue effects at both room and high temperatures could not be explained by the accumulation of the static fatigue damage through an integration over the cyclic loading history. It is apparent that the alumina selected by this study indeed demonstrates the existence of a true mechanical cyclic effect at room temperature and this cyclic loading effect is more detrimental on failure time than static fatigue at the same maximum stress. This cyclic effect at room temperature is independent of cycle frequency. Under certain conditions, however, cyclic loading at high temperatures caused a beneficial effect on fatigue lifetime as opposed to sustained constant loading. The cyclic effect at high temperatures is cycle-shape or time dependent. Once the hold time at maximum stress reaches a specific value, there is no longer a beneficial cyclic effect and the cyclic lifetime becomes predictable from the static loading data. The above discussion indicates that the characteristics of cyclic loading effects in ceramics are also temperature dependent. The cyclic loading which is more deleterious than static loading at room temperature may not be more damaging than static fatigue at high temperatures in ceramics.

The above comparisons of the present work with the previous studies suggest that cyclic fatigue of ceramics containing viscous boundary phases might not be such a severe problem at elevated temperatures as it is in the metals with creep-fatigue interactions. These comparisons also provide the clues for explanation of the two distinct observations in the previous studies with respect to the existence of any cyclic effect in ceramics at elevated

temperatures. The generation of the two distinct conclusions could be attributed to the difference in cyclic loading procedure, in particular the cycle frequency and cycle shape.

A detailed failure analysis for the alumina fractured at the given stress-temperature conditions in the current work is given in the following chapter to characterize the cyclic fatigue mechanisms at both room and high temperatures.

6. FAILURE ANALYSIS

A comprehensive microstructural analysis of the fractured specimens in the present study was conducted and elucidated in the current chapter. Both room and high temperature specimens, fractured at different loading conditions, were examined with SEM and TEM to investigate the fatigue mechanisms for the alumina chosen in this study.

"As-received" specimens were prepared from an axial section cut from an as-received cylindrical rod for both SEM and TEM analysis to obtain the undeformed microstructural information for future comparison. The inherent processing pores are primarily seen in the areas such as triple-point junctions and two-grain interfaces, as evidenced by Figure 17. The glassy grain-boundary phase in this material is generally discontinuous and non-uniformly distributed; i.e., it exists in the form of isolated zones. Most of the glassy phase is confined to triple-point junctions and occasionally seen at two-grain interfaces (Figure 18).

6.1 Scanning Electron Microscopy Observations

Post-failure fractographic analysis is performed with SEM. Specimens were cut from the broken gage sections parallel to the fracture surface. In addition, some specimens, from each loading path with high, intermediate, and low maximum applied tensile stress, were axially sliced into four sections parallel to the loading direction. Each sliced internal section was then mechanically polished for SEM examination to explore possible evidence for the development of high temperature fatigue damage. Before SEM examination, each specimen was ultrasonically cleaned and sputteringly coated with gold-palladium.

6.1.1 Room Temperature Fracture Patterns

Figure 19(A) is the fracture surface of a room temperature cyclic fatigue specimen. A fracture mirror (the semicircular flat region indicated by dashed lines) was found around the surface-initiated fracture origin. Beyond the fracture mirror is a small region with small radial ridges or flakes, which is called mist. Mist region typically merges into the next region called hackle. The hackle region is associated with similar larger ridges and river patterns, and transitions into the macroscopic crack branching region which is the remaining portion of the fracture surface. The details of mirror-mist-hackle- crack branching features in ceramics are described and discussed in elsewhere.[86,87]

The semicircular mirror region in Figure 19(A) represents a period of stable crack growth. No precise crack nucleation sites could be consistently identified in this region for the cyclic fatigue specimens at room temperature, yet the general locations could be found. Fast fracture then occurred outside the semicircular flat region and was characterized by a rough surface and "river patterns". Although the stable slow crack growth regions and the overload zones are macroscopically distinguished at low magnification, no significant microscopic differences in features could be discerned at high magnification as shown in Figures 19(B) and (C). Both regions show a mixed intergranular/transgranular fracture mode. Cleavage steps as well as inherent processing pores were occasionally seen on the fracture surface in both regions. Figure 20(A) is an example of the typical processing voids within the grains and along the grain boundaries. Figures 20(B) and (C) are the higher magnification micrographs of the cleavage facets associated with the internal and boundary processing pores, respectively. Figure 20(D) is a clear example of a transverse transgranular crack through the fracture surface.

Size of the semicircular flat area and the maximum stress applied during the fatigue cycle were applied to estimate the fracture toughness of this selected alumina and examine whether this zone truly indicates a period of slow crack growth. The details of the

calculation procedures and discussion have been reported in a previous study by Mayer.[59] The calculated values of the fracture toughness for this alumina were comparable with other published data (at the same order of magnitude). It is therefore concluded that this semicircular flat region is characteristic of the slow crack growth.

Figure 21 shows the features of the fracture surface in a specimen failed under a constant load at room temperature. The macroscopic features (see Figure 21(A)) are similar to those observed in cyclic fatigue specimens demonstrating the mirror-mist-hackle-crack branching fracture patterns. The exact fracture origin in flat region could not be consistently identified for the static fatigue specimens. Again, no apparent distinctions in the features of the fracture surface between the stable crack growth and fast fracture regions could be made at high magnification as shown in Figures 21(B) and (C). The failure mode in both regions is mixed with intergranular and transgranular cracking. Although the mechanical testing results implied that cyclic and static fatigue might be inherited from distinct mechanisms, it was not possible to distinguish any major difference between the fracture surfaces generated by either loading conditions. Both fracture surfaces also contained fracture debris around the crack branching areas as shown in Figure 22. Similar observations of fracture debris in both static and cyclic fatigue specimens at room temperature were also reported by Reece et al.[22]

Some specimens from both static and cyclic loading tests were axially sectioned, polished, and examined with the SEM to seek possible evidence of the development of fatigue damage. As shown in Figure 23, no formation of any macrocrack except the primary failure crack was noted throughout the gage section of each sectioned static and cyclic loading specimen. It is suggested that failure of the alumina, tested under both sustained and cyclic tensile loading at room temperature in this investigation, was controlled by the formation and growth of a single primary crack from the dominant preexistent surface-connected flaw rather than by simultaneous nucleation and/or growth of

multiple macrocracks. Furthermore, it is important to note that some kind of "process zone" developed by dispersed microcracks in front of a crack tip was not detected.

Figure 23(B) also demonstrates crack branching from the primary failure crack in a cyclic fatigue specimen. With careful documentation of orientation in this sectioned specimen, it is found that the location where the crack branching began lies within the catastrophic fracture region in the fracture surface as shown in Figure 19(A). Crack deflection was often recognized in the crack paths for the branching cracks as shown in Figure 24(A). In addition, these crack paths show evidences of interlocking grains, contact of crack surface asperities, unbroken ligaments, and trapped grains within the closed crack (see Figures 24(B)-(E)). These events along the crack paths are the candidates for the primary sources of the crack-interface traction behind the crack tip and shield the crack tip from the applied stress. These observations might also provide a reasonable explanation for the cyclic fatigue mechanisms in the selected alumina at room temperature. Details of discussion on the cyclic fatigue mechanisms at room temperature will be given in a later section.

6.1.2 High Temperature Fracture Patterns

Figure 25(A) shows the typical mirror-mist-hackle-branching fracture surface of the specimens that were cyclically loaded with sine wave form at 1200°C. The macroscopic features are similar to those in room temperature specimens. However, the size of the semicircular mirror region is much larger in this high temperature specimen due to the lower applied maximum stress. Furthermore, the features of the slow crack growth region at higher magnifications are indistinguishable from those in the catastrophic fracture zone as shown in Figures 25(B) and (C). Both slow crack growth and fast fracture regions show that intergranular cracking is the predominant fracture mode except at some large grains where transgranular crack growth occurs. This is the major difference in fracture surface

between the room temperature and high temperature specimens. At high temperatures the grain-boundary phases would become viscous and less energy was needed for the crack to go around the grains than through a grain. Thus, intergranular cracking is more prevalent in high temperature fractured specimens.

The macroscopic features of the fracture surface of cyclic specimens under square ($R = 0.1$ and 0.5), trapezoid I and II loading wave forms at 1200°C are shown in Figures 26 to 29. No consistent mirror-mist-hackle-crack branching fracture patterns were observed in these specimens, but they still showed both flat and rough regions. At higher magnifications, no notable microscopic differences in fracture features were observed between flat and rough regions for these cyclic cases. Moreover, similar to the case of the sine wave form, intergranular crack growth is the prevalent fracture mode throughout the fracture surfaces in these specimens except at the areas with large grains.

For the static fatigue specimens, again, no mirror-mist-hackle-crack branching fracture patterns could be identified. Figure 30(A) shows the fracture surface of a specimen failed under a low constant load at 1200°C . It is suspected that the origins of the failure in this specimen occurred near or at the edge of the fracture surface and were associated with rough areas (marked by R1-3 in Figure 30(A)) as opposed to the cyclic case of sine wave form where a semicircular flat region was found to surround the sole failure origin. Stable crack growth of this static fatigue case is characterized by the rough surface while the flat surface represents a fast fracture region. In addition to the major rough area (R1), some other smaller rough areas (R2,R3) were also recognized. These smaller rough areas might be characteristic of slow crack growth of other cracks. More evidence for this argument will be given later in the observations of the axially-sectioned specimens. However, no such multiple isolated rough areas were observed in the static fatigue specimens at high levels of applied stress. No significant microscopic differences in fracture features at higher magnifications could be seen between the rough and flat zones

(see Figures 30(B) and (C)). Both regions show that intergranular cracking is the dominant mode of fracture except at large grains.

Typical failure origins, where they could be clearly identified, for static and cyclic fatigue specimens are shown in Figure 31. These include processing flaws such as large pores near or at the edge of the fracture surfaces (Figures 31(A) and (B)), and large-grained agglomerates (Figure 31(C)).

As described in an earlier chapter, the improved fatigue resistance in cyclic loading with higher frequency or a shorter duration of maximum tensile stress may be due to the adhesive effects of viscous boundary phases. Typical profiles of the viscous glassy phases observed on the fracture surfaces of various specimens are demonstrated in Figure 32. The different structures of the sporadic viscous glassy phase indicate that the glassy phase is discontinuous and mostly confined to the channels along three-grain junctions or isolated at four-grain junctions. Figures 32(B) and (C) show the features of a finger-like perturbation observed in the specimens under trapezoid II and static loading at low stress levels. The finger-like structure is thought to be the consequence of the creep cavity growth through the viscous liquid meniscus propagation along a two-grain boundary.[69,70] However, those grain facets without spread viscous boundary phase look similar to those in fracture surfaces of room temperature specimens as shown in Figure 33. No additional damages such as diffusional cavities could be recognized on the grain facets for the high temperature specimens. Furthermore, grain-boundary sliding or grain rotation due to diffusional creep was occasionally observed in the grains within the area without the glassy phase for the specimens of trapezoid II and static loading tests at low applied loads (Figure 34). However, no such creep-related features were noticed in the specimens under sine, square ($R = 0.1$ and 0.5), and trapezoid I loading wave forms at all applied stress levels, as well as in the specimens under trapezoid II and static loading at high stresses.

No other crack except the primary failure crack was detected in each axially-sliced internal section for cyclic cases with sine, square ($R = 0.1$ and 0.5), and trapezoid I loading

wave forms at all applied stress levels (Figure 35(A)). It is suggested that failure of the alumina subjected to these cyclic tensile loading patterns at 1200°C was dominated by the formation and growth of a single primary crack rather than by simultaneous nucleation and/or growth of multiple cracks. However, examination of the axially-sliced sections in the static fatigue specimens of low stress levels (below or equal to 48.3 MPa in maximum stress) revealed the existence of few small cracks (of the order of 100 μm) in addition to the fracture plane of the specimen (Figure 35(B)). These non-failure-induced small cracks seem to initiate at or near the outer surface rather than at the deeply inner locations. Thus, the failures of static fatigue specimens tested under the low loading conditions in this study might occur by simultaneous nucleation and/or growth of multiple cracks. This is supported by the observations of many isolated rough areas (stable crack growth regions) in the fracture surface of the same static fatigue specimen as shown previously in Figure 30. The sectioned specimens of trapezoid II cyclic loading wave form at low maximum stress levels ($\sigma_{\text{max}} \leq 48.3 \text{ MPa}$) also demonstrate the existence of few small cracks in the gage section. Such phenomenon was not observed in the axially-sliced sections of the specimens under static and trapezoid II loading at high loading levels. This similar appearance in fracture pattern between trapezoid II and static loading implies that the failure mechanism for cyclic case with a long hold time at maximum stress is possibly similar to the case of static loading. This can be supported by the stress-life results in which the lifetime of trapezoid II cyclic loading wave form agrees reasonably well with the predicted value from static fatigue data.

In comparison to the as-received material, no visible bulk creep damage such as extensive crack-like cavities or grain-sized microcracks was observed throughout the gage sections in all examined static and cyclic loading specimens. Moreover, a damage zone comprised of intense grain-sized microcracks and crack bifurcation at the crack tip of the unfailed small cracks or along the crack tip wake of both the primary failure crack and unfailed cracks could not be detected in sectioned static and cyclic SEM specimens (Figures

35(C) and (D)). However, examples of the viscous boundary phases bridging the crack surfaces did exist, and they are shown in Figure 36. These observations provide the evidence for the postulation that the improved fatigue resistance for cyclic loading with a short duration of maximum tensile stress may be attributed to the crack bridging effects produced by the viscous glassy islands behind the crack tip.

6.2 Transmission Electron Microscopy Observations

For TEM examination, 3-mm-diameter disks were cut out from some of the axially-sliced internal sections as mentioned earlier in the preparation of SEM specimens, and thin foils were prepared using standard procedures including mechanical polishing, dimple grinding, and then ion milling.

6.2.1 Room Temperature Phenomena

Figure 37 demonstrates the typical TEM views of the areas near the fracture plane in the axially-sliced gage sections for both static and cyclic loading specimens. No significant differences in the TEM micrographs of the failed specimens between these two loading paths. These TEM micrographs are also indistinguishable from the micrographs of the as-received material. Plastic deformation such as dislocation activity was never detected in these room temperature specimens. The search for the existence of dispersed microcracks was not successful in all examined room temperature TEM specimens. These results in conjunction with the SEM observations suggest that microcracking might not be the major failure mechanism for both static and cyclic fatigue specimens failed at room temperature. Other mechanisms, particularly, responsible for the failure of the static fatigue specimens, if they exist in the vicinity of the crack tip, could not be recognized under the current examination methods.

6.2.2 High Temperature Phenomena

As noted previously in the SEM observations, no distributed stress-induced microcracks of the order of the grain size could be discerned throughout the internal gage sections of the static and cyclic loading specimens tested at high temperatures, although the gage section undergoes a uniform tensile stress distribution. Similarly, no enhanced micron-sized cavities were detected at the triple-point junctions or two-grain interfaces in the TEM specimens obtained from the areas immediately ahead of the non-failure-induced crack tip, as compared to the as-received material in which some inherent pores have been present at such junctions. These observations, combined with the SEM examination, suggest that the crack-tip damage zone, if it exists in this alumina under the high temperature testing conditions of the current study, might be small-sized and mostly associated with isolated cavities (inherent and/or stress-induced) rather than with non-coplanar extensive microcracks or coalesced cavities. However, when TEM specimens were prepared from material near the fracture plane in sliced sections of the static fatigue and trapezoid II loading specimens at low applied stresses, cavity linkage was occasionally observed in few localized spots as shown in Figure 38(A) in which two of the adjacent triple-point cavities has been connected by cavity growth through the two-grain boundary and the linkage with the third one might be in progress. Such an event was not observed in the TEM specimens of other high temperature static and cyclic loading conditions (Figure 38(B)). Consistent with the corresponding SEM observations, the rotation of an alumina grain in a static loading specimen at a stress level of 34.5 MPa is demonstrated in Figure 39, suggesting that creep process such as grain-boundary sliding might occur under these loading conditions.

In ceramics with continuous amorphous second phases, creep cavity is thought to nucleate in the triple junctions and then extend along two-grain interfaces.[67,69,70,78] Although the alumina tested in the current study did not contain a continuous second phase,

isolated zones of glassy phase existed in the triple or four-grain junctions and occasionally along two-grain boundaries. The SEM micrographs of the finger-like viscous glassy phase (Figures 32(B) and (C)) implied that cavity extension might occur at some localized sites by the presence of the viscous glassy phase in the specimens of trapezoid II and static loading tests at low stress levels. As the creep cavity emanates from triple junction and grows along the two-grain boundary filled with a thin layer of viscous amorphous phase, the liquid meniscus continuously increases its propagating velocity along the "channel" until it becomes unstable and causes the formation of a finger-like perturbation.[69,70] Figure 40 is a TEM micrograph of the bridging of two alumina grains by a finger-like viscous glassy phase, as discrete finger tips (or cavity fronts) can be identified within the crack-like cavity.

It should be noted that distinction between the inherent processing pores and stress-induced cavities at grain boundaries could not be achieved in this study from the SEM or TEM examination. Moreover, density of the cavities or pores of detectable size in all examined high temperature failed specimens was unchanged or only negligibly enhanced in comparison to as-received materials. It is therefore suggested that cavity growth from the inherent processing pores might be more important than the nucleation of new cavities, when one considers the high temperature failure mechanisms in this alumina ceramic. The above observations suggest that creep processes may not be intensely operative under the given stress-temperature conditions in the present work.

6.3 Failure Mechanisms

It is well established in metallic materials that the rising crack resistance with the crack growth is attributable to an increasing size of a plastic zone at the crack tip under plane stress conditions along with macroscopic blunting of the crack tip at the incipience of crack extension. Similar plastic zone could not be found in brittle ceramics and therefore other toughening mechanisms of crack tip shielding have been proposed for the increased

toughness and associated R-curve in ceramics.[88,89] These extrinsic toughening mechanisms include:[88,89] (1) crack deflection and meandering; (2) zone shielding (e.g. a "process zone" seen as a region of microcracking or transformation ahead of the crack tip and around the crack surfaces); (3) contact shielding (e.g. wedging, bridging between crack surfaces).

A process zone of stress induced microcracking in the vicinity of the crack tip has been proposed as a major mechanism for the toughening and consequent source of R-curve behavior in non-transformation and non-cubic polycrystalline ceramics such as alumina.[90,91] Dispersed microcracks can take place in the residually-strained field of a primary crack due to the internal residual tensile stresses from thermal expansion anisotropy or elastic mismatch,[90] and generate crack tip shielding results. However, recent observations[92-96] indicated that some activities behind the crack tip instead of the frontal microcrack cloud were responsible for the major toughening and R-curve behavior of alumina. These behind-crack-tip effects include frictional interlocking and grain bridging of the crack surfaces[93-96] at room temperature and adhesive forces caused by the secondary phase at high temperatures.[94]

Crack extension behavior under cyclic loading in the materials exhibiting the crack tip shielding toughening mechanisms was also generally discussed by Ritchie.[88] To date, limited evidence for the existence of true cyclic fatigue in ceramics at room temperature has been supported in literature, yet there is still wide speculation regarding the possible cyclic fatigue mechanisms in ceramic materials. These proposed mechanisms for alumina ceramics at room temperature include: (1) plastic indentation and lateral cracking due to asperities contacting on crack surfaces;[6] (2) crack closure effects due to the crack wedging by debris particles or asperities;[6,19] (3) microcrack formation and coalescence ahead of the main crack tip;[6] (4) bridging by the interlocking grains at the crack surfaces behind the crack tip;[7] (5) friction heating at the crack tip resulting in the local weakening

of the boundary glassy phases and intergranular failure.[4] However, the conclusive data to support any of the proposed mechanisms is still indirect and inadequate.

At elevated temperatures, ceramics become physically and/or chemically unstable. Critical fracture might occur through a process involving the nucleation, growth, and coalescence of cavities as a result of bulk diffusion or viscous flow of a grain boundary phase.[67-82] Consequently, crack nucleation and propagation in ceramics at elevated temperatures are attributable to creep mechanisms under certain conditions. However, very little is known about the cyclic fatigue mechanisms in ceramics at elevated temperatures due to the inadequate studies in this area. Based on the SEM and TEM observations in the previous two sections, the cyclic fatigue mechanisms of the alumina selected in the current study at room and elevated temperatures will be discussed in the following sections.

6.3.1 Fatigue Mechanisms at Room Temperature

As described in the previous sections, process zone of microcracking around the crack tip and along the crack wake regime was not found in the alumina under the given room temperature testing conditions in this study. This promotes the question: *What are the fundamental conditions for the existence of a microcracking process zone at room temperature?* The spontaneous microcracking was thought to take place upon initial cooling in alumina and other non-cubic and high thermally anisotropic ceramics above a critical grain size, l_c , while an activated microcracking process zone might occur in a transition region of grain size, $l^* < l < l_c$. [97-99] Below the transition grain size, l^* , no spontaneous or activated microcracking is expected to occur. Furthermore, the crack growth resistance or toughness is also expected to increase with the grain size in the range $l^* < l < l_c$ and to reach a peak value at $l = l_c$ above which the fracture toughness will diminish with the increase in grain size.[97,98] The value of l_c for alumina was estimated as 100 μm [99] which was comparable with the observed critical grain size corresponding to the maximum

fracture energy.[100] The lower limit of the grain size, l^* , for the existence of microcracking process zone was determined as about $0.4l_c$:[97,98] i.e., dispersed microcracks may occur around a primary crack when the grain size reaches about 40% of the grain size needed for generation of spontaneous microcracking during cooling. It is therefore suggested that the presence of microcracking process zone around a primary crack at room temperature would not be anticipated in alumina with the grain size below 40 μm .

With the failure to obtain experimental evidence for distributed microcracks throughout the gage sections of axially sectioned specimens, and with the nominal grain size of the selected alumina, 6 μm , much less than the estimated transition grain size, 40 μm , for initiation of a microcracking process zone around a primary crack, other mechanisms need to be considered and employed to explain the cyclic fatigue phenomena in the present investigation.

The toughening and R-curve behavior for the alumina with no observed microcracking process zone have been attributed to other behind-crack-tip effects such as crack bridging due to interlocking grains or unbroken ligaments and friction of the crack surfaces.[93,96] These behind-crack-tip effects shield the crack tip from the externally applied stresses. Knehans and Steinbrech[92] reported that the rising R-curve behavior terminated and the toughness of an alumina returned to its original level after cutting out the crack or renotching to just behind the extended crack tip by careful sawing, implying that some mechanism behind the crack tip induced the rising R-curve. The in situ observations of the crack growth in alumina, reported by Swanson et al.,[93,95] demonstrated the existence of some active grain-localized bridges of interlocking grains or unbroken ligaments at the primary crack interface, which generated restraining forces acting across the crack surfaces.

The earlier SEM observations on the fracture surfaces and axial cross sections of gage sections for static and cyclic fatigue specimens tested at room temperature indicated that the failure in both cases occurred by the slow crack growth of a single macrocrack

which likely originated from a preexistent flaw at or near the outer surface. This is similar to the general trends observed in fine-grained alumina with a grain size less than the transition value, l^* , where fracture occurs by the growth of a predominant flaw rather than by the formation and coalescence of microcracking.[98] It is therefore suggested that crack propagation may be the controlling factor in determining the fatigue lifetime of this selected alumina at room temperature. This also implies that crack growth is faster under cyclic loading than it is under static loading, as the static fatigue specimens took a much longer time to fail than the cyclic fatigue specimens under the same applied maximum loads. Hence, the application of the behind-crack-tip effects to explain the deleterious cyclic fatigue effect at room temperature is possible and reasonable.

Those behind-crack-tip effects responsible for the crack growth resistance behavior were mostly observed under quasi-static loading conditions. However, very few direct observations exist with regard to what effect cyclic loading might have on the behind-crack-tip events and the associated crack tip shielding mechanisms in ceramics. For a true detrimental cyclic fatigue effect to exist in ceramics, the effective stress intensity factor at the crack tip during cyclic loading needs to be higher than that in static loading, or there exist some kind of irreversible mechanisms, at or behind the crack tip, which would make the failure of ceramics easier during cyclic loading. In the following paragraphs, a qualitative interpretation of the failure mechanisms for the damaging cyclic fatigue effects at room temperature in the present work will be given and based on the SEM and TEM observations and the behind-crack-tip activities noted above.

Evidence to support the existence of some kind of behind-crack-tip effects in this selected alumina at room temperature has been shown in a previous section. Figures 24(B)-(D) illustrate the existence of crack bridging due to interlocking grains, frictional interlocking of asperities, or unbroken ligaments in this selected alumina. These interlocking grains stick to the alumina "matrix" on either side of the crack surface behind the crack tip as a result of the internal residual compressive stress between grains due to

thermal expansion anisotropy. The frictional interlocking of the asperities was attributed to the rough fracture surfaces or serrated grains. These load bearing bridges may be permanently ruptured due to the irreversible frictional sliding and wear processes under repeated loading and the crack extension is then enhanced. In cyclic loading, the frictional resistance between the interlocking grains and alumina "matrix" is reduced and the wearing of the surfaces of the interlocking grains is enhanced. This bridge degradation mechanism due to the decrease in frictional tractions has been confirmed in a recent study by Lathabai et al.[101] with the in situ observations of the development of bridging sites along the crack surfaces during cyclic loading tests. As the crack growth continues, if the crack opening displacement is larger than the grain-localized crack surface roughness at a local interlocking grain, the interlocking grain will extricate from the alumina "matrix" and bridging is no longer possible and will translate with the crack. Figure 24(E) is a clear example of the pull-out small interlocking grains trapped within the closed crack. Trapping of these debonded grains and associated debris inside the crack surfaces is thought to be another damaging mechanism in cyclic loading. The wedging action of these pull-out grains or asperities between the crack surfaces will affect crack closure during the reducing part of the load cycle by increasing the local stress intensity factor at the crack tip and generating crack-tip opening, as these ceramic grains are too hard to deform plastically.

It is therefore concluded that the exhibitions of the static and cyclic fatigue behavior in this selected low toughness alumina ceramic at room temperature are primarily attributed to the crack-tip shielding from combination of various behind-crack-tip activities. These behind-crack-tip events that impart toughness can degrade under repetitive loading and unloading and induce the cyclic fatigue effect at room temperature.

6.3.2 Fatigue Mechanisms at High Temperatures

Failure of ceramics under constant loading at high temperatures usually occurs by slow crack growth or creep rupture for a given stress-temperature condition.[101] The former case takes place at high stresses within a short period of time and generally involves the extension of a single dominant preexistent flaw from initial size to final critical size. Localized creep damage in the vicinity of crack tip might occur in the slow crack growth regime under certain conditions. Alternatively, at low stresses, failure is generated by bulk deformation such as nucleation, growth, and coalescence of extensive cavities and microcracks as a result of creep processes such as diffusion or viscous flow. The existence of these two failure mechanisms at a certain high temperature under different stress levels has been demonstrated in ceramics with a glassy grain-boundary phase such as silicon nitride,[80] as well as in two alumina ceramics in the absence of a glassy phase at the grain boundaries.[82]

6.3.2.1 Slow Crack Growth vs. Creep Rupture

The two failure mechanisms noted above might also occur in the specimens of static fatigue and trapezoid II loading tests in the current study. As indicated in the previous sections, no distributed creep damage could be identified at high stress levels ($\sigma_{\max} > 48.3$ MPa) for these two loading paths. Thus, the mechanism of slow crack growth of a single dominant crack from the most damaging preexistent flaw to the final critical size was responsible for failure of the high loading specimens in these two loading paths.

However, at low stress levels ($\sigma_{\max} \leq 48.3$ MPa), creep process was more operative than it was at high stresses, and failure of the specimens under these two loading paths might become a combination process of slow crack growth and creep process, as few non-failure-induced small cracks were visible in this loading regime. Creep damage

might occur locally rather than globally throughout the gage section of these tensile specimens, as no bulk creep damages were noticed. Evidence of the existence of creep processes such as finger-like perturbation of glassy phase and grain-boundary sliding has been demonstrated in the low loading specimens of both trapezoid II and static loading tests, as previously shown in Figures 32(B), (C) and 40. The creep-related multiple cracks might also emanate from the preexistent flaws and extend at a lower growth rate by coalescence with the creep-induced cavities or inherent pores ahead of the crack tip through a process of diffusion or viscous flow, depending on the local microstructure of the materials, as the glassy phase was not homogeneously distributed. Crack growth therefore appears to be the controlling factor in determining final failure in this load regime although the rate of crack propagation decreases and the creep process is a little more operative. Therefore, the lifetime seems to be limited by the extension of these multiple cracks to the critical size or to link with each other. The observations noted above suggest that the failure mechanism in the low levels of applied stress ($35.5 \leq \sigma_{\max} \leq 48.3$ MPa) for both static and trapezoid II loading cases might be in a transition regime from the domination by slow crack growth of a single prevailing preexistent flaw to that by bulk creep damage entailing extensive nucleation and linkage of cavities and microcracks.

In the regime of maximum applied stress below 35.5 MPa, the failure mechanism for both static and trapezoid II loading cases could not be examined, as neither of the specimens tested at $\sigma_{\max} = 27.6$ MPa failed when the tests were terminated at 700 and 800 hours, respectively, for static loading and trapezoid II loading. However, it could be anticipated that, in this regime, failure might not occur (below the stress threshold for failure), or creep process may be more operative and the preexistent flaws might be blunted by creep damage[80,82] so that the material may become damage tolerant with the existence of extensive cavities and microcracks.

With regard to the failure mechanism for the cyclic loading with a high loading rate and a short duration of maximum stress, such as sine, square ($R = 0.1$ and 0.5), and

trapezoid I loading wave forms in the current study, the SEM and TEM observations in the previous sections suggest that the mechanism of slow crack growth was the controlling factor for the failure in these three loading wave forms at all applied stresses, as no other cracks or bulk creep damages were detected. In this mechanism, a single dominant crack emanates from the most damaging preexistent flaw and likely grows along the grain boundaries and through the inherent pores for the given stress-temperature conditions in these three cyclic loading wave forms.

As noted by the above discussion, failure of the selected alumina appears to be controlled by crack propagation under the given stress-temperature conditions in both static fatigue and various cyclic fatigue tests. In a later section, the bridging effect of the viscous grain-boundary phases under static and cyclic loading conditions will be examined to make a possible explanation of the beneficial effect on the failure time from the cyclic loading with a short duration of maximum stress in comparison to static loading.

6.3.2.2 Comparison with Other Studies

Most of the previous studies[9,10,13,64-66] on cyclic fatigue behavior of ceramics at elevated temperatures only considered lifetime analysis of the mechanical testing results. Very little information is available for the high temperature cyclic fatigue mechanisms in ceramics due to the lack of comprehensive studies in this field.

In a recent investigation on the high temperature failure of an Al_2O_3 -33 vol.% SiC whisker composite under cyclic loads, Han and Suresh[62] found that the permanent damage and fatigue crack growth in this ceramic composite were essentially due to the interfacial and intergranular cavitation and microcracking at the crack tip. The formation of a zone of microcracks and crack bifurcation at the crack tip as well as along the crack wake in this ceramic composite is evidenced by Figure 41[62] of a notched and precracked four-point-bend specimen subjected to cyclic tensile loading at a load ratio, $R = 0.15$ and

frequency, $f = 0.1$ Hz in 1500°C air environment. In the high temperature air environment, the oxidation of SiC whiskers caused the formation of an amorphous glass phase and led to intergranular and interfacial cavitation. The oxidation of the SiC whiskers in the crack-tip damage zones was more extensive in static loading than it was in cyclic loading. However, breakage of the SiC whiskers was observed only in cyclic loading. The size of the crack-tip microcracking zone was also found to increase extensively with the increase in the applied stress levels or the test temperature and with the decrease in loading rate. In addition, the level of the bridging of the crack surfaces was also different between static and cyclic loading. This might partially explain the slower crack growth under cyclic loads compared to static loads with a similar maximum stress intensity factor.[62]

As noted in the previous sections, such features of a damage zone of microcracks and cavities around the crack tip were never detected in the monolithic alumina studied in the current program at both static and various cyclic loading conditions. It is noted that in the work of Han and Suresh,[62] small flexure specimens with an initial long crack, 3.5 mm in length including the length of notch and precrack, were used in the four-point bending tests under static and cyclic loads.

In the recent work of Wilkinson and co-workers[81,82], the creep and creep fracture behavior of two hot-pressed aluminas, made by AVCO and ARCO, were studied under static loads. Both aluminas were free of any grain-boundary glass phase and had very low residual porosity $<0.05\%$. Both were also composed of equiaxed grains with an average grain size of $1.6\text{ }\mu\text{m}$ for AVCO and $1.0\text{ }\mu\text{m}$ for ARCO. Creep tests in air were conducted on AVCO alumina at 1150°C using four-point bending method. However, both uniaxial tensile and four-point-bend tests were performed on ARCO alumina at 1250°C in air. The gauge section of the tensile specimen had a rectangular cross-section of $3.0\text{ mm} \times 5.0\text{ mm}$ with a length of 12.5 mm . The observations in the work of Wilkinson et al.[82]

are briefly summarized in the following paragraph for comparison with the cases of trapezoid II and static loading in the current study.

Three failure regimes were identified for both AVCO and ARCO aluminas depending on the stress levels. At high stresses (above about 175 MPa steady-state stress), in flexure, fracture occurred by slow crack growth of a single dominant crack from the most damaging preexistent flaw. This was called the "slow crack growth regime". Below a threshold stress (about 170/180 MPa), in the "microcrack regime", both materials failed by the development and coalescence of multiple microcracks (of the order of 100 μm) at the regions of large grains and chemical inhomogeneities. The density and morphology of the microcracks and cavities in this intermediate stress regime were contingent on the test geometry and the material. In flexure, much more microcracks appeared on the tensile surfaces of the AVCO specimens than on those of ARCO specimens. In addition, the higher density of microcracks in the flexural specimens of AVCO alumina also induced the development of "shear bands" (Figure 42[82]) which were never observed in the uniaxial tensile specimens. These microcracks blunted or bifurcated after some extension. Similar observation of "shear bands" on flexural specimens of other alumina was also reported by Dalglish et al.[75] In ARCO alumina, more extensive microcracks and cavities were observed in tensile than in flexural specimens due to the uniform stress distribution (Figure 43[82]). In contrast to the case in bending specimens, microcracks in tensile specimens in this regime remained sharp as they extended. At lower stresses (observed only in the tensile specimens of ARCO for stresses of 55 MPa and below), a large number of cavities and very few microcracks were observed in this "damage-tolerant regime". The cavities grew by a combination of surface diffusion and grain-boundary sliding and coalesced to form microcracks at the areas of large grains. In this regime, the coalescence of cavities near the crack-tip led to crack branching and blunting in the tensile specimens as shown in Figure 44[82]; i.e., crack growth was accompanied by damage zones at the crack tip. Although the isolated cavities could extend rapidly by surface diffusion to the limiting size

of a grain facet at low and intermediate stresses, the final failure was still dominated by crack growth.[82]

The overall observation in the work of Wilkinson et al.[82] parallels that in the trapezoid II and static loading in the present study. At high stresses, failure occurred by the slow growth of a single crack, while creep process was more active at intermediate and low stresses. However, only few small cracks near the outer surfaces were observed at the low stresses ($\sigma_{\max} \leq 48.3$ MPa) in the current work and they appeared sharp at the crack tip without blunting or bifurcation. The differences in the density and morphology of the microcracks (of the order of 100 μm) in tensile specimens between the current study and the work of Wilkinson et al.[82] might be related to the extent and variety of creep damage which is a function of material's composition and microstructure, stress, loading rate, temperature, and test geometry. For example, Robertson et al.[81] also discovered that no fracture occurred and no microcracking was detected in the flexural specimens of AVCO alumina at 1350°C in the stress range between 12 and 39 MPa. It is noted that the residual porosity in the alumina selected in the present work is about 1.5%. Further research is necessary to find out what kind of role these inherent pores would play in the development of creep damage such as nucleation, growth, and coalescence of cavities and microcracks in ceramic materials.

Comparison of the observed damages in the bending specimens between the work of Wilkinson et al.[82] and Han and Suresh[62] indicates that the extent of crack bifurcation at the crack tip might be related to the crack length. There is more crack branching in the long crack (a few millimeters in Han and Suresh[62]) than that in the small cracks (about 100 μm in Wilkinson et al.[82]) as shown in Figures 41 and 42. The tolerant damage size is also different between the long-cracked and small-cracked specimens. For instance, the crack-tip damage zones are composed of microcracks (of the orders of 10 and 100 μm) and cavities for the long cracks,[62] and only comprised of cavities (grain size) for the small cracks.[82] The formation of "shear bands" in bending specimens could

generate an effective load shedding mechanism which would not occur in tensile specimens, and extend the failure time.[82] This, in addition to the size effect, promotes another question about the validity of bending tests for lifetime assessment in ceramic materials.

6.3.2.3 Bridging Effect of the Viscous Glassy Phases

In several previous studies,[68,69,71,78] creep crack propagation in ceramics at elevated temperatures is usually thought to occur by coalescing with cavities in the damage zone ahead of a crack tip. In those studies, the activity behind the crack tip was not considered in modelling the creep crack growth; i.e., the crack surfaces were assumed to be traction-free. However, for ceramics with a glassy phase in the grain boundaries, the adhesive forces caused by the viscous second phase behind the crack tip also need to be considered in developing the crack growth model, especially for the case that high temperature failure is dominated by crack propagation. Crack bridging by the viscous glassy phase is one of the behind-crack-tip events that shield the crack tip from the externally applied stress by reducing the stress intensity factor at the crack tip. This bridging effect of the viscous glassy phase was also considered as the primary contributor to the increasing crack resistance curve behavior in an alumina at high temperatures.[94] Evidence of the viscous glassy phase bridging the crack surfaces has been shown in the previous sections (Figures 36 and 40). In the following discussion, we will consider this bridging effect under static loading and various cyclic loading wave forms.

In a recent study reported by Thouless,[103] the treatment of coplanar damage at a crack tip as a damage zone or as a bridging zone was carefully discussed. Either approach, a damage zone or a bridging zone, would essentially generate similar results for crack growth rate. For the case of bridging by a single viscous ligament behind the crack tip of

an elastic matrix in plane stress conditions, the effective stress intensity factor, K , at the crack tip can be derived as a function of time by [103]

$$K = K_{\infty} [1 - \exp(-\pi E_m t / 8 \eta_l)] \quad (11)$$

where K_{∞} is the applied stress intensity factor (assumed to be constant), E_m is Young's modulus of the matrix, t is the time from when the ligament begins to grow, and η_l is the viscosity of the ligament with a value of three times the conventional (shear) viscosity. A characteristic time, t_c , for the rate-sensitivity of deformation of the viscous ligament can be defined as $t_c = 8\eta_l/\pi E_m$.

Microscopic examination of the alumina grains by TEM after failure gave little evidence of dislocation activity within the grains, and only small localized creep damage was detected in the low stress regime for static loading and trapezoid II loading tests. Consequently, we may assume that an elastic stress field dominates around the tip of a growing crack for all of the given stress-temperature conditions in the present work. Thus, the stress intensity factor can be assumed to characterize the crack growth rate. Because of the existence of isolated zones of glassy phase in this selected alumina, the formation of a bridging zone comprising viscous glassy islands behind the crack tip is anticipated and supported by the microstructural analysis of the failed specimens noted earlier. According to the author's knowledge, there is no existence of such model which can generate quantitative prediction of cyclic crack growth rate in ceramics under various loading wave forms with the consideration of the effects of crack bridging by the viscous glassy phase and the size and shape of the bridging zone. Thus, we will extend the derivation in acquisition of Eqn. (11) to various cyclic loading wave forms, and use the obtained results in Eqn. (11) as the case of static loading to examine the general trends of the influence of the bridging effect on high temperature static and cyclic fatigue behavior of ceramics with viscous glassy phases. The details of this simplified model, the procedures of extending

this model to the various cyclic wave forms employed in the present work, and the calculation methods are given in the Appendix.

As the true viscosity of the glassy phase in the selected alumina is not available, a particular value of 1.25 second for t_c is selected in order to obtain trends consistent with the stress-life data. With $t_c = 1.25$ s and $E_m \approx 260$ GPa (estimated for this alumina at 1200°C), the viscosity is then given approximately as $\eta_l/3 \approx 4 \times 10^{11}$ P which is comparable to the available values of most silica glasses at this temperature range.[104] Comparison of $t_c = 1.25$ s with the loading parameters shown in Figure 4 indicates that the loading time in a cycle for the applied sine, square, and trapezoid I wave forms is $0.2 t_c$, while the corresponding value for the applied trapezoid II wave form is $2 t_c$. These cyclic wave forms are then applied into the governing equations in Thouless's model[103] with the consideration of K_∞ as a periodic function of time. Results of the calculated effective stress intensity factor at the crack tip under the applied cyclic loading wave forms compared to those in static loading with the same maximum applied stress intensity factor, K_{max} , are plotted versus time in Figures 45 and 46.

As shown in Figure 45 of the comparison between static loading and various cyclic loading wave forms with $R = 0.1$, it is apparent that the bridging effect of the glassy phase behind the crack tip is frequency or cycle shape dependent. For a symmetrical wave form with a short period compared to the characteristic time, t_c , such as the applied sine and square wave forms, the reduction of the stress intensity factor range at the crack tip is truly enhanced (reduced from $\Delta K = 0.9$ to $0.1 K_{max}$ in the current example) even though the mean stress intensity factor ($0.55 K_{max}$) at the steady state ($t > 4 t_c$ in Figure 45) is identical to the applied mean stress intensity factor. The effective stress intensity factors of the sine and square ($R = 0.1$) wave forms are not significantly different, and both are much smaller than those in trapezoid I, trapezoid II, and static loading. This is consistent with the stress-life data that the lifetime in the applied sine and square ($R = 0.1$) wave forms is comparable and larger than that in the other three loading cases. In the case of the trapezoid wave with

a limited time of unloading and a short hold time at maximum stress (such as the applied trapezoid I wave form), the stress intensity factor range at crack tip is profoundly reduced, but the mean stress intensity factor is much higher than that in either sine or square ($R = 0.1$) wave form. However, the effective stress intensity factor at the crack tip in trapezoid I is still lower than those in trapezoid II and static loading. This agrees with the stress-life data that the lifetime of trapezoid I loading is less than (by a factor of 2 in cycles or by a factor of 4 in time) that in sine or square ($R = 0.1$) wave form, and suggests that the length of unloading time in a fatigue cycle would also affect the bridging effect and the lifetime. The specimens under trapezoid I loading were also found to take a longer time to fail than did trapezoid II and static loading specimens at similar maximum applied loads. If the hold time in the trapezoid wave increases to the order of the characteristic time (e.g., $2 t_c$) with the time for unloading in a cycle kept unchanged, the effective stress intensity factor at the crack tip is increased to the level equivalent to that in static loading, as shown by the curve of trapezoid II which almost overlaps the static loading curve in Figure 45. This is consistent with the stress-life data that the lifetime of trapezoid II wave and static loading is comparable to each other, and much less than that in sine, square ($R = 0.1$), and trapezoid I wave forms.

The effect of the externally applied stress ratio, R , on this bridging mechanism is also examined by comparing the calculated crack-tip effective stress intensity factor in static loading to those under the applied square wave forms with two distinct R values, $R = 0.1$ and 0.5 , as shown in Figure 46. With the same cyclic frequency and maximum applied stress intensity factor, the calculated effective stress intensity factor at the crack tip for the square wave with a high applied stress ratio ($R = 0.5$) is larger than that with a low R value ($R = 0.1$), but it is still much lower than that in static loading. This is also in agreement with the lifetime results, as the specimens under square loading wave form with $R = 0.5$ took a shorter time to failure (approximately by a factor of 2 in both cycles and time) than those under square loading wave form with $R = 0.1$. It is noted that the stress-life data also

indicated square wave form with $R = 0.5$ would generate longer lifetime than did static loading with the same maximum applied stress. Moreover, the calculated effective crack-tip stress intensity factors for square wave form with $R = 0.5$ are still lower than the calculated results for trapezoid I wave form ($R = 0.1$) in Figure 45. This is consistent with the lifetime data that the failure time in trapezoid I loading wave form is slightly less than that in square wave form with $R = 0.5$.

Although only a single viscous ligament behind the crack tip in plane stress is considered in this simplified model, it still demonstrates the general trends. These include: (1) static loading would generate the largest effective stress intensity factor at the crack tip compared to various cyclic loading wave forms; (2) the effective crack-tip stress intensity factor in cyclic loading is frequency or cycle shape dependent; (3) the cyclic loading results would get closer to the static loading results when the hold time at the maximum stress is increased to the order of the characteristic time, t_c , for the trapezoid wave forms; (4) the effective stress intensity factor at the crack tip increases with the externally applied stress ratio. As noted above, these general trends are in agreement with those in the stress-life data, and support the postulation that crack propagation might be the dominant controller in the failure time and the viscous glassy phases might play an important role in the improved fatigue resistance for the cyclic loading with a short duration of maximum stress at high temperatures.

The current study has identified the possible high temperature failure mechanisms in both static and various cyclic loading for an alumina with a small amount of glassy phase under the given stress-temperature conditions. These observed mechanisms in combination of a simplified model of crack bridging by a viscous ligament behind the crack tip can make a reasonable qualitative explanation of the stress-life data. However, a more rigorously quantitative lifetime prediction or crack growth rate modelling for ceramic materials at elevated temperatures under various cyclic loading paths will require further consideration of the effects of size and shape of the bridging (or damage) zone, amount of viscous

ligaments, other mechanisms behind the crack tip, geometry of the crack front, and existence of processing pores and other microstructural factors. In addition, whether the high temperature cyclic crack growth rate in ceramics is controlled by the power law in terms of stress intensity factor range or maximum stress intensity factor at the crack tip, or by other forms needs more work with mechanistic and microstructural analysis.

7. CONCLUSIONS

(1) Fatigue behavior of a polycrystalline alumina was studied at room temperature and 1200°C in both static and cyclic loading. Cyclic fatigue effects at both temperatures could not be explained only by accumulation of the static fatigue damage through an integration over the cyclic loading history. Cyclic loading at room temperature was found to degrade more strength than static loading at the same maximum applied load. In contrast, it was not more detrimental than static loading at high temperatures

(2) Cyclic lifetime was cycle dependent at room temperature. At high temperatures, it became cycle shape or time dependent, and cyclic loading with a short duration of maximum stress took a larger number of cycles to fail than did cyclic loading with a longer hold time at maximum stress.

(3) At high temperatures, cyclic loading with a short duration of maximum stress provided a beneficial effect on fatigue lifetime in comparison to static loading at the same maximum stress, while lifetime of the cyclic case with a longer hold time at maximum stress was very close to the static loading lifetime under a similar maximum applied load.

(4) Cyclic fatigue mechanisms at both room and high temperatures might be attributed to the events behind the crack tip. The deleterious cyclic loading effect at room temperature was likely associated with the behind-crack-tip activities such as interlocking grains, frictional interlocking of asperities, and trapped grains between the crack surfaces. The beneficial cyclic loading effect (compared to static loading) at high temperatures may be due to the rate-sensitivity of deformation of the viscous glassy phases bridging the crack surfaces behind the crack tip.

(5) Slow crack growth of a single dominant crack from the most damaging preexistent flaw was the major failure mechanism for all room temperature static and cyclic fatigue specimens as well as for the high temperature specimens under cyclic loading with a short duration of maximum stress at the given stress-temperature conditions.

(6) At high levels of applied load, fracture of the high temperature specimens under trapezoid II wave form (a longer hold time at maximum stress) and static loading also occurred by the formation and growth of a single dominant crack. However, at low applied stresses, failure in these two loading paths might occur by nucleation, growth and/or coalescence of multiple cracks, and creep process was more operative than it was at other high temperature loading conditions. Preexistent flaws were still the favorable sites for crack nucleation in both loading regimes under these two high temperature loading paths.

(7) Crack bridging by the viscous glassy phases behind the crack tip was detected and a simplified model was used to calculate the effective stress intensity factor at the crack tip taking the bridging effect into account. The qualitative agreement between the calculated trends and the actual high temperature stress-life data indicated that the failure time in all applied static and cyclic loading conditions at high temperatures was likely controlled by crack propagation. The loading paths generating the longest failure time, such as the applied sine and square wave forms, correspond to the lowest levels of the effective crack-tip stress intensity factor, and vice versa for the static loading and trapezoid II wave form.

TABLES

Table 1 Results of cyclic fatigue at room temperature under triangular loading wave form with $R = 0.075$

Maximum Stress, (MPa)	Cycles to Failure		Time to Failure, (Hours)
320.3	1 ^c		N/A
308.9 ^a	1 ^c		N/A
273.9 ^a	1 ^c		N/A
271.2 ^a	42	(0.5 Hz)	0.02
238.8 ^a	9179	(0.5 Hz)	5.10
234.4	4374	(0.1 Hz)	12.15
234.4 ^b	800	(2.0 Hz)	0.11
228.2 ^a	2935	(0.5 Hz)	1.63
220.6	33243	(0.1 Hz)	92.34
220.6	9630	(2.0 Hz)	1.34
220.6	67250	(5.0 Hz)	3.74
207.2 ^a	115418	(2.0 Hz)	16.03
203.7 ^b	72020	(2.0 Hz)	10.00
203.7 ^a	399861	(2.0 Hz)	55.54
203.7	103800	(5.0 Hz)	5.77

^aFrom Liu and Brinkman[38]^bFrom Mayer[59]^cTensile Strength Test

Table 2 Results of static fatigue at room temperature under constant loading

Maximum Stress, (MPa)	Time to Failure, (Hours)
251.7	0.15
243.0	8.10
234.4	50.05
220.6	>351.00
203.7	>358.00

Table 3 Results of cyclic fatigue at 1200°C under sine wave form with $R = 0.1$ and $f = 2$ Hz

Maximum Stress, (MPa)	Cycles to Failure	Time to Failure, (Hours)
206.0	1 ^a	N/A
103.4	1970	0.27
86.2	8170	1.14
75.8	6410	0.89
62.0	174420	24.22
55.2	>1000000	>138.89

^aTensile Strength Test

Table 4 Results of cyclic fatigue at 1200°C under square wave form with $R = 0.1$ and $f = 2$ Hz

Maximum Stress, (MPa)	Cycles to Failure	Time to Failure, (Hours)
103.4	690	0.10
86.2	6820	0.95
77.6	4040	0.56
69.0	133170	18.50
58.6	505950	70.27
48.3	>1000000	>138.89

Table 5 Results of cyclic fatigue at 1200°C under trapezoid I wave form with $R = 0.1$, $t_h = 0.25$ s, and $t_u = 0.02$ s

Maximum Stress, (MPa)	Cycles to Failure	Time to Failure, (Hours)
86.2	2760	0.21
77.6	2820	0.21
69.0	52600	3.94
48.3	411010	30.83
41.4	799430	59.96
34.5	>1000000	>75.00

Table 6 Results of cyclic fatigue at 1200°C under trapezoid II wave form with $R = 0.1$, $t_h = 2.5$ s, and $t_u = 0.02$ s

Maximum Stress, (MPa)	Cycles to Failure	Time to Failure, (Hours)
69.0	336	0.24
58.6	635	0.44
48.3	40970	28.68
41.4	10860	7.60
41.4	57680	40.38
34.5	130220	91.15
27.6	>1146600	>802.62

Table 7 Results of cyclic fatigue at 1200°C under square wave form with $R = 0.5$ and $f = 2$ Hz

Maximum Stress, (MPa)	Cycles to Failure	Time to Failure, (Hours)
86.2	2510	0.35
69.0	71410	9.92
58.6	94380	13.11
48.3	306640	42.59
34.5	>3000000	>416.67

Table 8 Results of static fatigue at 1200°C under constant loading

Maximum Stress, (MPa)	Time to Failure, (Hours)
86.2	0.07
86.2	0.08
55.2	0.09
48.3	2.00
41.4	51.00
34.5	81.60
27.6	>700.00

Table 9 Calculated r factors for various kinds of loading wave forms

Temperature	Wave Form	r	Duration of a Cycle, τ , (sec)
Room	Triangular	79.43	0.2 ~10.0 (0.1 ~5.0 Hz; $R = 0.075$)
1200°C	Sine	4.90	0.50 ($R = 0.1$)
	Square	2.00	0.50 ($R = 0.1$)
	Square	1.99	0.50 ($R = 0.5$)
	Trapezoid I	1.07	0.27 ($t_h = 0.25$, $t_u = 0.02$; $R = 0.1$)
	Trapezoid II	1.01	2.52 ($t_h = 2.50$, $t_u = 0.02$; $R = 0.1$)

FIGURES

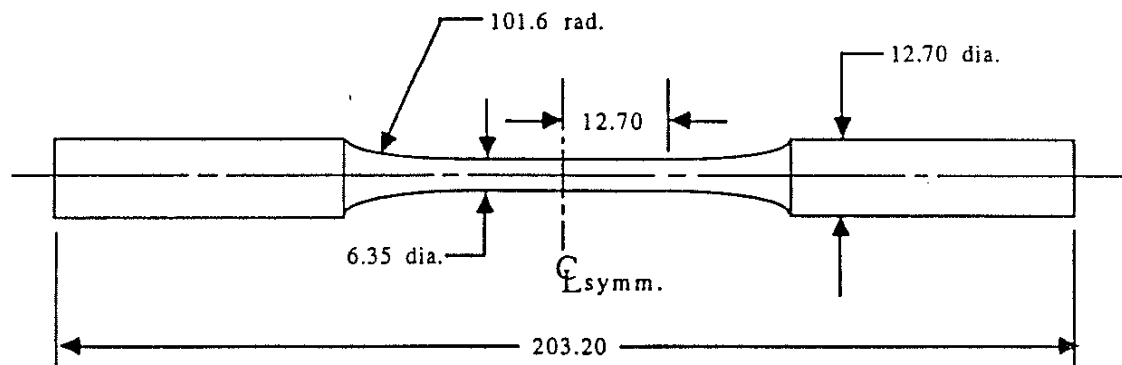


Figure 1 Geometry of tested specimens. (All dimensions in millimeters)

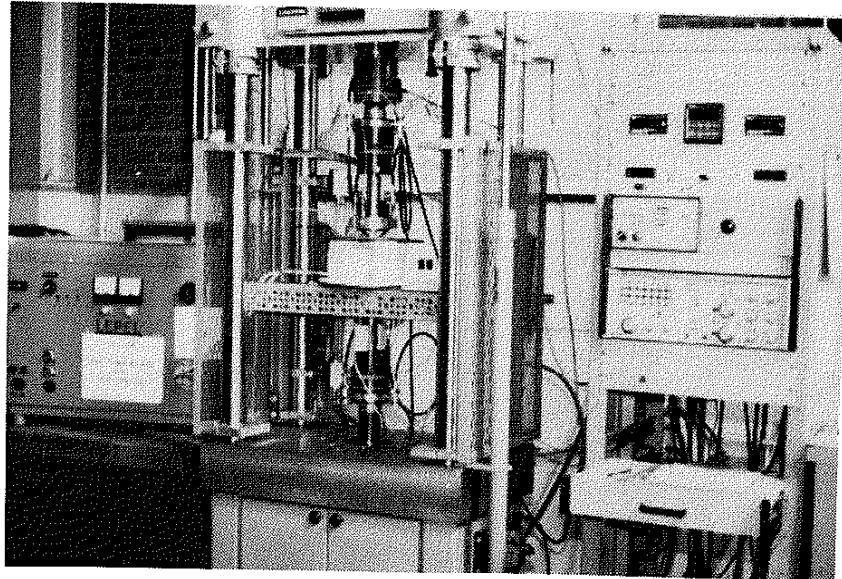


Figure 2 Complete view of test system.

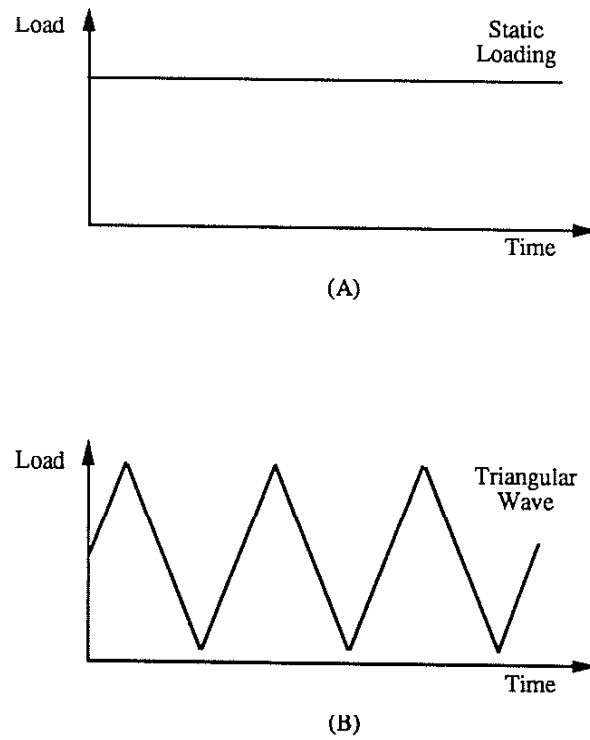


Figure 3 Schematic drawing of loading paths for fatigue tests at room temperature. (A) static loading, (B) triangular wave form (0.1 to 5 Hz, $R = 0.075$).

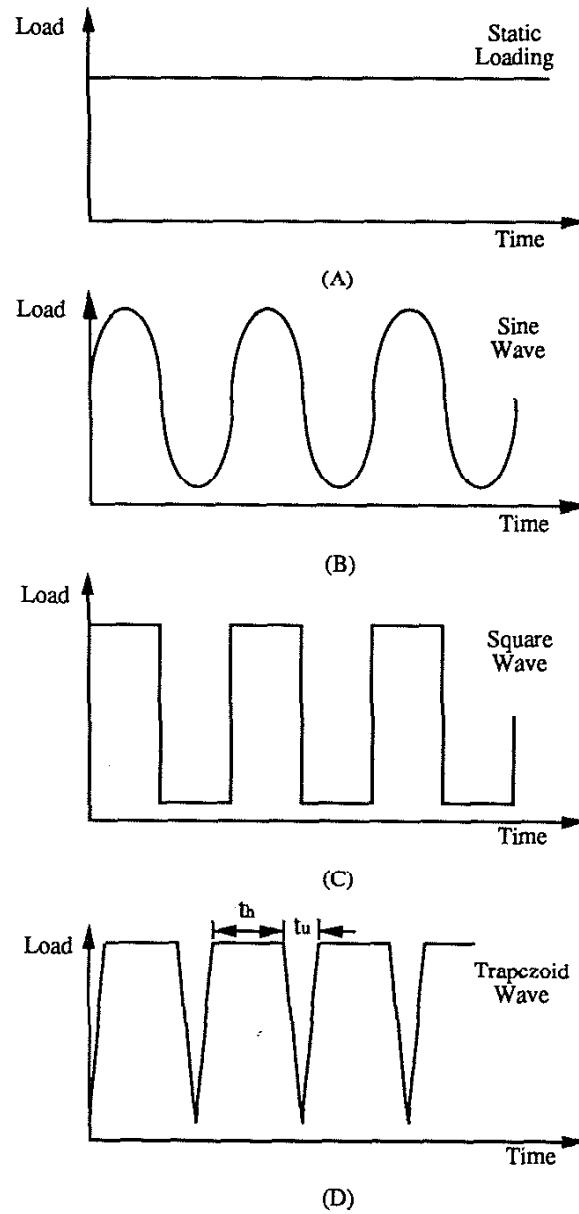


Figure 4 Schematic drawing of loading paths for fatigue tests at 1200°C. (A) static loading, (B) sine wave form (2 Hz, $R = 0.1$), (C) square wave form (2 Hz, $R = 0.1$ and 0.5), and (D) trapezoid wave form (trapezoid I: $t_h = 0.25$ s, trapezoid II: $t_h = 2.50$ s, $t_u = 0.02$ s and $R = 0.1$ for both cases).

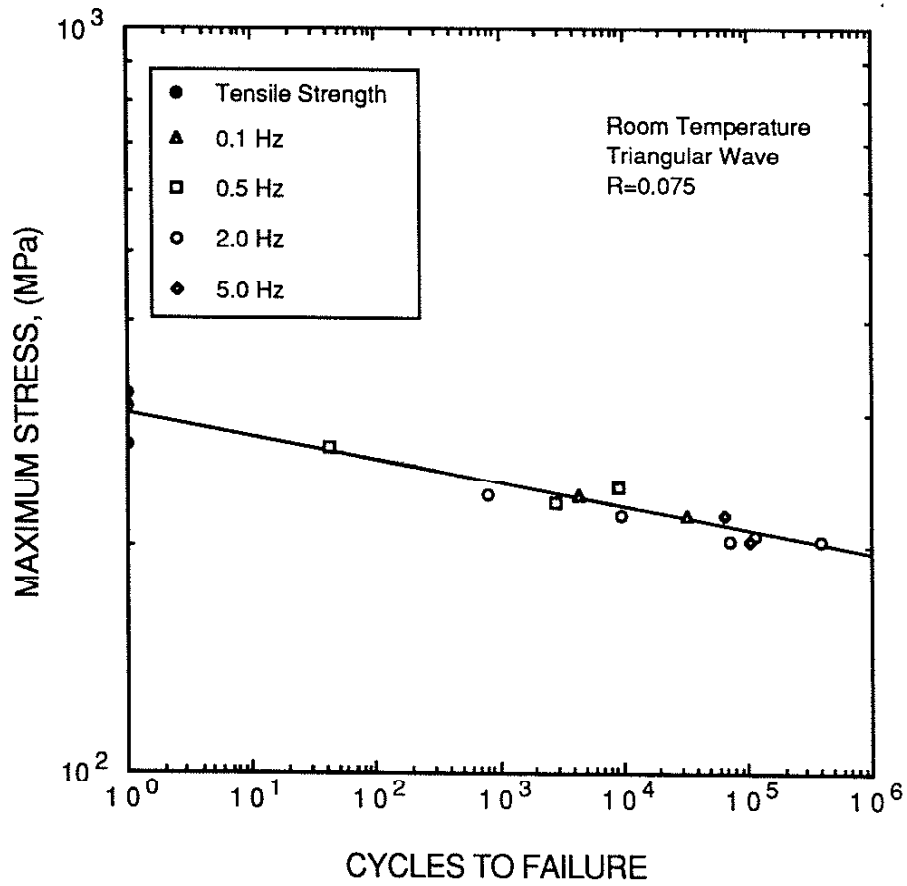


Figure 5 Cyclic fatigue lifetime under different cycle frequencies at room temperature. (Some of the data points of 0.5 and 2 Hz are from Refs. 38 and 59; see Table 1 for details.)

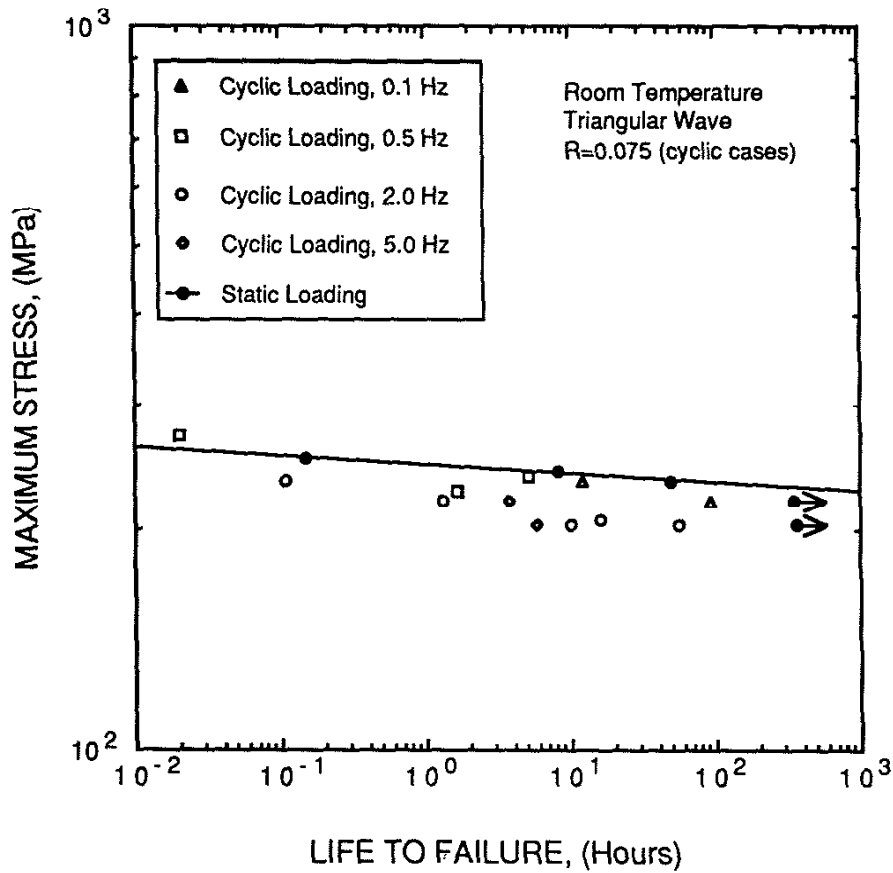


Figure 6 Comparison of static and cyclic fatigue lifetime at room temperature. (Arrow indicates that failure of specimen did not occur when the test was terminated.) (Some of the data points of 0.5 and 2 Hz are from Refs. 38 and 59; see Table 1 for details.)

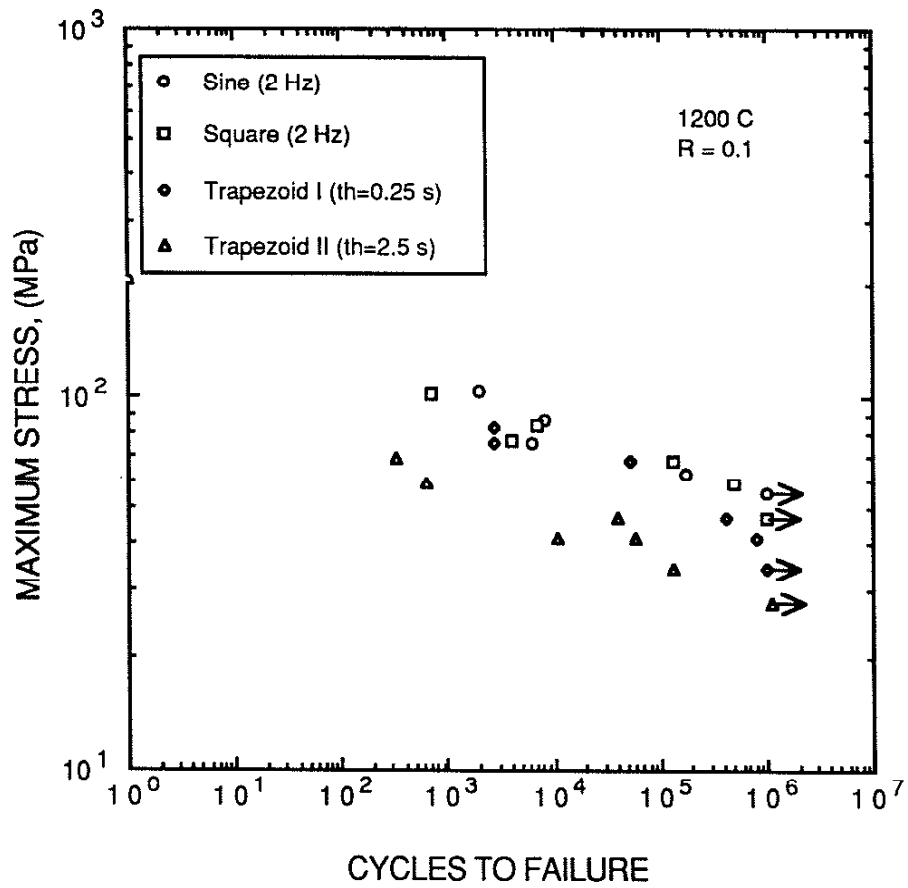


Figure 7 Comparison of cyclic fatigue lifetime at 1200°C under various kinds of loading wave forms with R = 0.1.

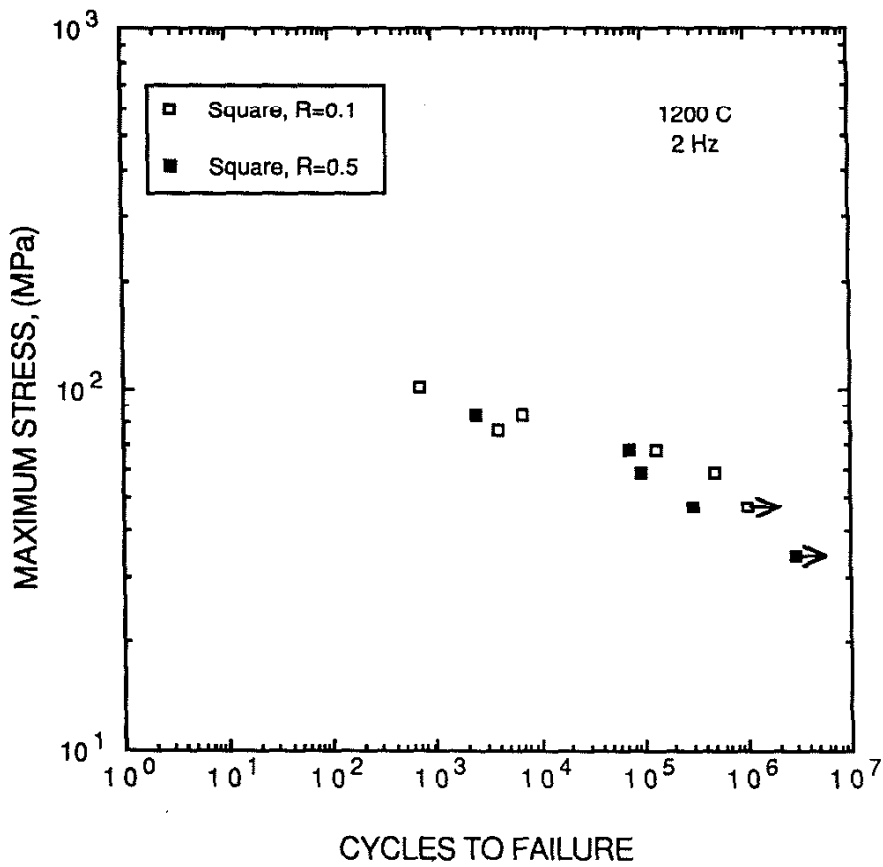


Figure 8 Comparison of cyclic fatigue lifetime at 1200°C under square wave form with R = 0.1 and 0.5.

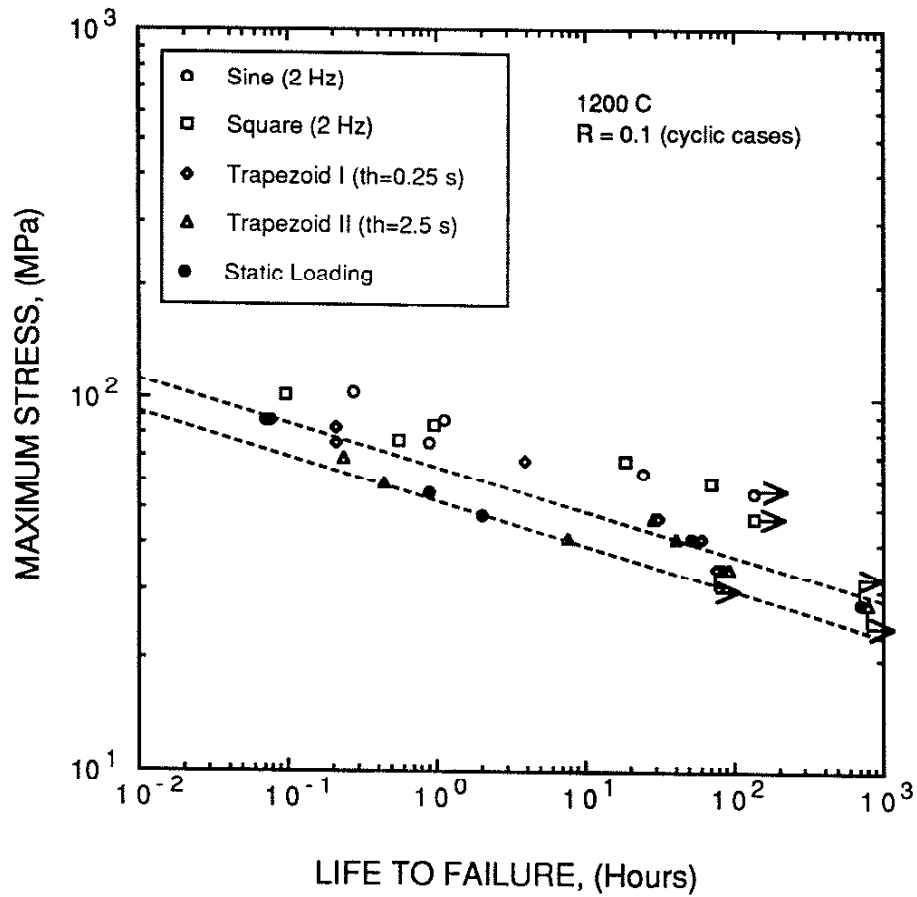


Figure 9 Comparison of static and all cyclic fatigue lifetime with $R = 0.1$ at 1200°C . (The dashed lines are the upper and lower bound of static fatigue data.)

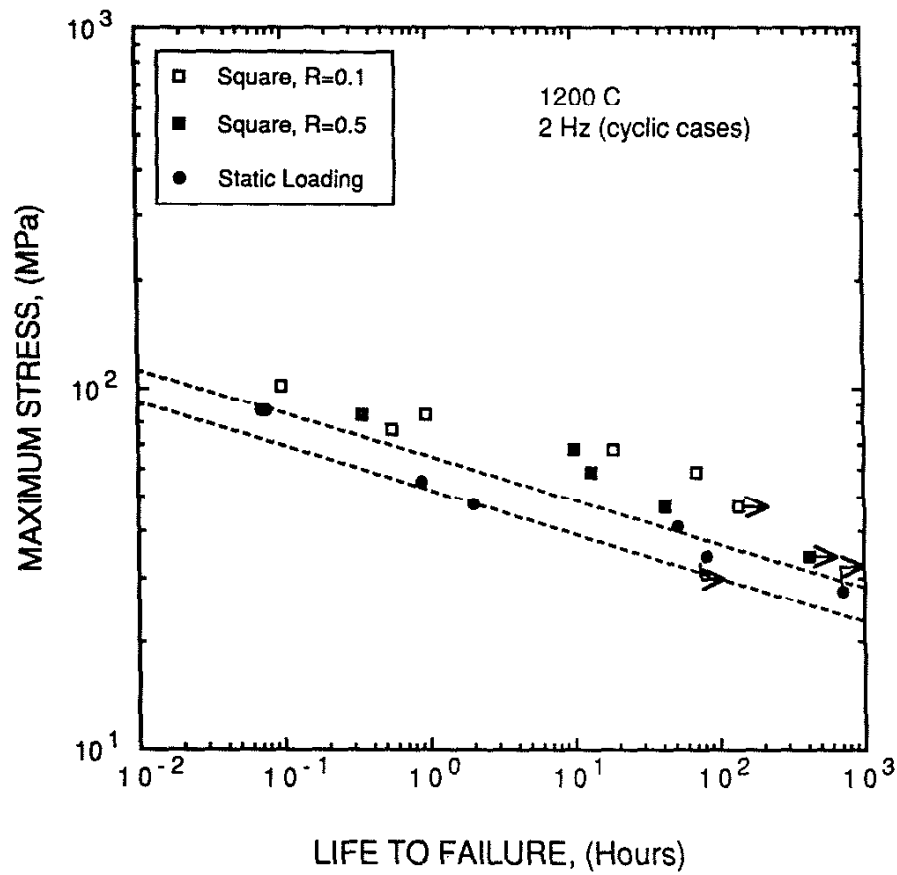


Figure 10 Comparison of static and cyclic fatigue lifetime under square wave form with $R = 0.1$ and 0.5 at 1200°C . (The dashed lines are the upper and lower bound of static fatigue data.)

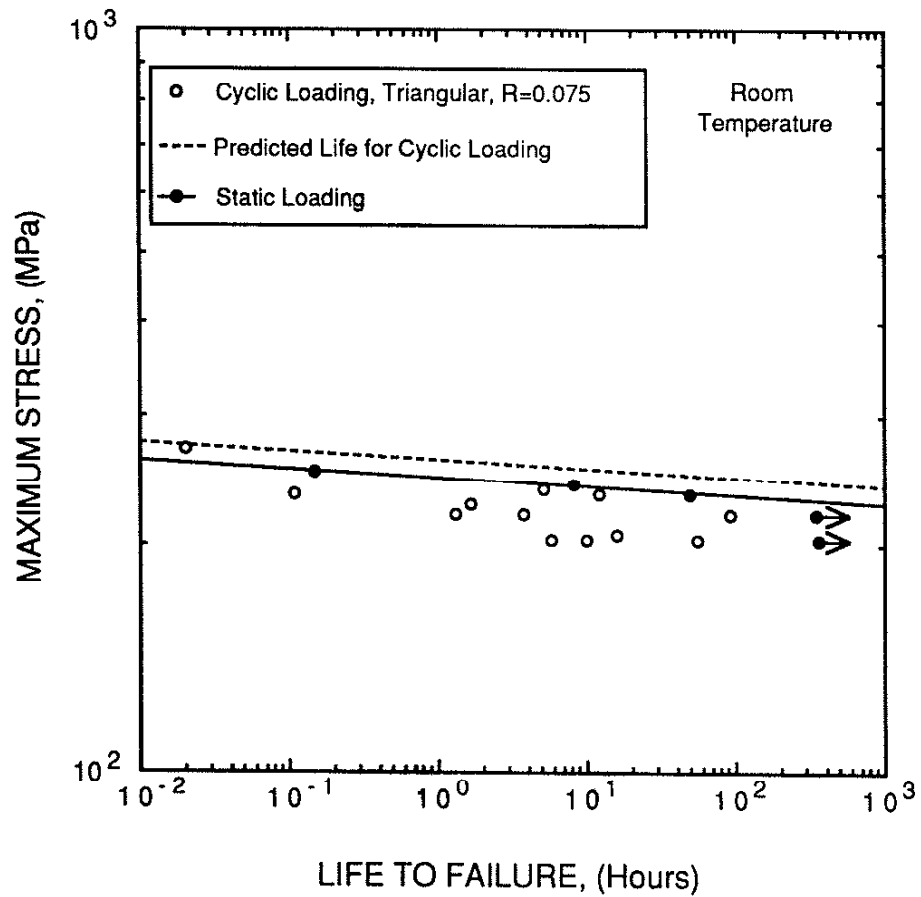


Figure 11 Comparison of measured cyclic lifetime at room temperature with predicted value from static fatigue data. (Some of the data points of 0.5 and 2 Hz are from Refs. 38 and 59; see Table 1 for details.)

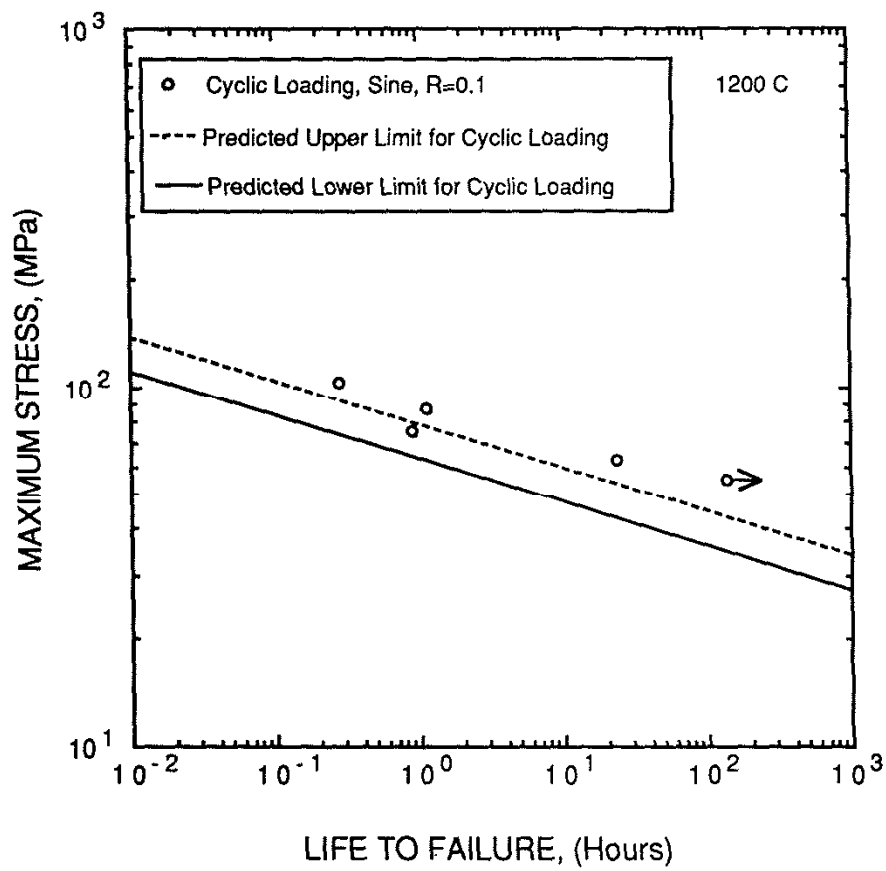


Figure 12 Comparison of measured cyclic lifetime for sine wave form at 1200°C with predicted value from static fatigue data.

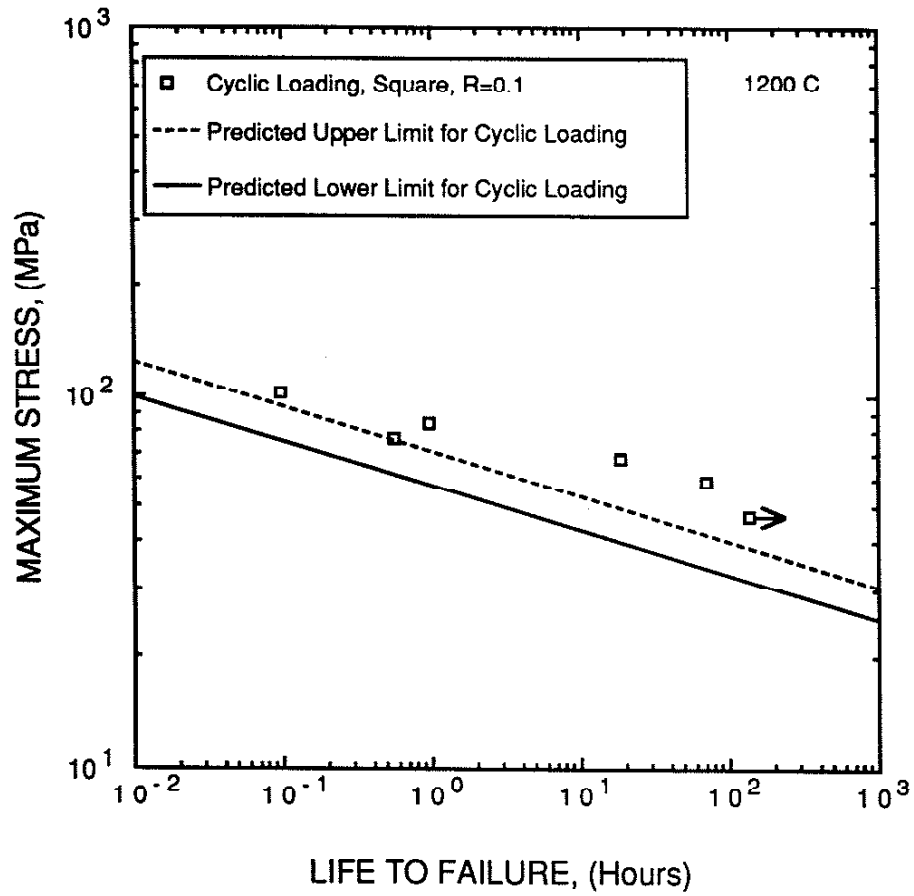


Figure 13 Comparison of measured cyclic lifetime for square wave form ($R = 0.1$) at 1200°C with predicted value from static fatigue data.

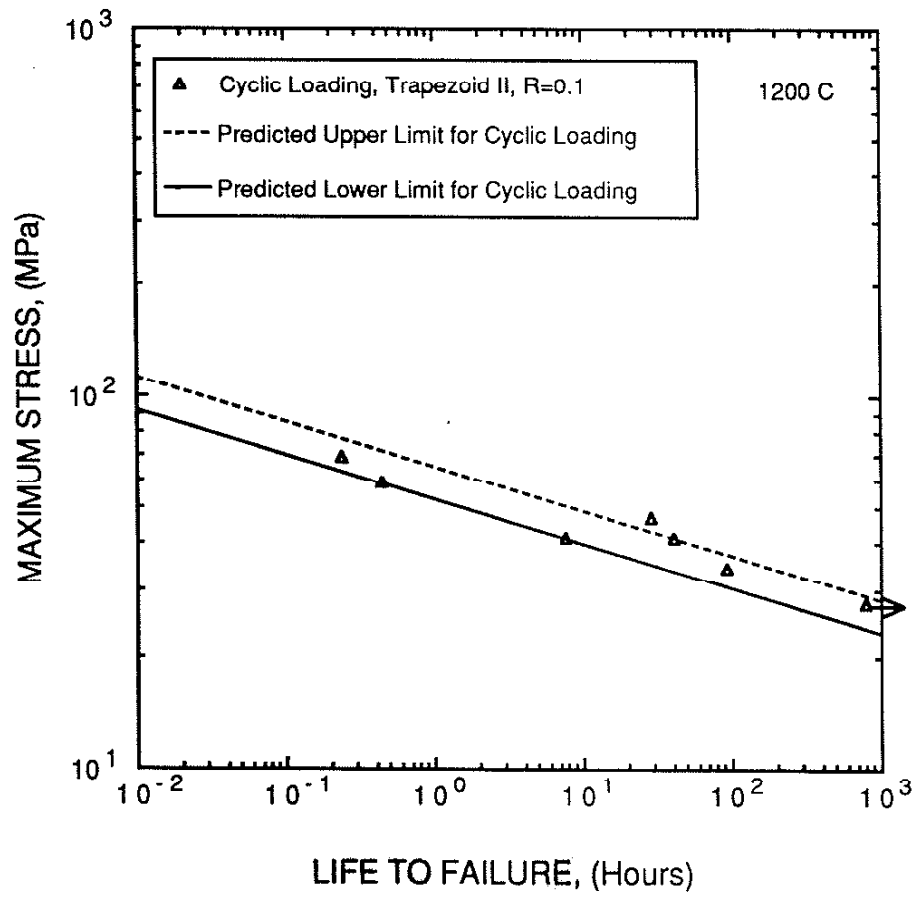


Figure 15 Comparison of measured cyclic lifetime for trapezoid II wave form at 1200°C with predicted value from static fatigue data.

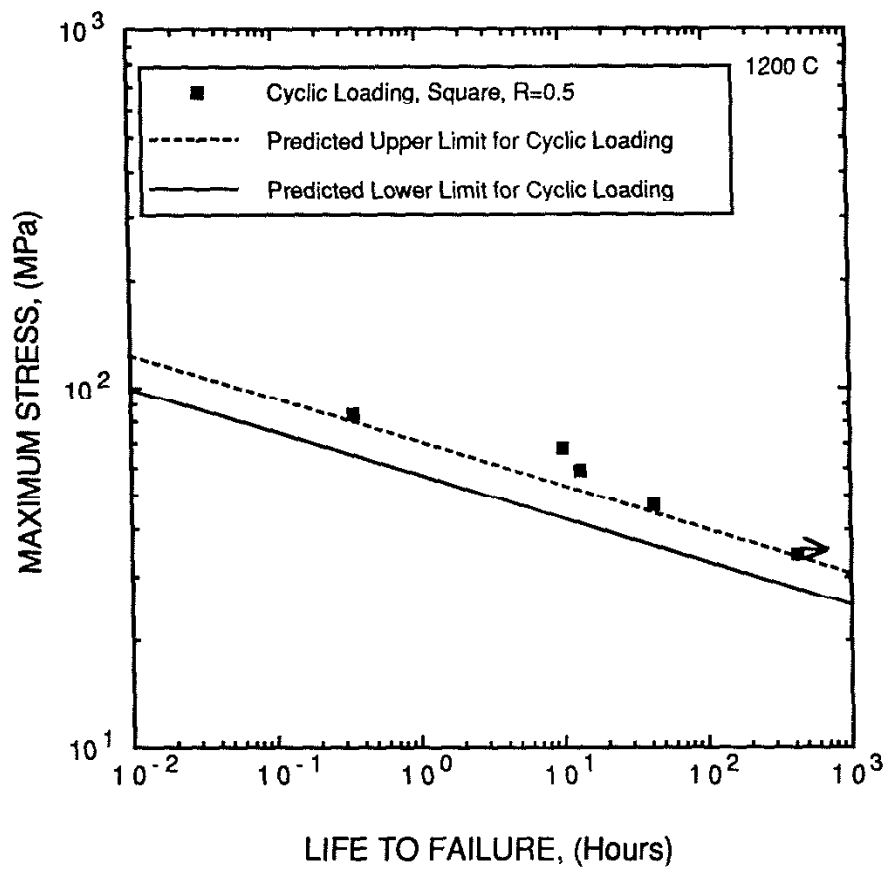
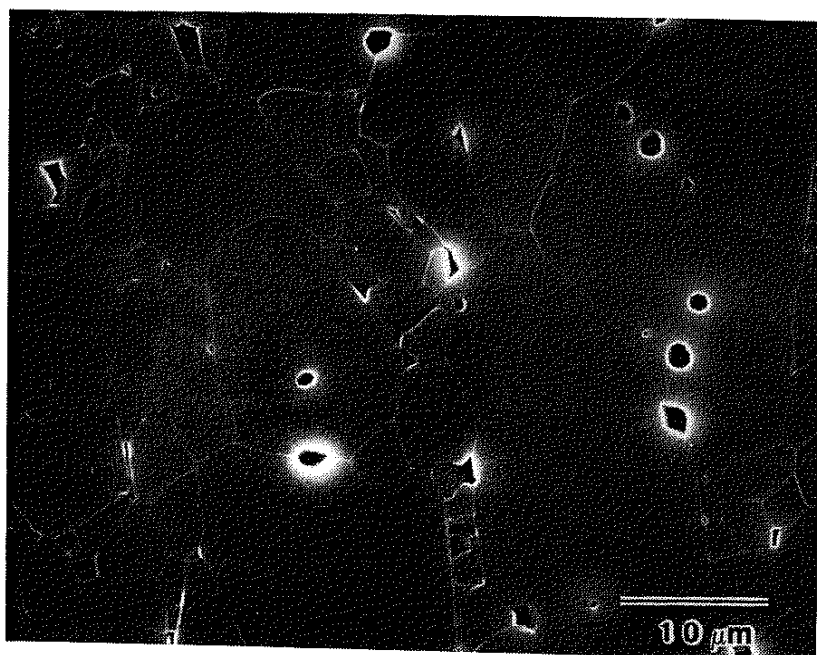
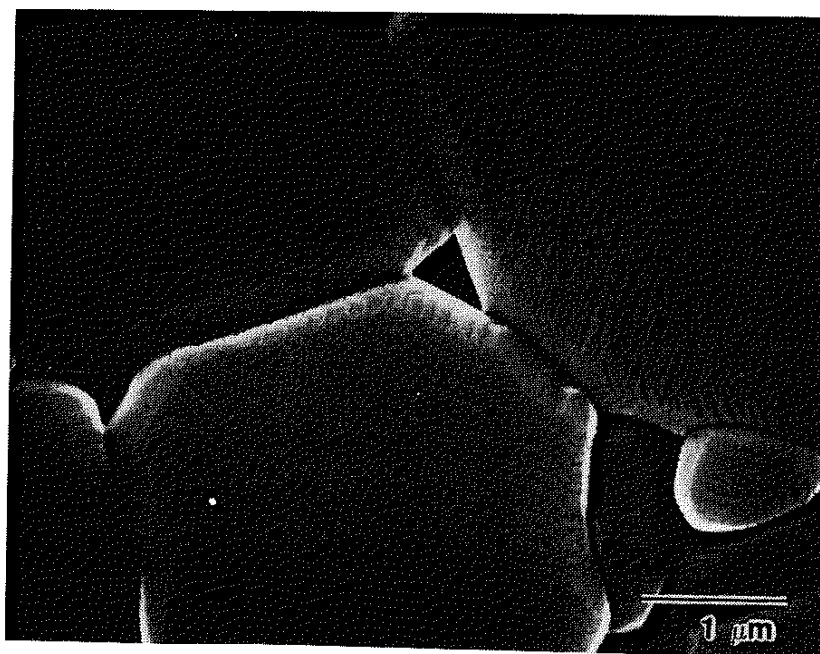


Figure 16 Comparison of measured cyclic lifetime for square wave form ($R = 0.5$) at 1200°C with predicted value from static fatigue data.

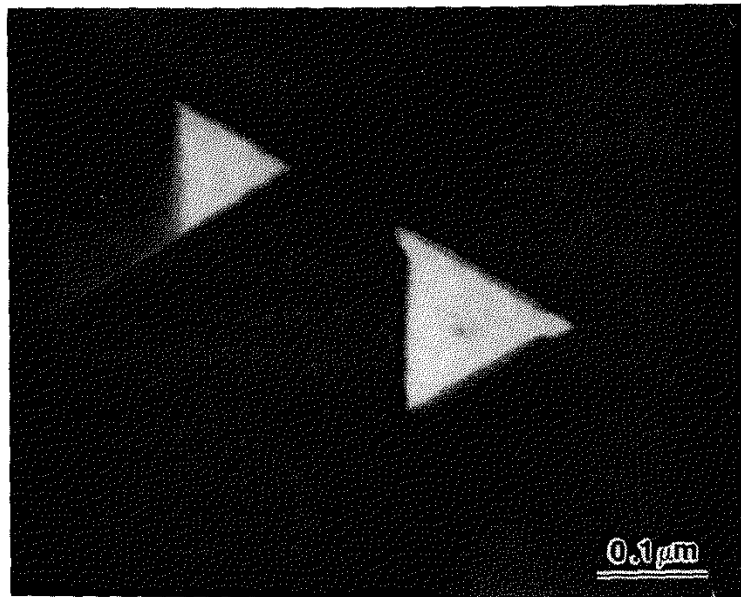


(A)

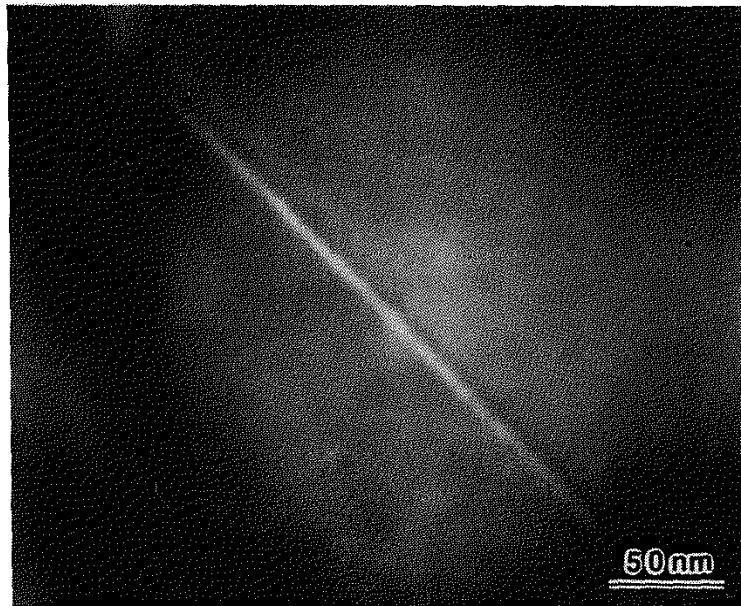


(B)

Figure 17 SEM micrographs of the as-received microstructure for the AD-998 alumina showing the residual porosity. (A) low magnification view and (B) high magnification view.



(A)



(B)

Figure 18 Diffuse dark-field TEM micrographs of the as-received alumina illustrating the isolated zones of glassy phase (A) at triple-point junctions, (B) at a two-grain "channel", and (C) along a two-grain interface and connected triple-point junctions. The glassy phase appears bright in the diffuse dark-field image.



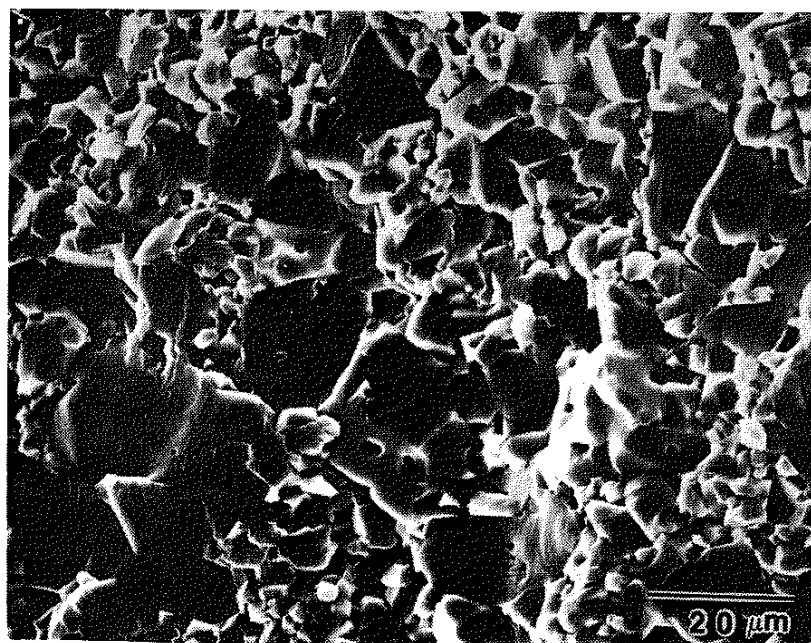
(C)

Figure 18 (Continued)

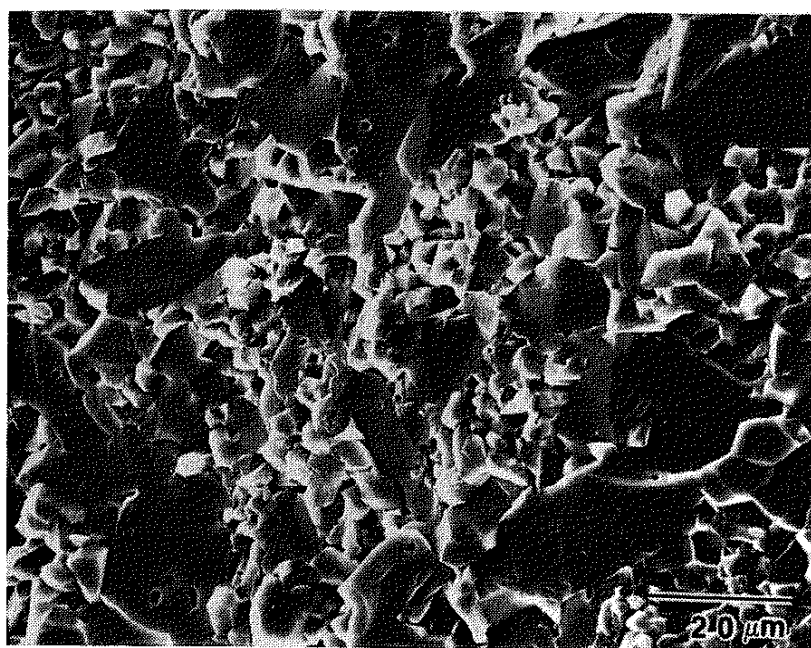


(A)

Figure 19 SEM micrographs demonstrating the typical fracture surface in cyclic fatigue specimens failed at room temperature. (A) macroscopic view, (B) high magnification view in the slow crack growth region, (C) high magnification view in the fast fracture zone. ($\sigma_{\max} = 220.6$ MPa, 2 Hz)

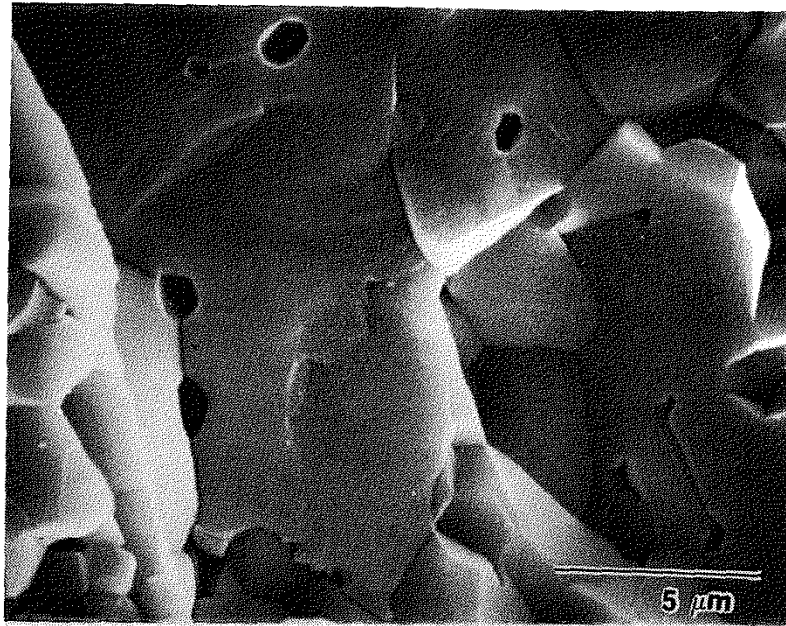


(B)

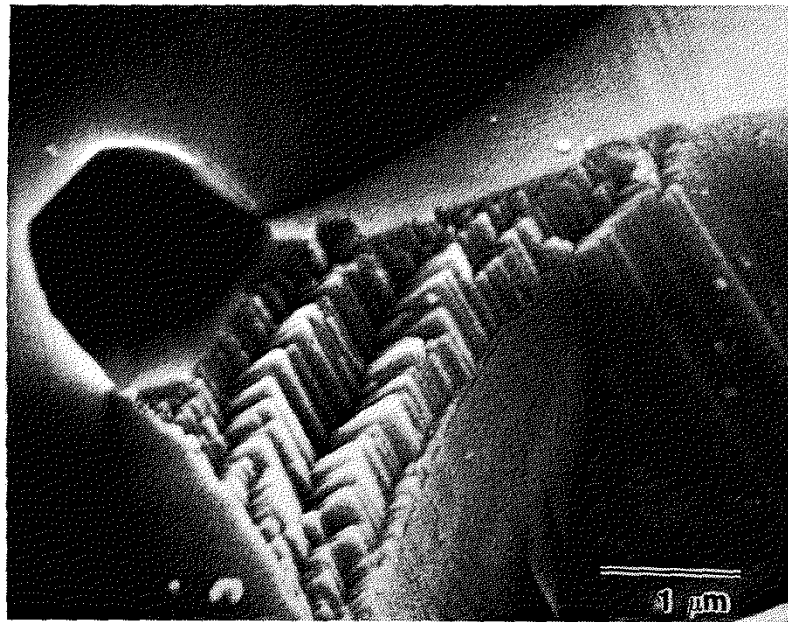


(C)

Figure 19 (Continued)

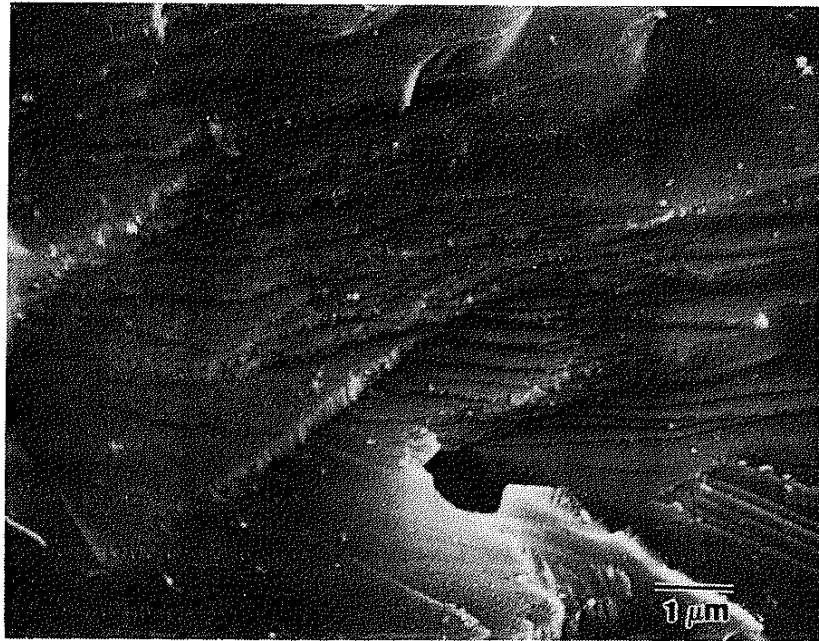


(A)

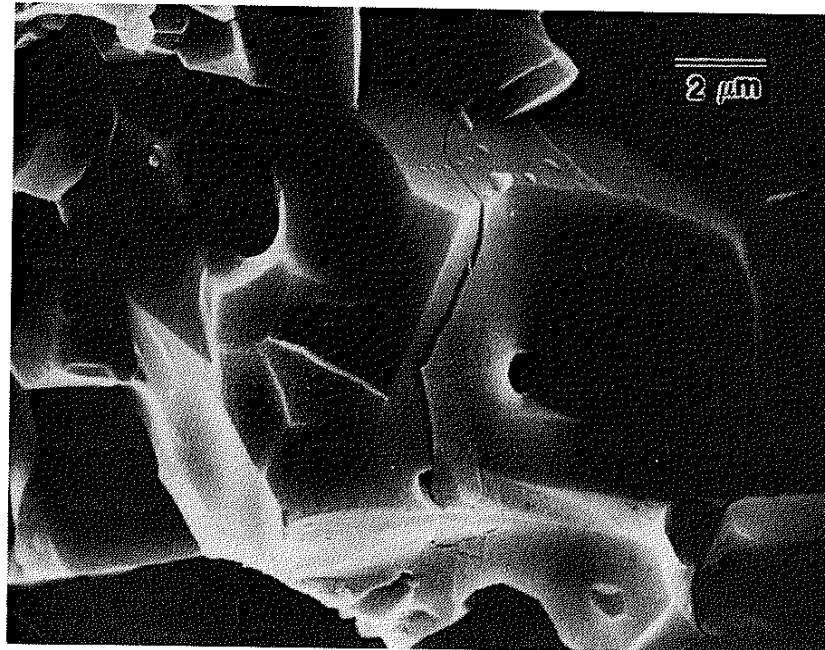


(B)

Figure 20 SEM micrographs of some typical features of transgranular failure mode observed in the fracture surface of room temperature specimens. (A) general view, (B and C) higher magnification view of the cleavage facets associated with the grain-boundary pores or within-grain pores, and (D) a transverse crack through the grain facet.

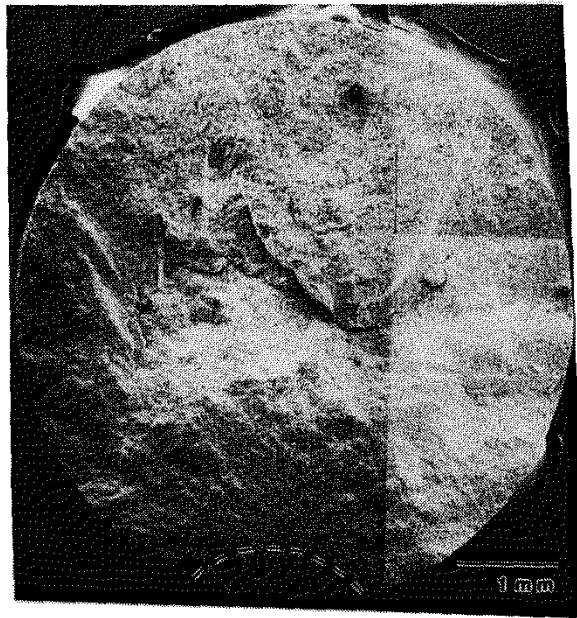


(C)



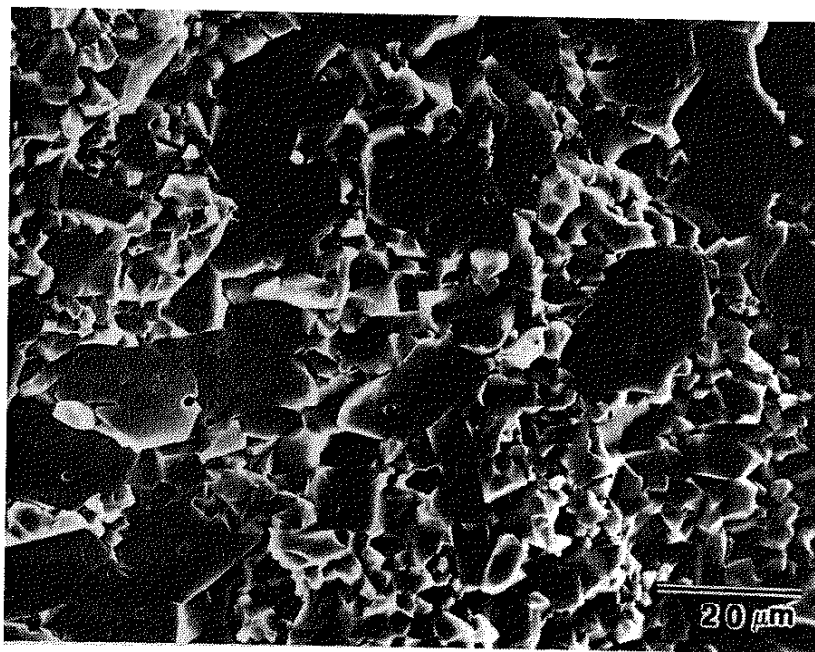
(D)

Figure 20 (Continued)

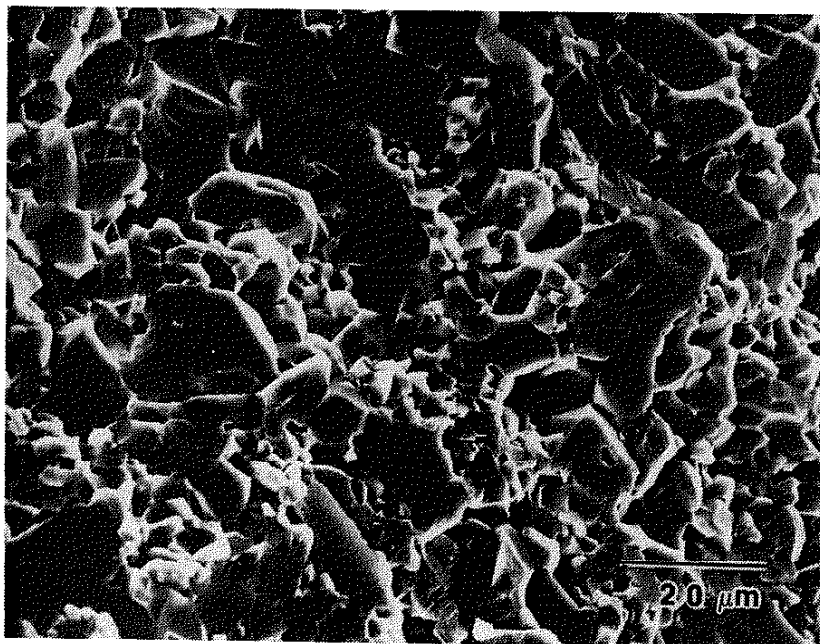


(A)

Figure 21 SEM micrographs demonstrating the typical fracture surface in static fatigue specimens failed at room temperature. (A) macroscopic view, (B) high magnification view in the slow crack growth region, and (C) high magnification view in the fast fracture zone. ($\sigma_{\max} = 234.4 \text{ MPa}$)

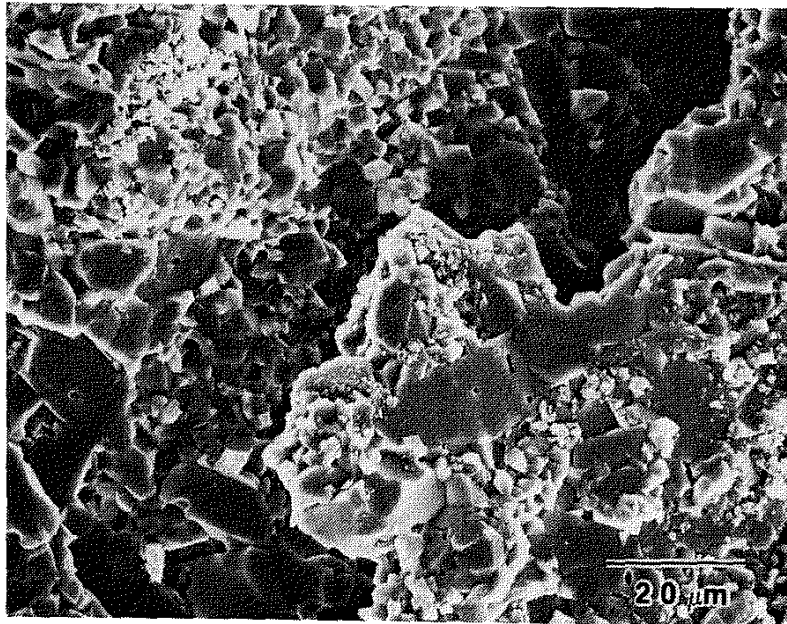


(B)

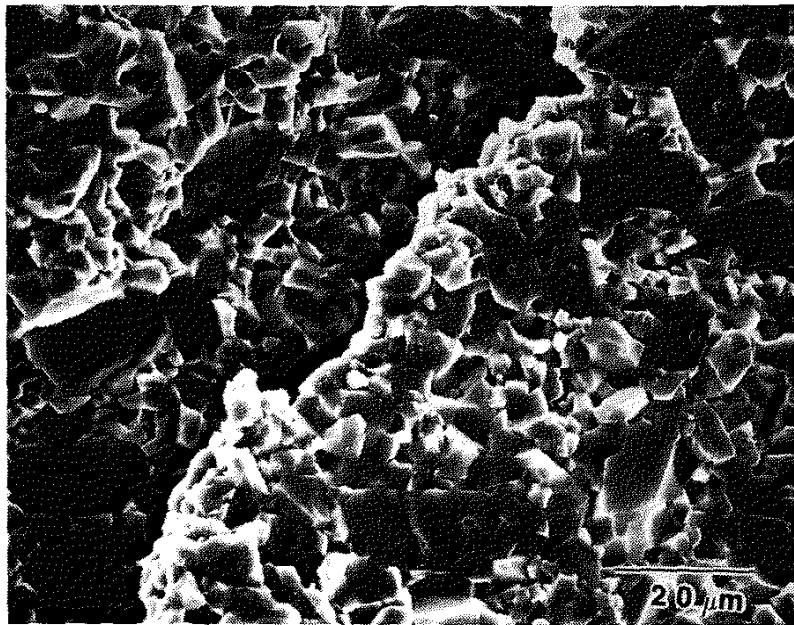


(C)

Figure 21 (Continued)

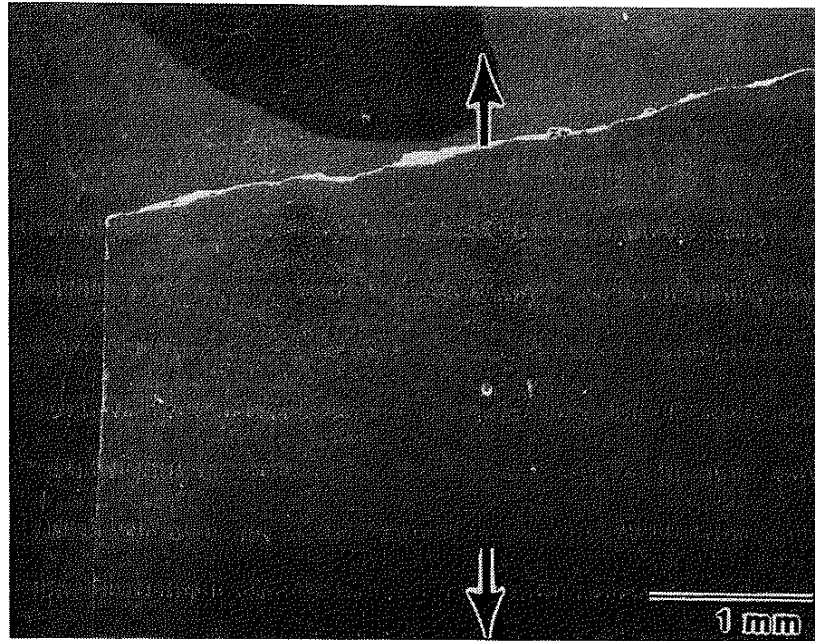


(A)

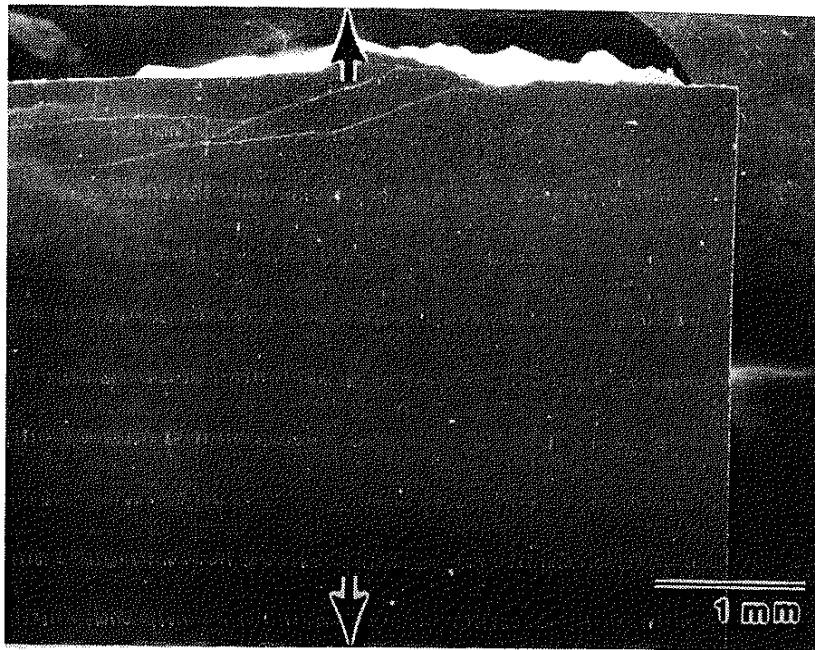


(B)

Figure 22 Debris formation observed around the macrocrack branching areas on the fracture surface in both (A) static fatigue and (B) cyclic fatigue specimens failed at room temperature.

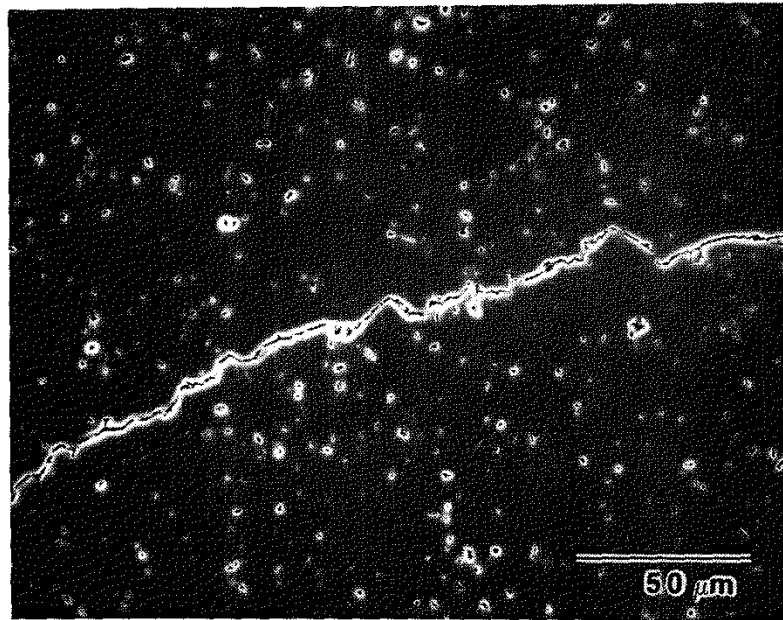


(A)

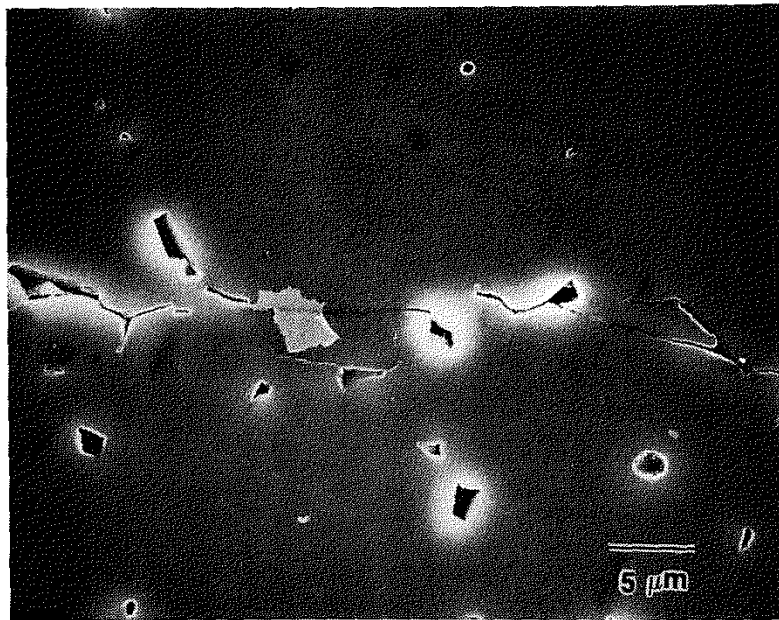


(B)

Figure 23 SEM micrographs of the axially sectioned view in fractured specimens under different loading conditions at room temperature. (A) static loading ($\sigma_{\max} = 234.4$ MPa) and (B) cyclic loading ($\sigma_{\max} = 220.6$ MPa, 2 Hz). (Arrows indicate the loading direction.)

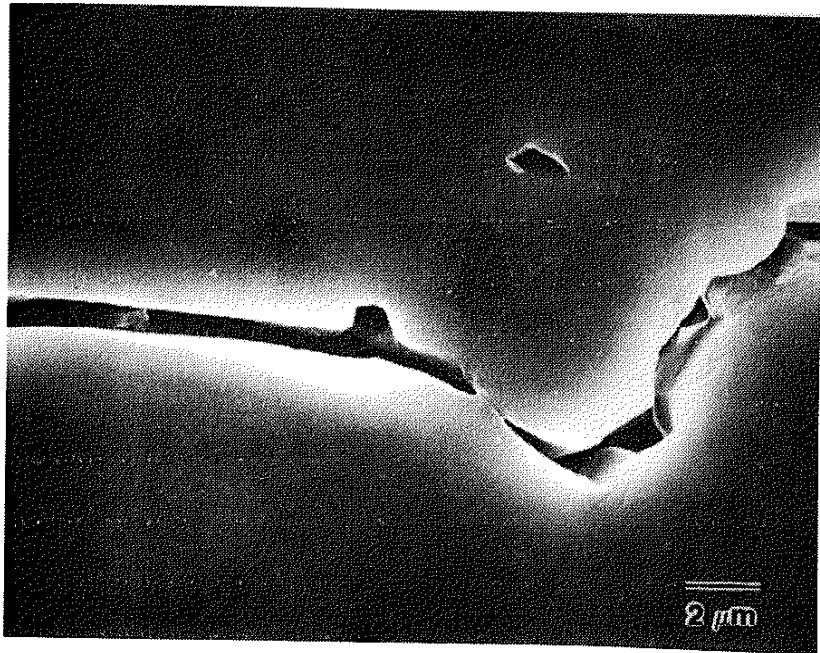


(A)

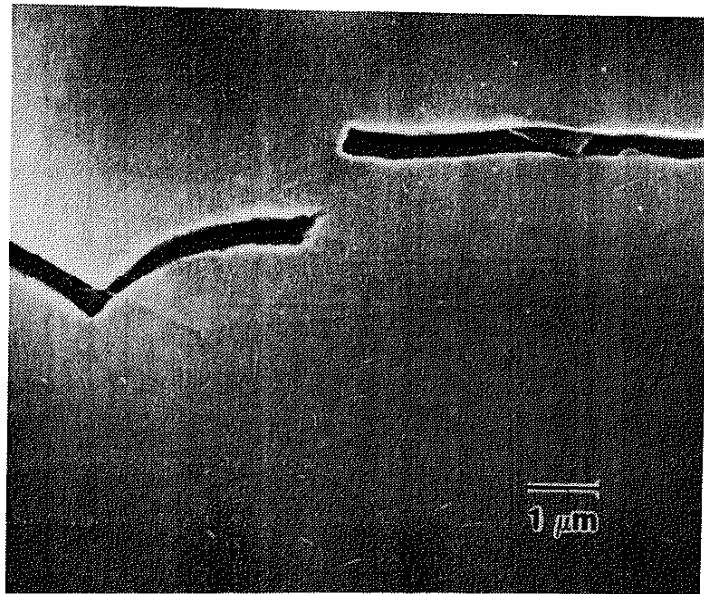


(B)

Figure 24 Some typical features observed along the crack paths in room temperature cyclic fatigue specimens. (A) crack deflection, (B) interlocking grains, (C) contact of fracture surface asperities, (D) an unbroken ligament, and (E) trapped grains within the closed crack.

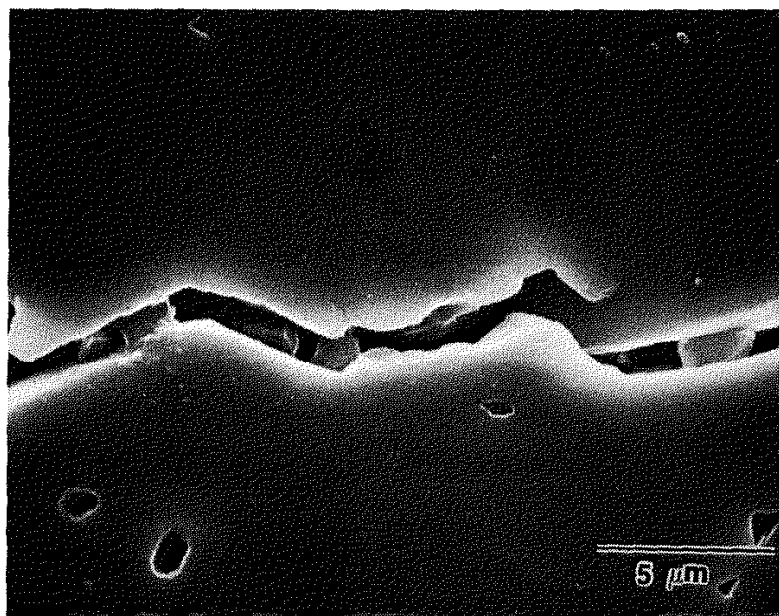


(C)



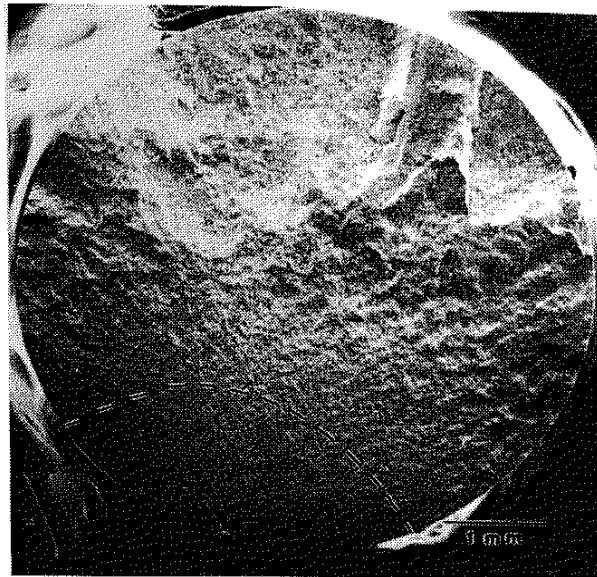
(D)

Figure 24 (Continued)



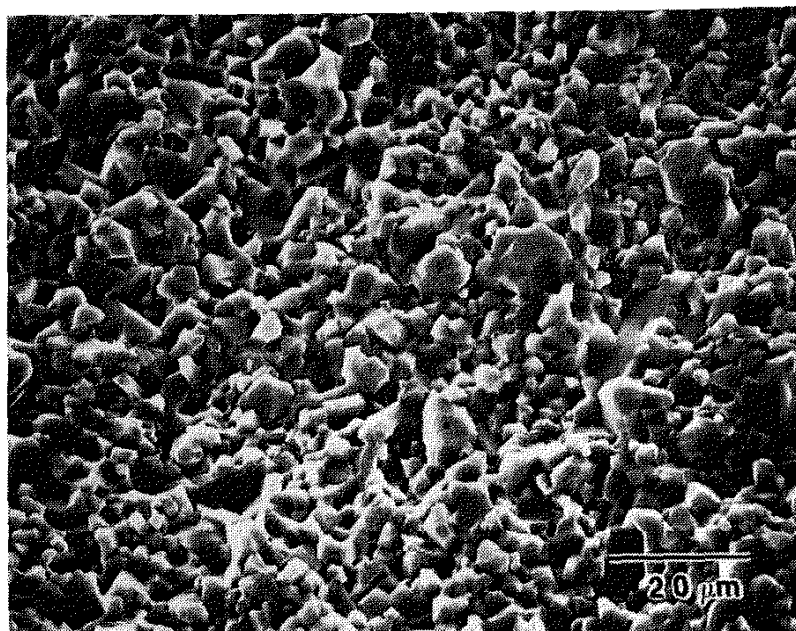
(E)

Figure 24 (Continued)

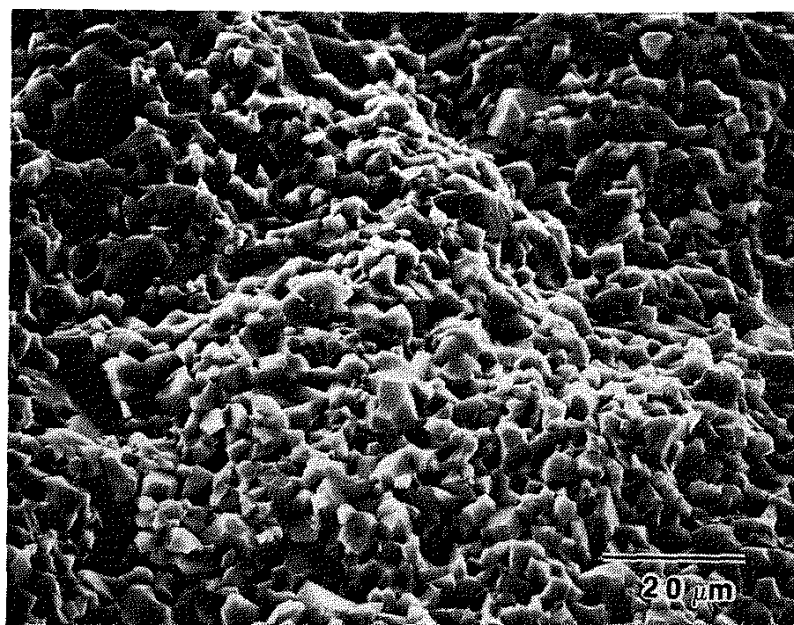


(A)

Figure 25 SEM micrographs demonstrating the typical fracture surface in sine wave form specimens failed at 1200°C. (A) macroscopic view, (B) high magnification view in the slow crack growth region, and (C) high magnification view in the fast fracture zone. ($\sigma_{\max} = 86.2$ MPa)



(B)



(C)

Figure 25 (Continued)

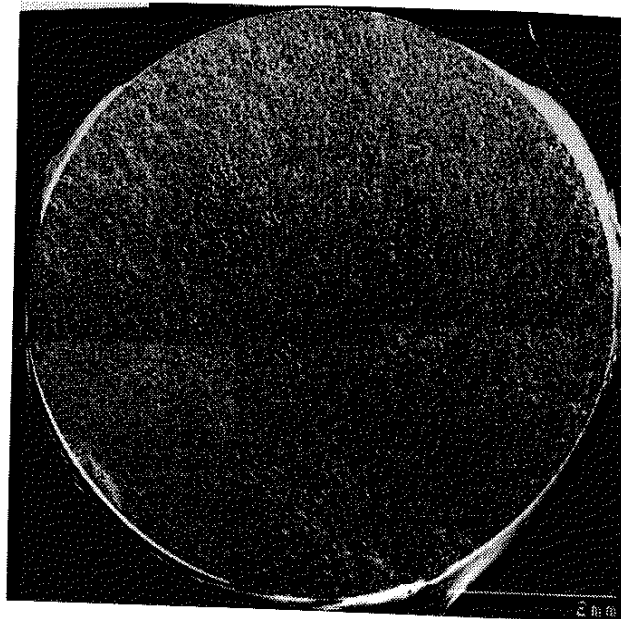


Figure 26 Macroscopic SEM view of the typical fracture surface in square wave form specimens ($R = 0.1$) failed at 1200°C . ($\sigma_{\text{max}} = 86.2 \text{ MPa}$)

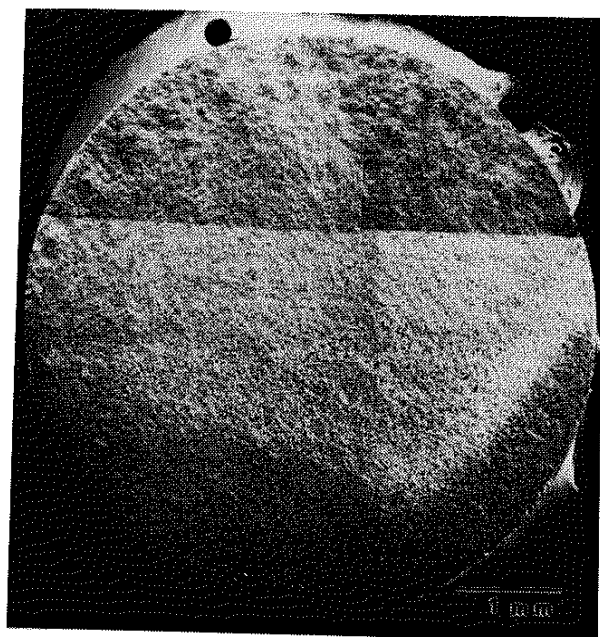


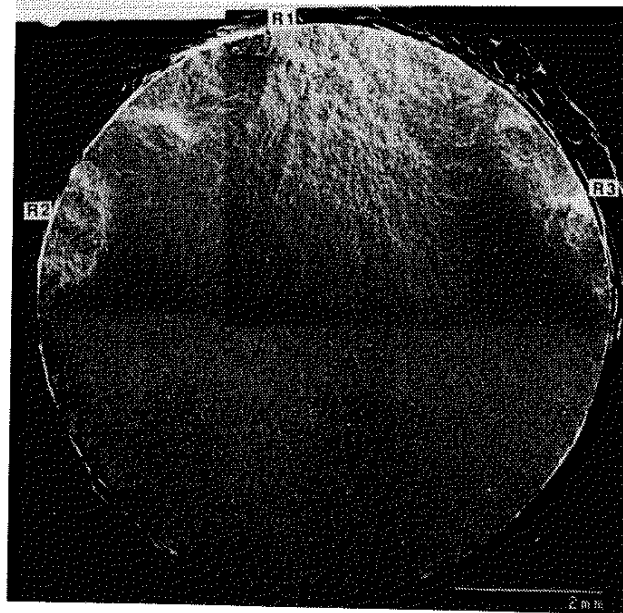
Figure 27 Macroscopic SEM view of the typical fracture surface in square wave form specimens ($R = 0.5$) failed at 1200°C . ($\sigma_{\text{max}} = 48.3 \text{ MPa}$)



Figure 28 Macroscopic SEM view of the typical fracture surface in trapezoid I wave form specimens failed at 1200°C. ($\sigma_{\max} = 86.2$ MPa)

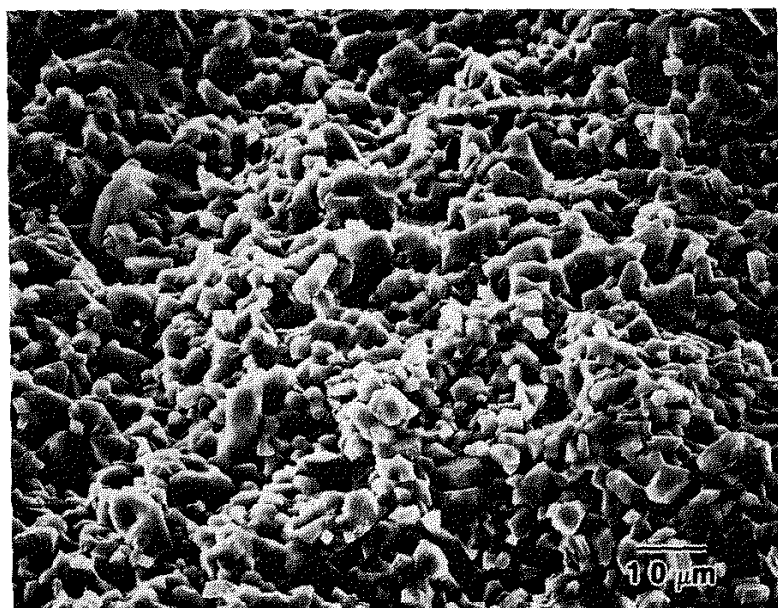


Figure 29 Macroscopic SEM view of the typical fracture surface in trapezoid II wave form specimens failed at 1200°C. ($\sigma_{\max} = 34.5$ MPa)

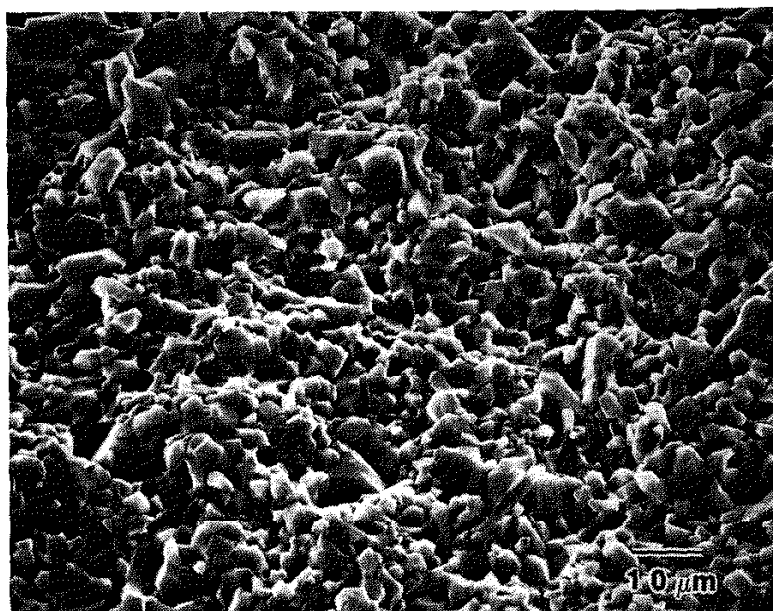


(A)

Figure 30 SEM micrographs demonstrating the typical fracture surface in static loading specimens failed at 1200°C. (A) macroscopic view, (B) high magnification view in the slow crack growth region, and (C) high magnification view in the fast fracture zone. ($\sigma_{\max} = 34.5$ MPa)

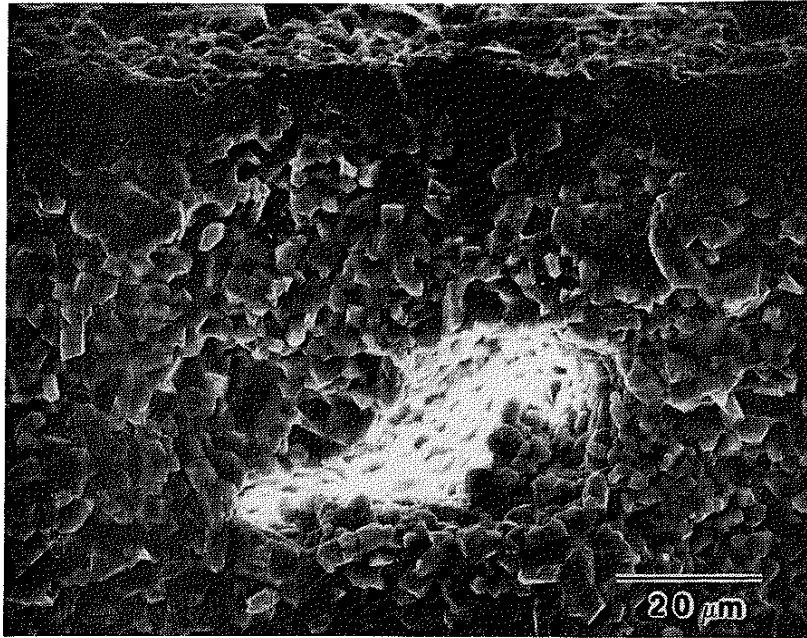


(B)

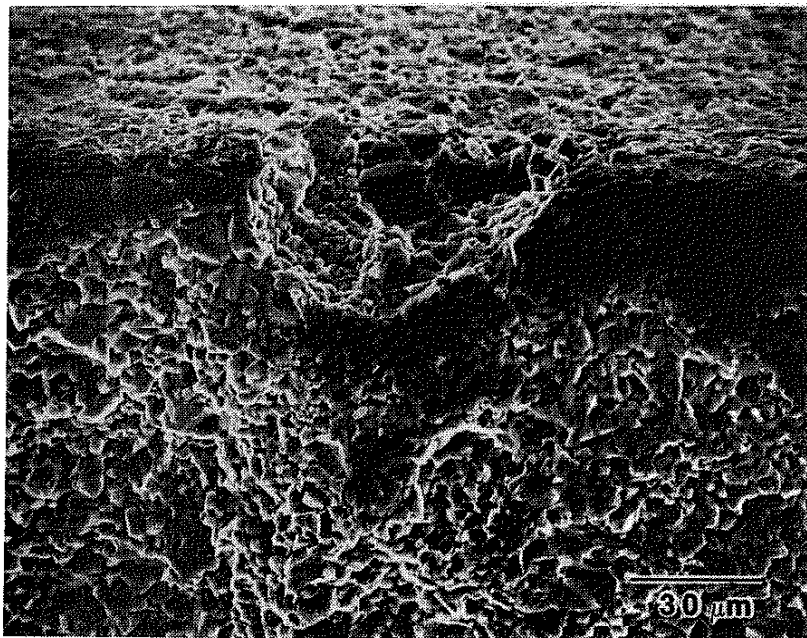


(C)

Figure 30 (Continued)

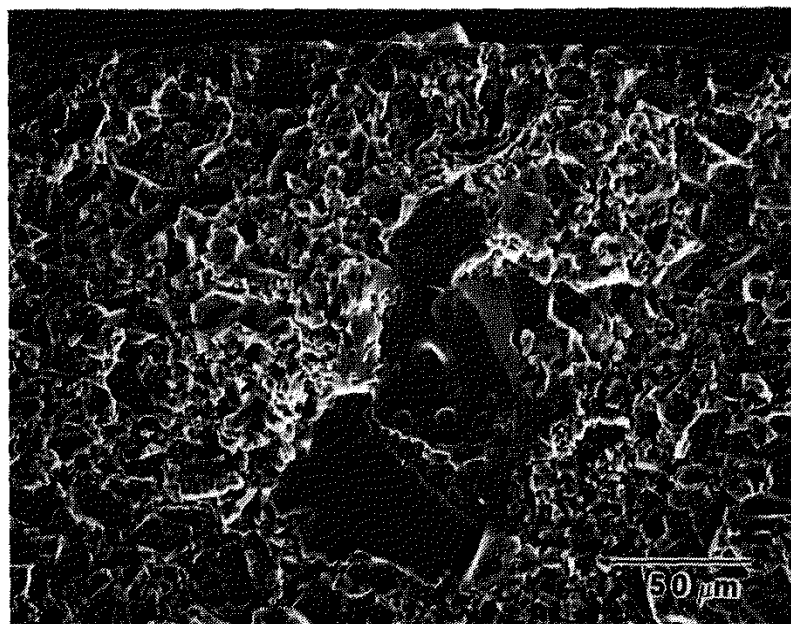


(A)



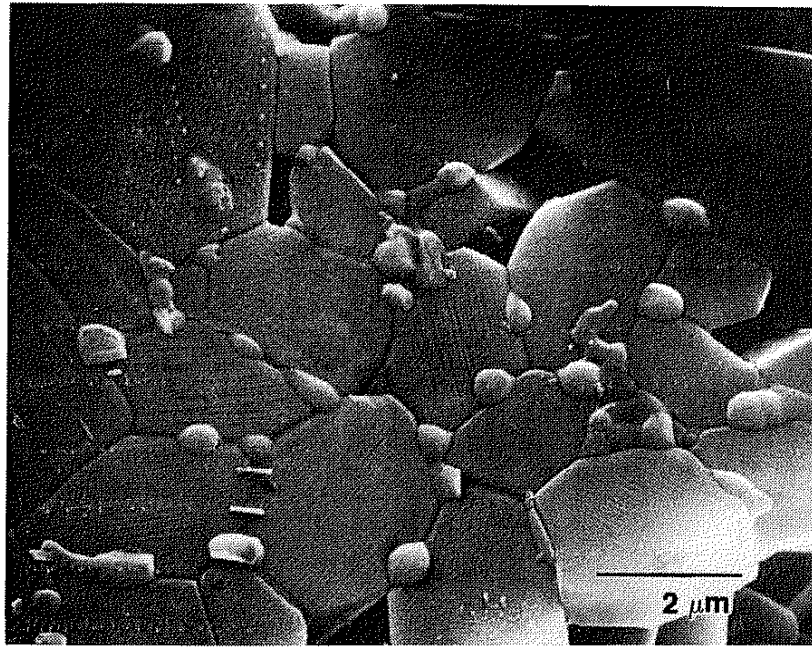
(B)

Figure 31 Typical failure origins at all applied loading conditions at 1200°C. (A) a large void near the edge of the fracture surface (square, $R = 0.1$, $\sigma_{\max} = 58.6$ MPa), (B) a large surface flaw (sine, $\sigma_{\max} = 86.2$ MPa), and (C) a large-grained agglomerate (static loading, $\sigma_{\max} = 34.5$ MPa).

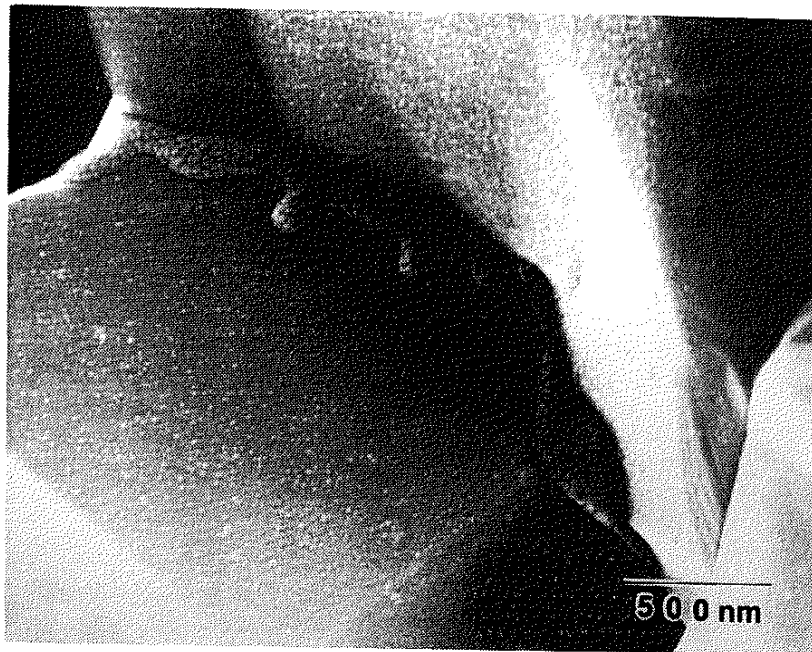


(C)

Figure 31 (Continued)

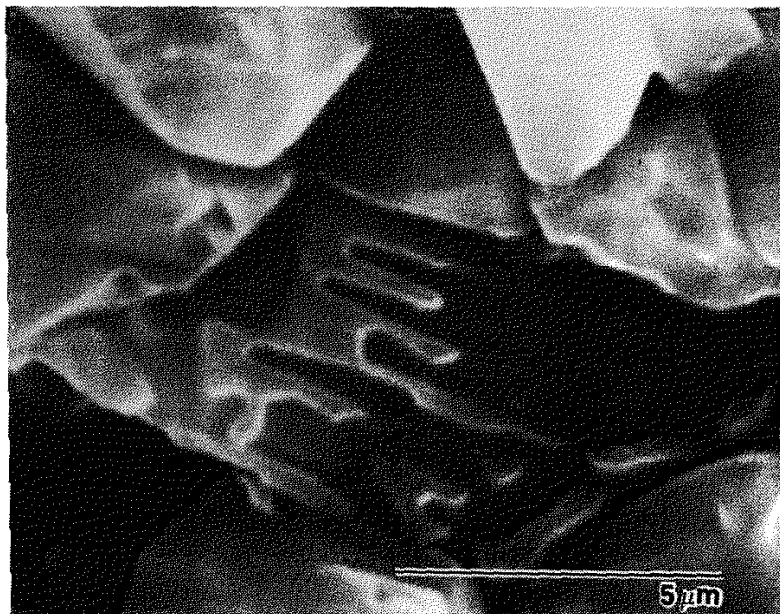


(A)



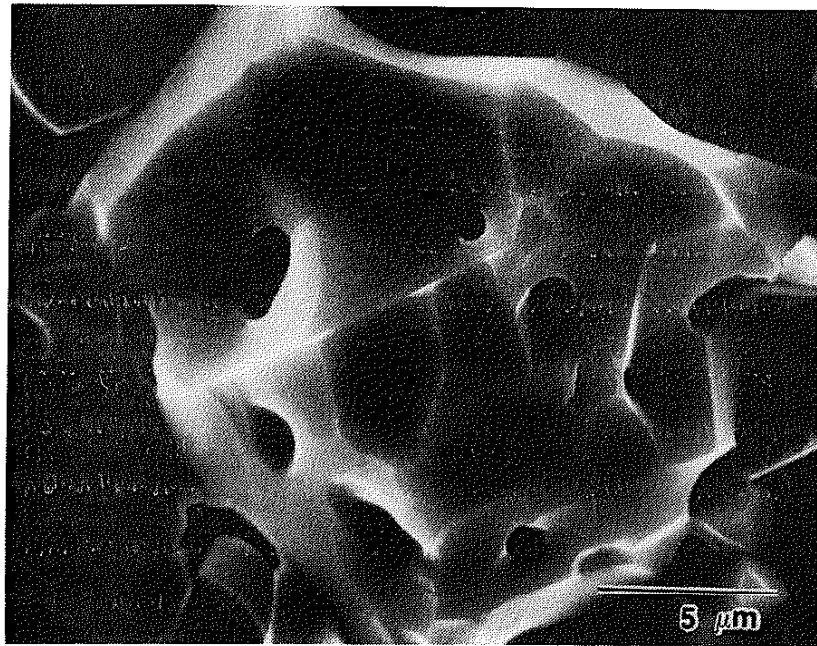
(B)

Figure 32 Typical profiles of the glassy phase on fracture surface in different loading conditions at 1200°C. (A) sine wave form ($\sigma_{\max} = 86.2$ MPa), (B) trapezoid II wave form ($\sigma_{\max} = 34.5$ MPa), and (C) static loading, ($\sigma_{\max} = 34.5$ MPa).

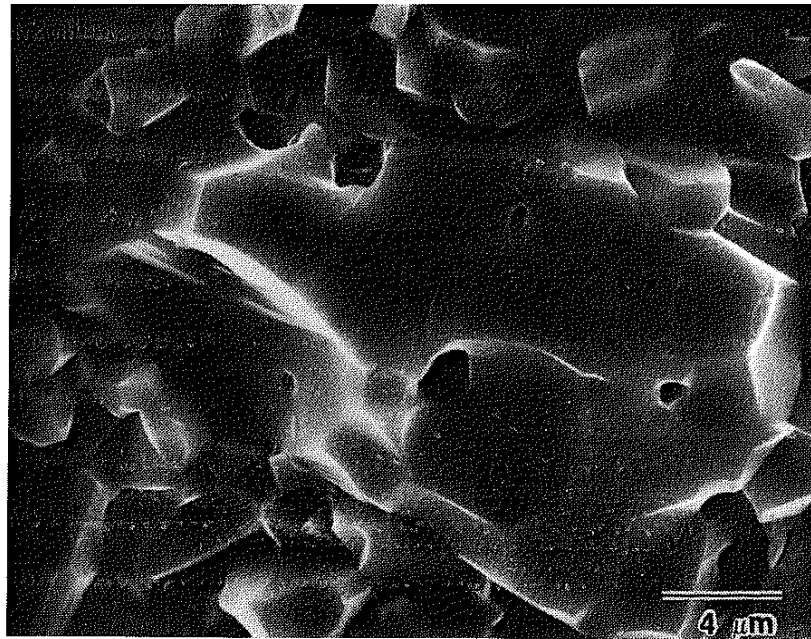


(C)

Figure 32 (Continued)



(A)



(B)

Figure 33 Comparison of the SEM micrographs of the grain facets in the areas without glassy phase on the fracture surface in the (A) room and (B) high temperature specimens.

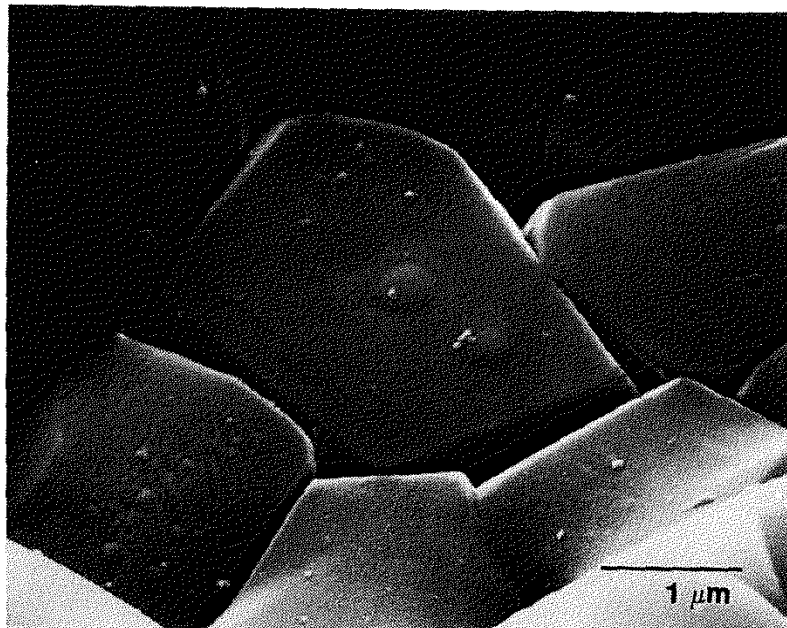
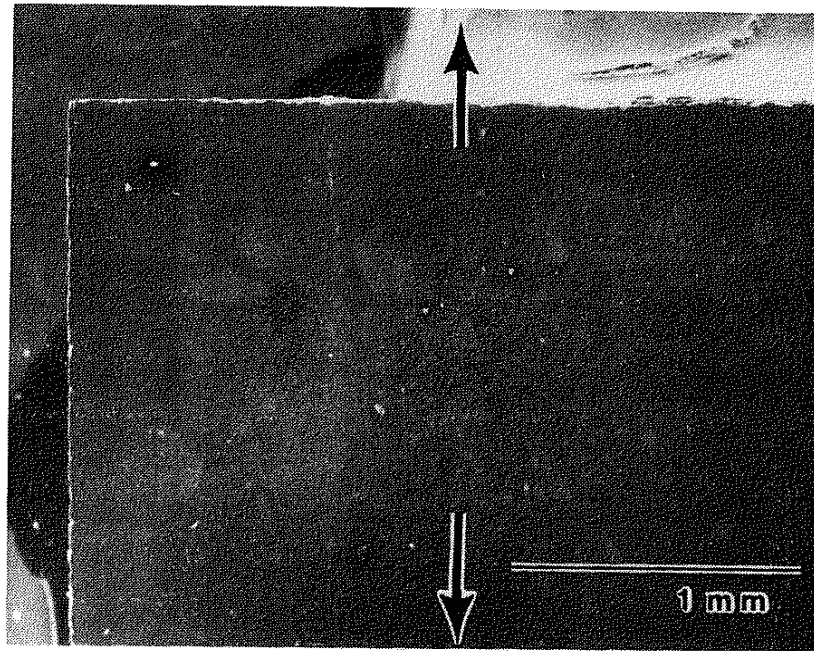
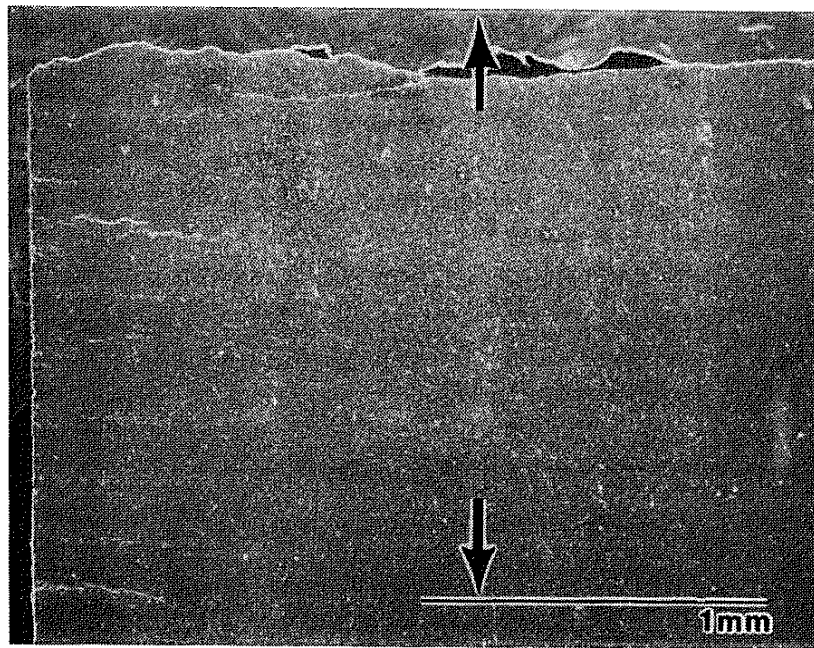


Figure 34 Evidence of grain-boundary sliding from the SEM micrograph of a trapezoid II wave form specimen failed with $\sigma_{\max} = 34.5$ MPa at 1200°C.

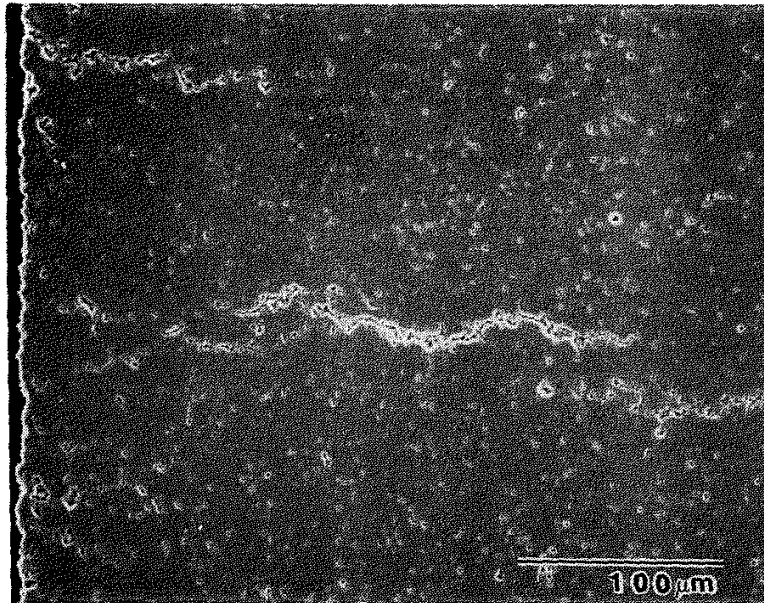


(A)

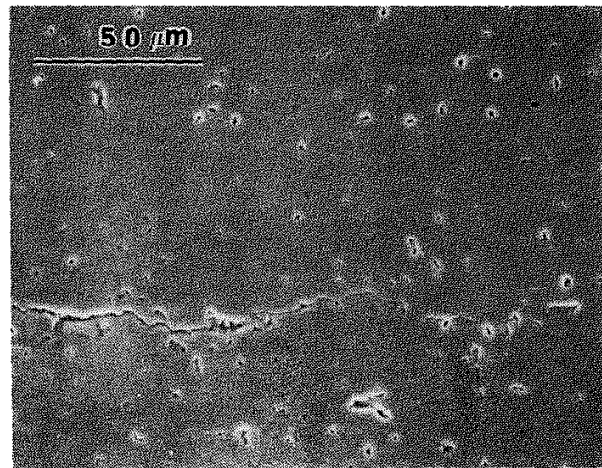


(B)

Figure 35 SEM micrographs of the axially sectioned view in fractured specimens under different loading conditions at 1200°C. (A) sine wave form ($\sigma_{\max} = 62$ MPa), (B) static loading ($\sigma_{\max} = 34.5$ MPa), (C) high magnification view of the non-failure-induced macrocracks in (B), and (D) the area around the crack tip of a non-failure-induced macrocrack in (C). (Arrows indicate the loading direction.)

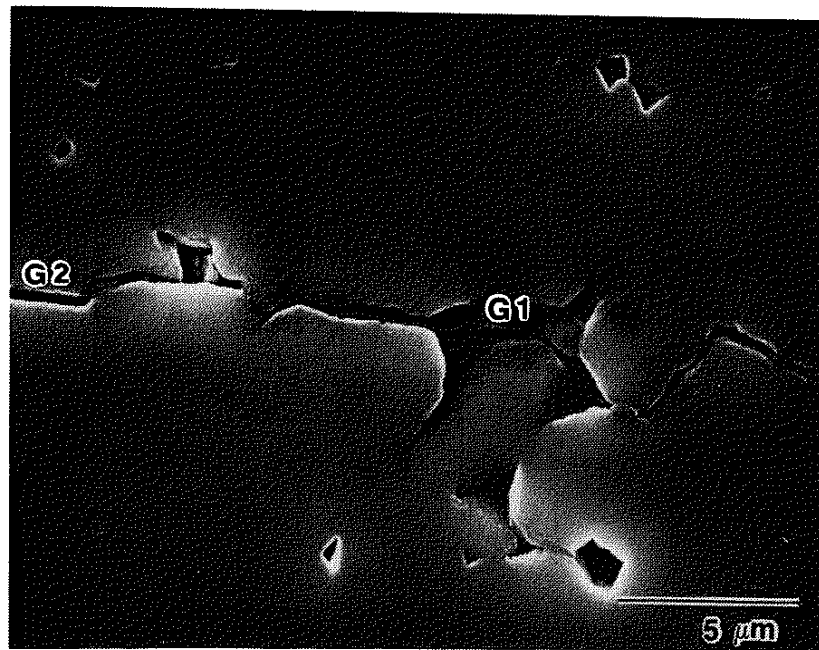


(C)



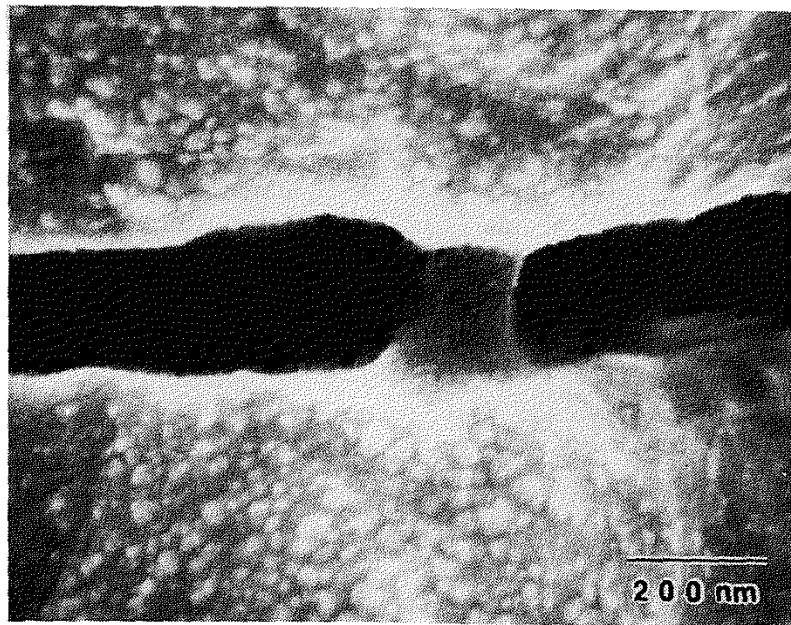
(D)

Figure 35 (Continued)

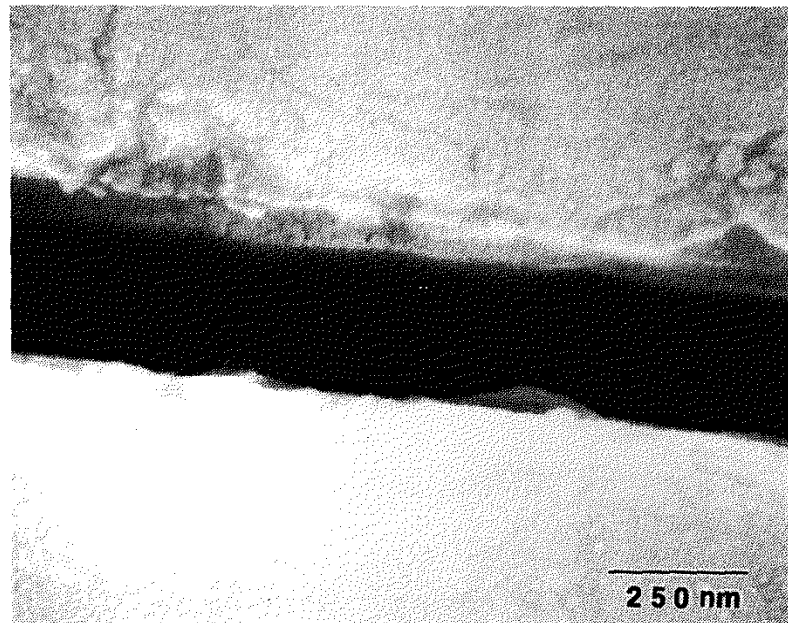


(A)

Figure 36 High magnification SEM view of the crack profile in an axially-cut section of a static loading specimen ($\sigma_{\max} = 34.5$ MPa) failed at 1200°C. (A) typical crack path, (B and C) enlarged views showing the viscous glassy phases bridging the crack surfaces at marked segments, G1 and G2, respectively, in (A).

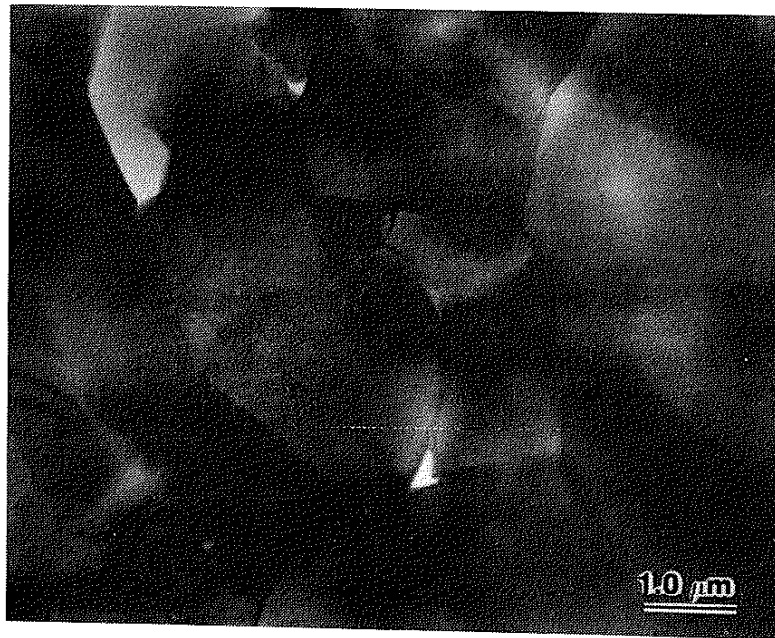


(B)

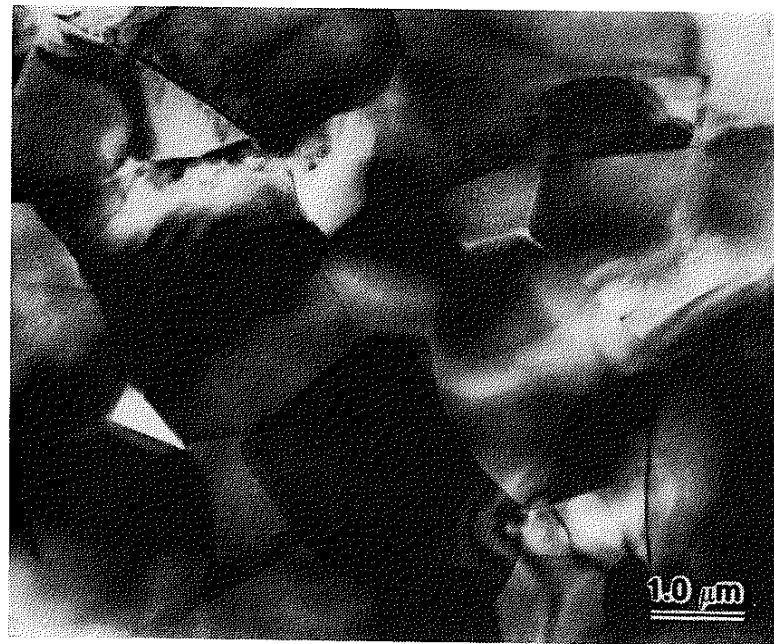


(C)

Figure 36 (Continued)

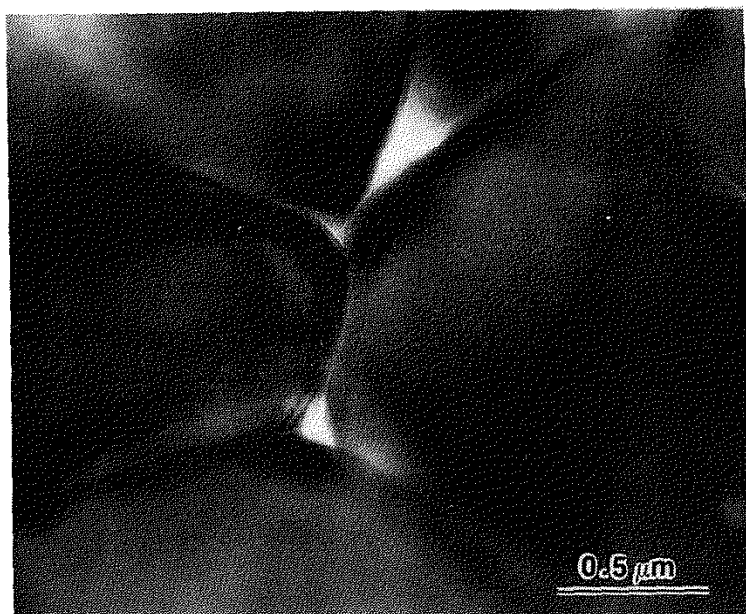


(A)

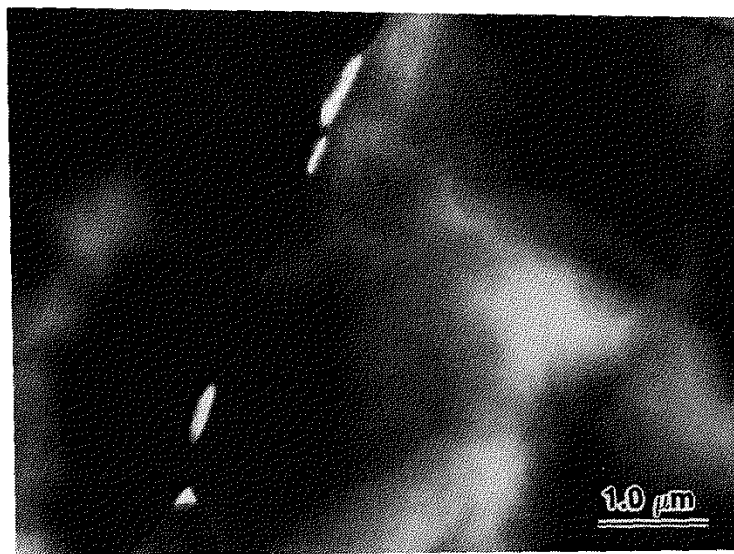


(B)

Figure 37 TEM micrographs of the general structure after failure in room temperature (A) static and (B) cyclic fatigue specimens.



(A)



(B)

Figure 38 TEM micrographs demonstrating (A) growth and linkage of pores in a static loading specimen ($\sigma_{\max} = 34.5$ MPa) and (B) isolated pores (no linkage of pores was observed) in a sine wave form specimen ($\sigma_{\max} = 62$ MPa).

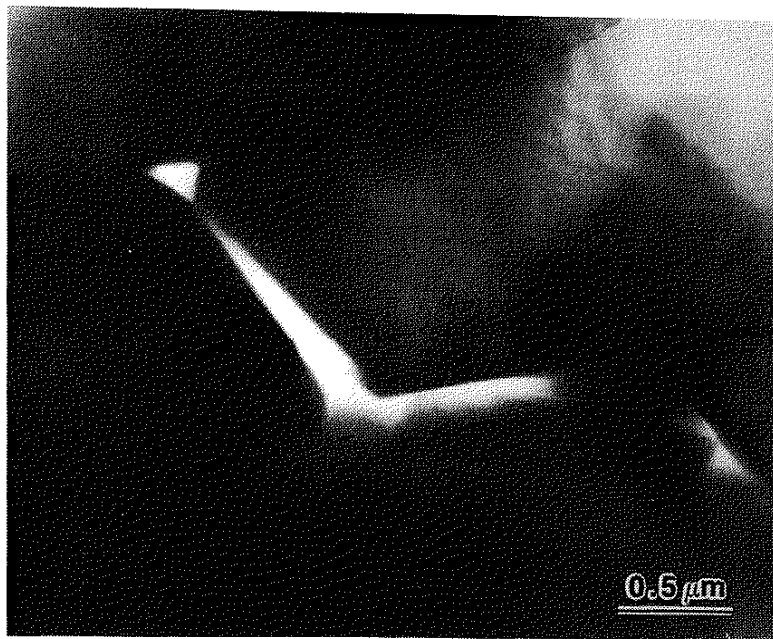


Figure 39 Evidence of grain-boundary sliding in the TEM micrograph of a static loading specimen failed with $\sigma_{\max} = 34.5$ MPa at 1200°C.

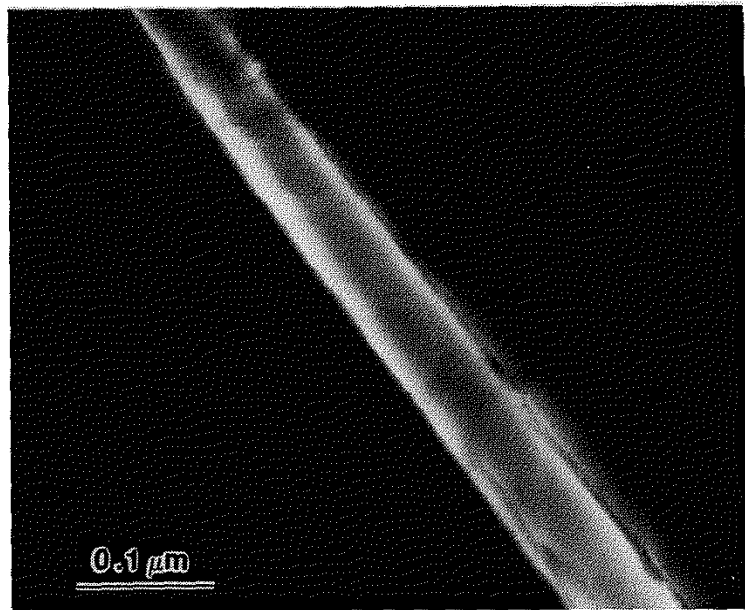


Figure 40 TEM micrograph showing a side view of the finger-like meniscus of the viscous glassy phase between two alumina grains.

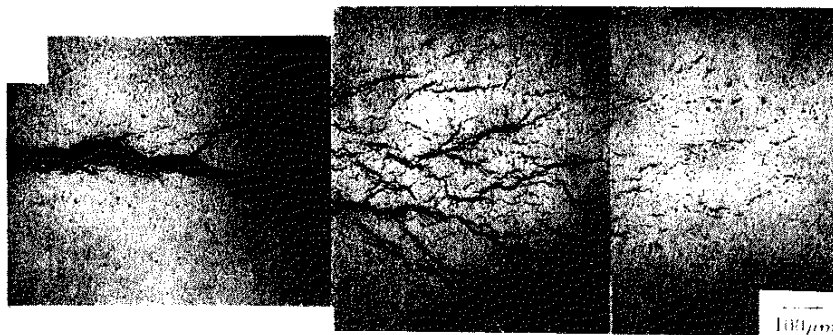


Figure 41 A damage zone of distributed microcracking ahead of a long fatigue crack in an Al_2O_3 -33 vol.% SiC whisker composite subjected to cyclic tensile loads (in four-point flexure) in 1500°C air environment. (From Ref. 62)



Figure 42 Microcrack coalescence through shear band formation on the tensile surface of a bend bar of AVCO alumina deformed at 100 MPa and 1150°C. Bars = 0.1 mm. (From Ref. 82)

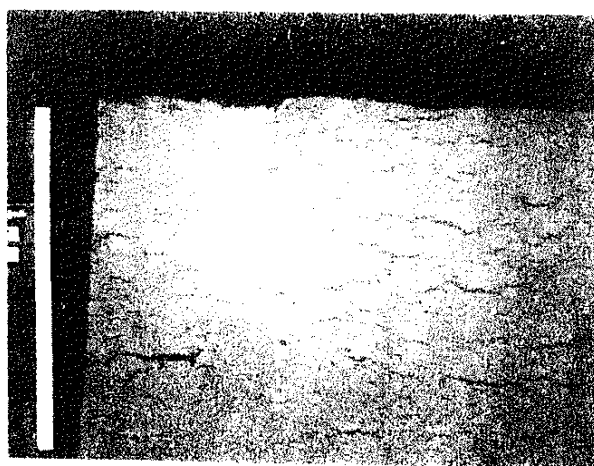


Figure 43 Extensive microcracking is visible on the side of a tensile specimen of ARCO alumina deformed at 100 MPa and 1250°C. Bar = 1 mm. (From Ref. 82)



Figure 44 Microcracking and crack-tip blunting on an internal section of a tensile specimen of ARCO alumina deformed at 55 MPa and 1250°C. Bars = 10 μm . (From Ref. 82)

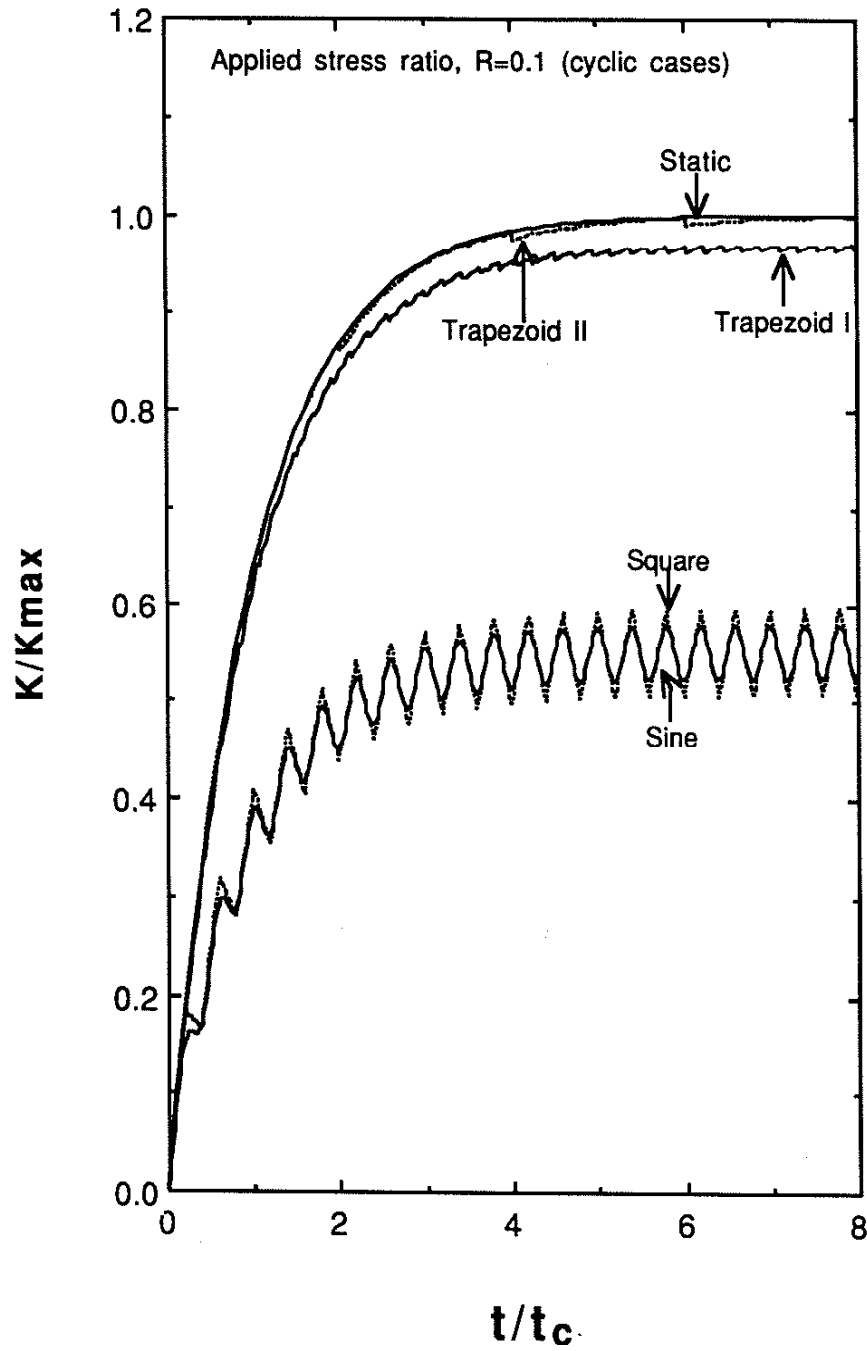


Figure 45 Comparison of the calculated effective stress intensity factors at the crack tip in static loading and various cyclic loading wave forms at 1200°C under the same maximum applied stress intensity factor, K_{max} .

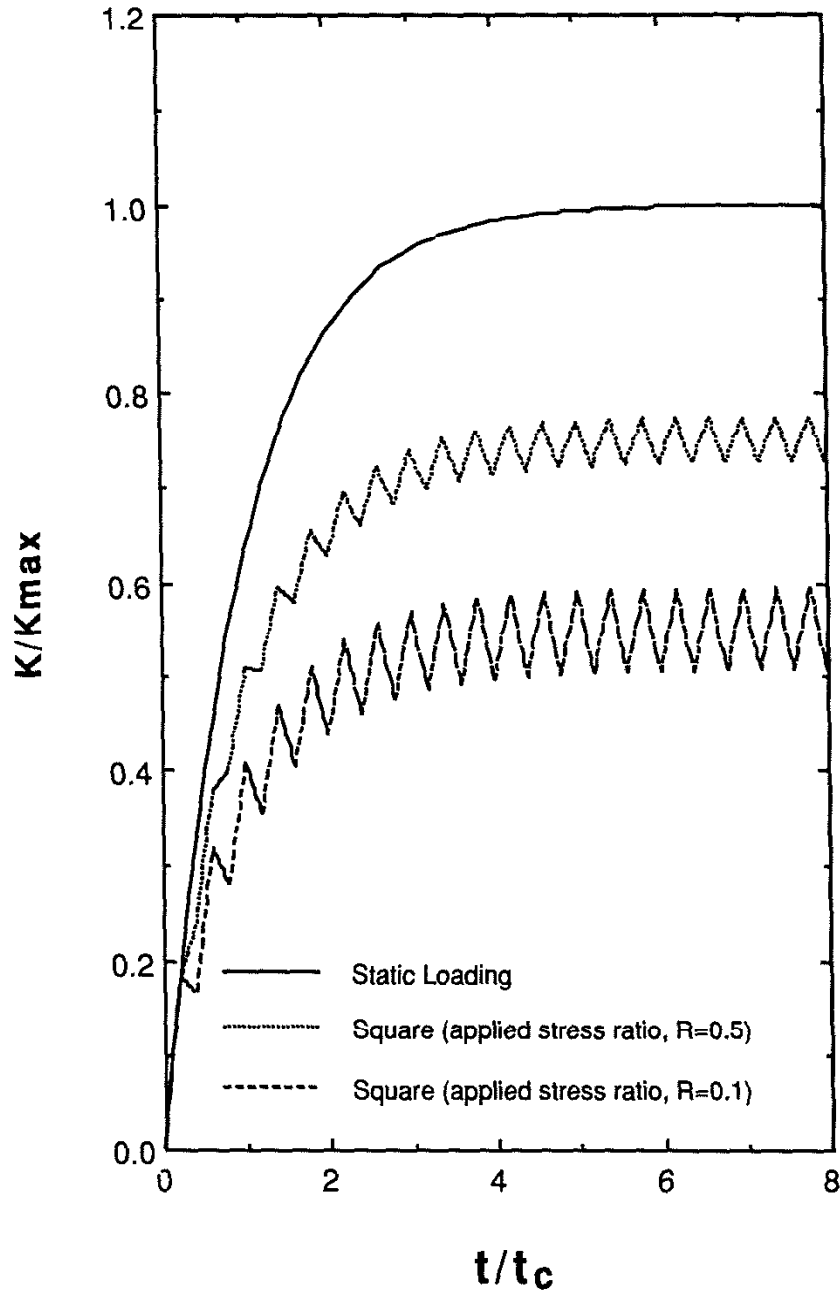


Figure 46 Comparison of the calculated effective stress intensity factors at the crack tip in static loading and square loading wave forms ($R = 0.1$ and 0.5) at 1200°C under the same maximum applied stress intensity factor, K_{max} .

REFERENCES

1. L. S. Williams, "Stress-Endurance of Sintered Alumina," *Trans. Br. Ceram. Soc.*, **55** [5] 287-312 (1956).
2. L. S. Williams, "Fatigue and Ceramics"; pp. 245-302 in *Mechanical Properties of Engineering Ceramics*, Edited by W. Kriegel and H. Palmour, Interscience Publishers, New York, 1961.
3. J. S. Mizushima and W. J. Knapp, "Behavior of a Ceramic under Cyclic Loading," *Ceram. News*, **5** [12] 26-29, 36 (1956).
4. D. A. Krohn and D. P. H. Hasselman, "Static and Cyclic Fatigue Behavior of a Polycrystalline Alumina," *J. Am. Ceram. Soc.*, **55** [4] 208-11 (1972).
5. A. G. Evans and E. R. Fuller, "Crack Propagation in Ceramic Materials under Cyclic Loading Conditions," *Metall. Trans. A*, **5** [1] 27-33 (1974).
6. A. G. Evans, "Fatigue in Ceramics," *Int. J. Fract.*, **16** [6] 485-98 (1980).
7. S. Lathabai, Y.-W. Mai and B. R. Lawn, "Cyclic Fatigue Behavior of an Alumina Ceramic with Crack-Resistance Characteristics," *J. Am. Ceram. Soc.*, **72** [9] 1760-63 (1989).
8. T. Kawakubo, N. Okabe, and T. Mori, "Static and Cyclic Fatigue Behavior in Ceramics"; pp. 717-26 in *Fatigue 90*, Vol. 2, Edited by H. Kitagawa and T. Tanaka, Materials and Component Engineering Publications Ltd., Birmingham, U.K., 1990.
9. A. G. Evans, L. R. Russell, and D. W. Richerson, "Slow Crack Growth in Ceramic Materials at Elevated Temperatures," *Metall. Trans. A*, **6** [4] 707-16 (1975).
10. M. Kawai, H. Fujita, Y. Kanki, H. Abe, and J. Nakayama, "Tensile Testing of Silicon Carbide and Silicon Nitride"; pp. 269-78 in *Proceedings of the First International Symposium on Ceramic Components for Engines*, Edited by S. Somiya, E. Kanai, and K. Ando, Elsevier Applied Science Publishers Ltd., London, 1983.
11. Y. Matsuo, Y. Hattori, Y. Katayama, and I. Fukuura, "Cyclic Fatigue Behavior of Ceramics"; pp. 515-22 in *Progress in Nitrogen Ceramics*, Edited by F. L. Riley, Martinus Nijhoff Publishers, The Hague, The Netherlands 1983.
12. L. A. Sylva and S. Suresh, "Crack Growth in Transforming Ceramics under Cyclic Tensile Loads," *J. Mater. Sci.*, **24**, 1729-38 (1989).
13. S. Horibe and M. Sumita, "Fatigue Behavior of Sintered SiC: Temperature Dependence and Effect of Doping with Aluminium," *J. Mater. Sci.*, **23**, 3305-13 (1988).
14. E. B. Shand, "Stress Behavior of Brittle Materials," *Am. Ceram. Soc. Bull.*, **38** [11] 653-60 (1959).
15. R. Sedlacek and F. A. Halden, "Static and Cyclic Fatigue of Alumina"; pp. 211-20 in *Structural Ceramics and Testing of Brittle Materials*, Edited by S. J. Acquaviva and S. A. Bortz, Gordon and Breach Science Publishers, New York, 1968.

16. B. K. Sarkar and T. G. J. Glinn, "Fatigue Behavior of High- Al_2O_3 Ceramics," *Trans. Br. Ceram. Soc.*, **69**, 199-203 (1970).
17. F. Guiu, "Cyclic fatigue of Polycrystalline Alumina in Direct Push-Pull," *J. Mater. Sci. Lett.*, **13** [6] 1357-61 (1978).
18. L. Ewart and S. Suresh, "Dynamic Fatigue Crack Growth in Polycrystalline Alumina under Cyclic Compression," *J. Mater. Sci. Lett.*, **5** [4] 774-78 (1986).
19. L. Ewart and S. Suresh, "Crack Propagation in Ceramics under Cyclic Loads," *J. Mater. Sci. Lett.*, **22** [4] 1173-92 (1987).
20. J. R. Brockenbrough and S. Suresh, "Constitutive Behavior of a Microcracking Brittle Solid in Cyclic Compression," *J. Mech. Phys. Solids*, **35** [6] 721-42 (1987).
21. S. Suresh and J. R. Brockenbrough, "Theory and Experiments of Fracture in Cyclic Compression: Single Phase Ceramics, Transforming Ceramics and Ceramic Composites," *Acta Metall.*, **36** [6] 1455-70 (1988).
22. M. J. Reece, F. Guiu and M. F. R. Sammur, "Cyclic Fatigue Crack Propagation in Alumina under Direct Tension-Compression Loading," *J. Am. Ceram. Soc.*, **72** [2] 348-52 (1989).
23. G. Grathwohl, "Fatigue of Ceramics under Cyclic Loading," *Mat.-wiss. u. Werkstofftech.*, **19**, 113-24 (1988).
24. S. Horibe, "Fatigue of Silicon Nitride Ceramics under Cyclic Loading," *J. European Ceram. Soc.*, **6**, 89-95 (1990).
25. H. Kishimoto, A. Ueno, and H. Kawamoto, "Crack Propagation Behavior of Si_3N_4 under Cyclic Loads-Influence of Difference in Materials"; pp. 727-32 in *Fatigue 90*, Vol. 2, Edited by H. Kitagawa and T. Tanaka, Materials and Component Engineering Publications Ltd, Birmingham, U.K., 1990.
26. I. Bar-On and J. T. Beals, "Fatigue in Silicon Nitride Bend Bars"; pp. 793-98 in *Fatigue 90*, Vol. 2, Edited by H. Kitagawa and T. Tanaka, Materials and Component Engineering Publications Ltd, Birmingham, U.K., 1990.
27. M. V. Swain, "Lifetime Prediction of Ceramic Materials," *Mater. Forum*, **9** [1&2] 34-44 (1986).
28. M. V. Swain and V. Zelizko, "Comparison of Static and Cyclic Fatigue on Mg-PSZ Alloys"; pp. 595-606 in *Advances in Ceramics, Vol. 24: Science and Technology of Zirconia III*, Edited by S. Somiya, N. Yamamoto, and H. Yanagida, The American Ceramic Society, Inc., Westerville, Ohio, 1988.
29. R. H. Dauskardt, W. Yu, and R. O. Ritchie, "Fatigue Crack Propagation in Transformation-Toughened Zirconia Ceramic," *J. Am. Ceram. Soc.*, **70** [10] C-248-C-252 (1987).
30. R. H. Dauskardt, D. B. Marshall, and R. O. Ritchie, "Cyclic Fatigue-Crack Propagation in Magnesia-Partially-Stabilized Zirconia Ceramics," *J. Am. Ceram. Soc.*, **73** [4] 893-903 (1990).

31. J.-F. Tsai, C.-S. Yu, and D. K. Shetty, "Fatigue Crack Propagation in Ceria-Partially-Stabilized Zirconia [Ce-TZP]-Alumina Composites," *J. Am. Ceram. Soc.*, **73** [10] 2992-3001 (1990).
32. S. Horibe, "Cyclic Fatigue Damage and Microstructure of Ceramic Materials"; pp. 753-58 in *Fatigue 90*, Vol. 2, Edited by H. Kitagawa and T. Tanaka, Materials and Component Engineering Publications Ltd, Birmingham, U.K., 1990.
33. C. P. Chen and W. J. Knapp, "Fatigue Fracture of an Alumina Ceramic at Several Temperatures"; pp. 691-707 in *Fracture Mechanics of Ceramics*, Vol. 2, Edited by R. C. Bradt, D. P. H. Hasselman and F. F. Lange, Plenum Press, New York, 1974.
34. T. Kawakubo and K. Komeya, "Static and Cyclic Fatigue Behavior of a Sintered Silicon Nitride at Room Temperature," *Int. J. Fract.*, **16** [6] 485-98 (1980).
35. A. Ueno, H. Kishimoto, H. Kawamoto, and M. Asakura, "Crack Propagation Behavior of Sintered Silicon Nitride under Cyclic Load of High Stress Ratio and High Frequency"; pp. 733-38 in *Fatigue 90*, Vol. 2, Edited by H. Kitagawa and T. Tanaka, Materials and Component Engineering Publications Ltd, Birmingham, U.K., 1990.
36. K. Ohya, K. Ogura, M. Takatsu, and H. Kamiya, "Cyclic Fatigue Test of PSZ by Using a Piezoelectric Bimorph Actuator-Effect of Stress Amplitude and Frequency"; pp. 557-62 in *Structural Ceramics/Fracture Mechanics*, Proceedings of the MRS International Meeting on Advanced Materials, Vol. 5 (Tokyo, Japan, June, 1988). Edited by Y. Hamano, O. Kamigaito, T. Kishi, and M. Sakai., Materials Research Society, Pittsburgh, PA, 1989.
37. E. Glenny and T. A. Taylor, "The High-Temperature Properties of Ceramics and Cermets," *Powder Metallurgy*, [1/2] 189-226 (1958).
38. K. C. Liu and C. R. Brinkman, "Tensile Cyclic Fatigue of Alumina at Room and Elevated Temperatures"; pp. 191-200 in Proceedings of the 24th Automotive Technology Development Contractors' Meeting, P-197 (Dearborn, MI, Oct. 27-30, 1986). Society of Automotive Engineers, Inc., Warrendale, PA., 1987.
39. H. N. Ko, "Fatigue Strength of Sintered Al_2O_3 under Rotary Bending," *J. Mater. Sci. Lett.*, **5** [4] 464-66 (1986).
40. H. N. Ko, "Effect of Grain Size on Fatigue Strength of Sintered Al_2O_3 under Rotary Bending," *J. Mater. Sci. Lett.*, **8**, 1438-41 (1989).
41. H. N. Ko, "Cyclic Fatigue Behavior of High-Strength Sintered Si_3N_4 under Rotary Bending," *J. Mater. Sci. Lett.*, **10**, 545-48 (1991).
42. T. Hoshide, T. Ohara, and T. Yamada, "Fatigue Crack Growth from Indentation Flaw in Ceramics," *Int. J. Fract.*, **37** [1] 47-59 (1988).
43. R. Kossowsky, "Cyclic Fatigue of Hot-Pressed Si_3N_4 ," *J. Am. Ceram. Soc.*, **56** [10] 531-35 (1973).
44. R. Kossowsky, "Creep and Fatigue of Si_3N_4 as Related to Microstructures"; pp. 347-71 in *Ceramics for High Performance Applications*, Edited by J. Burke, A. E. Gorum, and R. N. Katz, Brook Hill Publishing Co., Chestnut Hill, MA, 1974.

45. K. C. Liu and C. R. Brinkman, "Dynamic Tensile Cyclic Fatigue of Si_3N_4 "; pp. 189-97 in Proceedings of the 25th Automotive Technology Development Contractors' Coordination Meeting, P-209 (Dearborn, MI, Oct. 26-29, 1987). Society of Automotive Engineers, Inc., Warrendale, PA., 1988.
46. K. C. Liu and C. R. Brinkman, "High Temperature Tensile and Fatigue Strengths of Silicon Nitride"; pp. 235-44 in Proceedings of the 27th Automotive Technology Development Contractors' Coordination Meeting, P-230 (Dearborn, MI, Oct. 23-26, 1989). Society of Automotive Engineers, Inc., Warrendale, PA., 1990.
47. M. Masuda, T. Soma, M. Matsui, and I. Oda, "Cyclic Fatigue Testing of Ceramic Materials," *Int. J. High Technology Ceramics*, **4**, 289-99 (1988).
48. T. Soma, M. Masuda, M. Matsui, and I. Oda, "Fatigue of Ceramics (Part 1)-Fatigue Behavior of Sintered Si_3N_4 under Tension-Compression Cyclic Stress," *J. Ceram. Soc. Jpn.*, **96** [3] 277-83 (1988).
49. M. Masuda, N. Yamada, T. Soma, M. Matsui, and I. Oda, "Fatigue of Ceramics (Part 2)-Cyclic Fatigue Properties of Sintered Si_3N_4 at Room Temperature," *J. Ceram. Soc. Jpn.*, **97** [5] 520-24 (1989).
50. A.-P. Nikkila and T. A. Mäntylä, "Cyclic Fatigue of Silicon Nitrides," *Ceram. Eng. Sci. Proc.*, **10** [7-8] 646-56 (1989).
51. V. Zelizko and M. V. Swain, "Influence of Surface Preparation on the Rotating Flexural Fatigue of Mg-PSZ," *J. Mater. Sci.*, **23**, 1077-82 (1988).
52. K. Majima, K. Amafuji, H. Nagai, and K. Shoji, "Fatigue Behavior of Y-PSZ under Alternating Stresses," *J. Mater. Sci. Lett.*, **8**, 183-85 (1989).
53. E. Minford and K. M. Prewé, "Fatigue Behavior of Silicon Carbide Fiber Reinforced Lithium-Alumino-Silicate Glass-Ceramics"; pp. 561-70 in *Tailoring Multiphase and Composite Ceramics*, Edited by R. E. Tressler, G. L. Messing, C. G. Patano and R. E. Newnham, Plenum Press, New York, 1986.
54. J. W. Holmes, T. Kotil and W. T. Foulds, "High Temperature Fatigue of SiC Fiber-Reinforced Si_3N_4 Ceramic Composites"; pp. 176-86 in *Symposium on High Temperature Composites*, American Society for Composites, Technomic Publishing Co., June 1989.
55. S. Suresh and L. X. Han, "Fracture of Si_3N_4 -SiC Whisker Composites under Cyclic Loads," *J. Am. Ceram. Soc.*, **71** [3] C-158-C-161 (1988).
56. A. A. Morrone, S. R. Nutt, and S. Suresh, "Fracture Toughness and Fatigue Crack Growth Behavior of Al_2O_3 -SiC Composite," *J. Mater. Sci.*, **23**, 3206-13 (1988).
57. E. Y. Luh, R. H. Dauskart, and R. O. Ritchie, "Cyclic Fatigue-Crack Growth Behavior of Short Cracks in SiC-Reinforced Lithium Aluminosilicate Glass-Ceramic Composite," *J. Mater. Sci. Lett.*, **9**, 719-25 (1990).
58. M. Masuda, T. Soma, and M. Matsui, "Cyclic Fatigue Behavior of Si_3N_4 Ceramics," *J. European Ceram. Soc.*, **6**, 253-58 (1990).

59. T. Mayer, "Cyclic Fatigue of Alumina", M.S. Thesis, University of Illinois, Urbana, IL, May, 1990.
60. L. X. Han, L. Ewart, and S. Suresh, "Elevated Temperature Crack Propagation in Al_2O_3 and Al_2O_3 -SiC Composite under Static and Cyclic Loads," Brown University Report No. DE-FG-02-84ER-45167/1/89, Providence, RI, December 1989.
61. S. Suresh, "Fatigue Crack Growth in Ceramic Materials at Ambient and Elevated Temperatures"; pp. 759-68 in *Fatigue 90*, Vol. 2, Edited by H. Kitagawa and T. Tanaka, Materials and Component Engineering Publications Ltd, Birmingham, U.K., 1990.
62. L. X. Han and S. Suresh, "High-Temperature Failure of an Alumina-Silicon Carbide Composite under Cyclic Loads: Mechanisms of Fatigue Crack-Tip Damage," *J. Am. Ceram. Soc.*, **72** [7] 1233-38 (1989).
63. R. A. Page and J. Lankford, "The Effect of Cyclic Creep on Grain-Boundary Cavitation in Ceramics," *J. Mater. Sci.*, **22**, 2521-28 (1987).
64. T. Fett, G. Himsolt and D. Munz, "Cyclic Fatigue of Hot-Pressed Si_3N_4 at High Temperatures," *Advanced Ceramic Materials*, **1** [2] 179-84 (1986).
65. M. Masuda, T. Soma, M. Matsui, and I. Oda, "Cyclic Fatigue of Sintered Silicon Nitride"; pp. 537-42 in *Structural Ceramics/Fracture Mechanics*, Proceedings of the MRS International Meeting on Advanced Materials, Vol. 5 (Tokyo, Japan, June, 1988). Edited by Y. Hamano, O. Kamigaito, T. Kishi, and M. Sakai., Materials Research Society, Pittsburgh, PA, 1989.
66. M. Masuda, T. Soma, M. Matsui, and I. Oda, "Fatigue of Ceramics (Part 3)-Cyclic Fatigue Behavior of Sintered Si_3N_4 at High Temperature," *J. Ceram. Soc. Jpn.*, **97** [6] 612-18 (1989).
67. A. G. Evans and A. Rana, "High Temperature Failure Mechanisms in Ceramics," *Acta Metall.*, **28**, 129-41 (1980).
68. D. S. Wilkinson and V. Vitek, "The Propagation of Cracks by Cavitation: A General Theory," *Acta Metall.*, **30**, 1723-32 (1982).
69. R. L. Tsai and R. Raj, "Creep Fracture in Ceramics Containing Small Amounts of a Liquid Phase," *Acta Metall.*, **30**, 1043-58 (1982).
70. J. E. Marion, A. G. Evans, M. D. Drory, and D. R. Clarke, "High Temperature Failure Initiation in Liquid Phase Sintered Materials," *Acta. Metall.*, **31**, 1445-57 (1983).
71. M. D. Thouless, C. H. Hsueh, and A. G. Evans, "A Damage Model of Creep Crack Growth in Polycrystals," *Acta. Metall.*, **31**, 1675-87 (1983).
72. B. J. Dalgleish, S. M. Johnson, and A. G. Evans, "High-Temperature Failure of Polycrystalline Alumina: I, Crack Nucleation," *J. Am. Ceram. Soc.*, **67** [11] 741-50 (1984).
73. W. Blumenthal and A. G. Evans, "High-Temperature Failure of Polycrystalline Alumina: II, Creep Crack Growth and Blunting," *J. Am. Ceram. Soc.*, **67** [11] 751-59 (1984).

74. S. M. Johnson, B. J. Dalgleish, and A. G. Evans, "High-Temperature Failure of Polycrystalline Alumina: III, Failure Times," *J. Am. Ceram. Soc.*, **67** [11] 759-63 (1984).
75. B. J. Dalgleish, E. B. Slamovich, and A. G. Evans, "Duality in the Creep Rupture of a Polycrystalline Alumina" *J. Am. Ceram. Soc.*, **68** [11] 575-81 (1985).
76. D. R. Clarke, "High-Temperature Deformation of a Polycrystalline Alumina Containing an Intergranular Glass Phase," *J. Mater. Sci.*, **20**, 1321-32 (1985).
77. K. Jakus, S. M. Wiederhorn, and B. J. Hockey, "Nucleation and Growth of Cracks in Vitreous-Bonded Aluminum Oxide at Elevated Temperatures," *J. Am. Ceram. Soc.*, **69** [10] 725-31 (1986).
78. M. D. Thouless and A. G. Evans, "On Creep Rupture in Materials Containing an Amorphous Phase," *Acta Metall.*, **34**, 23-31 (1986).
79. R. A. Page and K. S. Chan, "Stochastic Aspects of Creep Cavitation in Ceramics," *Metall. Trans. A*, **18** [11] 1843-54 (1987).
80. G. D. Quinn, "Fracture Mechanism Maps for Advanced Structural Ceramics, Part 1: Methodology and Hot-Pressed Silicon Nitride Results," *J. Mater. Sci.*, **25**, 4361-76 (1990).
81. A. G. Robertson, D. S. Wilkinson, and C. H. Caceres, "Creep and Creep Fracture in Hot-Pressed Alumina," *J. Am. Ceram. Soc.*, **74** [5] 915-21 (1991).
82. D. S. Wilkinson, C. H. Caceres, and A. G. Robertson, "Damage and Fracture Mechanisms During High-Temperature Creep in Hot-Pressed Alumina," *J. Am. Ceram. Soc.*, **74** [5] 922-33 (1991).
83. E. K. Tschegg and S. Suresh, "Tensile Fracture Toughness Measurements in Ceramics," *J. Am. Ceram. Soc.*, **70** [3] C-41-C-43 (1987).
84. K. C. Liu and C. R. Brinkman, "Tensile Cyclic Fatigue of Structural Ceramics"; pp. 279-84 in Proceedings of the 23rd Automotive Technology Development Contractors' Coordination Meeting, P-165 (Dearborn, MI, Oct. 21-24, 1985). Society of Automotive Engineers, Inc., Warrendale, PA., 1986.
85. S. M. Wiederhorn, "Subcritical Crack Growth in Ceramics"; pp. 623-46 in *Fracture Mechanics of Ceramics*, Vol. 2, Edited by R. C. Bradt, D. P. H. Hasselman and F. F. Lange, Plenum Press, New York, 1974.
86. D. W. Richerson, *Modern Ceramic Engineering: Properties, Processing and Use in Design*, Marcel Dekker, New York, 1982.
87. R. W. Rice, "Ceramic Fracture Features, Observations, Mechanisms, and Uses", pp. 5-103 in *Fractography of Ceramic and Metal Failures*, ASTM STP 827, Edited by J. J. Mecholsky, Jr. and S. R. Powell, Jr., American Society for Testing and Materials, Philadelphia, PA, 1984.
88. R. O. Ritchie, "Mechanisms of Fatigue Crack Propagation in Metals, Ceramics and Composites: Role of Crack Tip Shielding," *Mater. Sci. Eng.*, **A103**, 15-28 (1988).

89. M. V. Swain, "Toughening Mechanisms for Monolithic Ceramics", pp. 219-76 in *Transactions of the Materials Research Society of Japan*, Edited by S. Somiya, M. Doyama, M. Hasegawa, and Y. Agata, Elsevier Science Publishers Ltd., New York, 1990.
90. D. R. Clarke, "A Simple Calculation of Process-Zone Toughening by Microcracking," *J. Am. Ceram. Soc.*, **67** [1] C15-C16 (1984).
91. A.G. Evans and K.T. Faber, "Crack-Growth Resistance of Microcracking Brittle Materials," *J. Am. Ceram. Soc.*, **67** [4] 255-260 (1984).
92. R. Knechans and R. Steinbrech, "Memory Effect of Crack Resistance During Slow Crack Growth in Notched Al_2O_3 Specimens," *J. Mater. Sci. Lett.*, **1**, 327-29 (1982).
93. P. L. Swanson, C. J. Fairbanks, B. R. Lawn, Y.-W. Mai, and B. J. Hockey, "Crack-Interface Grain Bridging as a Fracture Resistance Mechanism in Ceramics: I, Experimental Study on Alumina," *J. Am. Ceram. Soc.*, **70** [4] 279-89 (1987).
94. H. Wieninger, K. Kromp, and R. F. Pabst, "Crack Resistance Curves of Alumina at High Temperatures," *J. Mater. Sci.*, **22**, 1352-58 (1987).
95. P. L. Swanson, "Crack-Interface Traction: A Fracture-Resistance Mechanism in Brittle Polycrystals", pp. 135-55 in *Advances in Ceramics, Vol. 22: Fractography of Glasses and Ceramics*, Edited by J. R. Varner and V. D. Frechette, The American Ceramic Society, Inc., Westerville, OH, 1988.
96. R. W. Steinbrech, A. Reichl, and W. Schaarwachter, "R-Curve Behavior of Long Cracks in Alumina," *J. Am. Ceram. Soc.*, **73** [7] 2009-15 (1990).
97. Y. Fu and A. G. Evans, "Microcrack Zone Formation in Single Phase Polycrystals," *Acta. Metall.*, **30**, 1619-25 (1983).
98. A. G. Evans and Y. Fu, "Mechanical Behavior of Alumina: A Model Anisotropic Brittle Solid", pp. 697-19 in *Advances in Ceramics, Vol. 10: Structure and Properties of MgO and Al_2O_3 Ceramics*, Edited by W. D. Kingery, The American Ceramic Society, Inc., Westerville, OH, 1984.
99. B. R. Lawn, "Fundamental Condition for the Existence of Microcrack Clouds in Monophase Ceramics," *J. European Ceram. Soc.*, **7**, 17-20 (1991).
100. R. W. Rice, S. W. Freiman, and P. F. Becher, "Grain-Size Dependence of Fracture Energy in Ceramics: I, Experiment," *J. Am. Ceram. Soc.*, **64** [6] 345-50 (1990).
101. S. Lathabai, J. Rodel, and B. R. Lawn, "Cyclic Fatigue from Frictional Degradation at Bridging Grains in Alumina," *J. Am. Ceram. Soc.*, **74** [6] 1340-48 (1991).
102. S. M. Wiederhorn and E. R. Fuller, Jr., "Structural Reliability of Ceramic Materials," *Mater. Sci. Eng.*, **71**, 169-86 (1985).
103. M. D. Thouless, "Bridging and Damage Zones in Crack Growth," *J. Am. Ceram. Soc.*, **71** [6] 408-13 (1988).

104. O. V. Mazurin, M. V. Streltsina, and T. P. Shvaiko-Shvaikovskaya, *Handbook of Glass Data, Part A: Silica Glass and Binary Silicate Glasses*; pp. 75-86. Elsevier Science Publishers, Amsterdam, The Netherlands, 1983.

APPENDIX: Calculation of the Effective Stress Intensity Factor at the Crack Tip under Different Loading Conditions with the Bridging Effect of the Viscous Glassy Phase behind the Crack Tip.

In order to examine the bridging effect by the viscous glassy phase on the crack-tip stress intensity factor, a simplified model derived by Thouless[103] was employed and extended to cyclic loading conditions. This simplified model as well as the procedures for its application to cyclic cases is outlined below.

In the following, the effective stress intensity factor at the crack tip with bridging by a single viscoelastic ligament behind the crack tip of a viscoelastic matrix (Figure A1) is calculated. Both ligament and matrix are assumed to be Maxwell materials in plane stress conditions. The force acting on the ligament, P (per unit thickness), can be expressed by a function of time, t , as follows:[103]

$$\frac{P'\{t\}}{E_l} + \frac{P\{t\}}{\eta_l} = \delta\{t\} \quad (\text{A1})$$

where E_l is Young's modulus of the ligament, η_l is the viscosity (three times the conventional (shear) viscosity), and δ is twice the crack-opening displacement at a distance $d/2$ from the crack tip. At this position, the crack-opening displacement for an elastic matrix is approximately given by[103]

$$\delta\{t\} = \frac{4 K\{t\}}{E_m} \sqrt{\frac{d}{\pi}} \quad (\text{A2})$$

where E_m is Young's modulus of the matrix, and K is the effective stress intensity factor acting at the crack tip. The analogous expression for a Maxwell material may be obtained by superposition as[103]

$$\frac{\dot{K}\{t\}}{E_m} + \frac{K\{t\}}{\eta_m} = \frac{\delta\{t\}}{4} \sqrt{\frac{\pi}{d}} \quad (\text{A3})$$

where η_m is the viscosity of the matrix. K is given by

$$K\{t\} = K_\infty - \Delta K\{t\} \quad (\text{A4})$$

where K_∞ is the applied stress intensity factor (assumed to be constant), and ΔK is the reduction in the stress intensity factor due to the bridging effect and is associated with the load in the ligament by [103]

$$\Delta K\{t\} = \frac{2 P\{t\}}{\sqrt{\pi d}} \quad (\text{A5})$$

The analytical solution for K can now be determined by the combination of Eqs. (A1-5) and expressed as [103]

$$K\{t\} = \frac{K_\infty \eta_m / \eta_l}{\eta_m / \eta_l + 8 / \pi} \{ 1 + C_1 \times \exp(-C_2 t) \} \quad (\text{A6})$$

where t is the time from when the ligament begins to grow. C_1 and C_2 are constants and given by

$$C_1 = (8 / \pi) \times [E_m \eta_l / E_l \eta_m - 1] / (E_m / E_l + 8 / \pi)$$

$$C_2 = (E_m / \eta_m) \times (\eta_m / \eta_l + 8 / \pi) / (E_m / E_l + 8 / \pi)$$

In the case that the matrix is elastic and the ligament is viscous, the solution for K may be obtained by repeating the derivation and neglecting the terms associated with E_l or η_m in Eqs. (A1) and (A3), or by considering the limits of Eq. (A6). The solution for K in this case then becomes

$$K = K_{\infty} [1 - \exp(-\pi E_m t / 8 \eta_l)] \quad (\text{A7})$$

The results obtained in Eq. (A7) may be treated as the consequences of the bridging effect by a single viscous ligament behind the tip of a crack in an elastic matrix under static loading conditions. The procedures of the above derivation can be extended to the case of varying or cyclic loading with the consideration that the applied stress intensity factor, K_{∞} , is a function of time instead of a constant. Thus, for cyclic loading case, Eq. (A4) becomes

$$K\{t\} = K_{\infty}\{t\} - \Delta K\{t\} \quad (\text{A8})$$

As the viscous ligament in an elastic matrix is the proper case for the selected alumina under the given stress-temperature conditions in the present work, we only consider the relevant terms in Eqs. (A1) and (A3) in conjunction with Eqs. (A2), (A5), and (A8) to obtain the solution for the effective crack-tip stress intensity factor, K , under cyclic loading conditions. The governing equation for K in this case is then expressed as

$$\dot{K}\{t\} + \frac{K\{t\}}{t_c} = \frac{K_{\infty}\{t\}}{t_c} \quad (\text{A9})$$

where a characteristic time constant, t_c , for the rate-sensitivity of deformation of the viscous ligament can be defined as $t_c = 8\eta_l/\pi E_m$. The solution of K in the above ordinary

differential equation may be obtained analytically or numerically by applying the known function of K_{∞} into the right hand side of Eq. (A9).

The effective stress intensity factor at the crack tip under the applied various cyclic loading wave forms in the present work can now be obtained by substituting the respective cyclic wave form into Eq. (A9). A numerical analysis called Runge-Kutta method[A1] is then applied to gain the solution of K . These numerical results have been plotted in Figures 45 and 46.

References

- A1. B.Carnahan, H. A. Luther, and J. O. Wilkes, *Applied Numerical Methods*, Chap.6, John Wiley & Sons, Inc., New York, 1969.

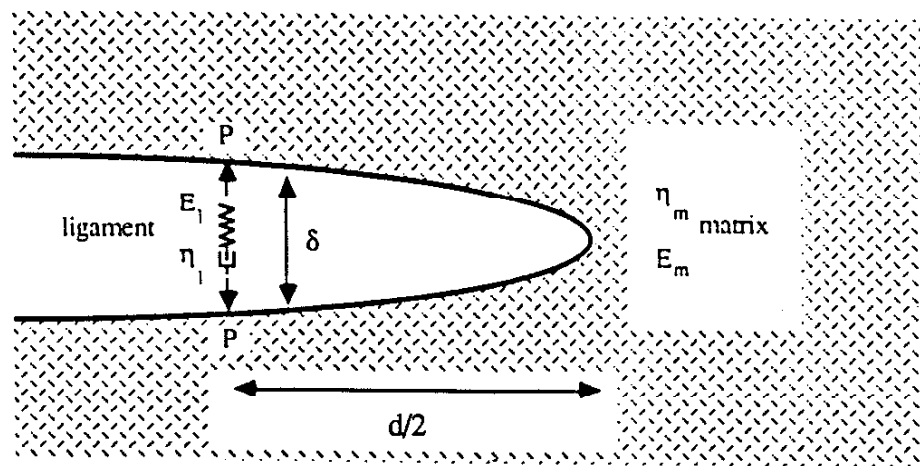


Figure A1 Geometry of the crack and ligament assumed for the bridging-zone model.
(From Ref. 103)